


3-21-2019

Wall Model Large Eddy Simulation of a Diffusing Serpentine Inlet Duct

Ryan J. Thompson

Follow this and additional works at: <https://scholar.afit.edu/etd>

 Part of the [Aerodynamics and Fluid Mechanics Commons](#), [Dynamical Systems Commons](#), and the [Fluid Dynamics Commons](#)

Recommended Citation

Thompson, Ryan J., "Wall Model Large Eddy Simulation of a Diffusing Serpentine Inlet Duct" (2019). *Theses and Dissertations*. 2233.
<https://scholar.afit.edu/etd/2233>

This Thesis is brought to you for free and open access by the Student Graduate Works at AFIT Scholar. It has been accepted for inclusion in Theses and Dissertations by an authorized administrator of AFIT Scholar. For more information, please contact richard.mansfield@afit.edu.



WALL MODEL LARGE EDDY SIMULATION
OF A DIFFUSING SERPENTINE
INLET DUCT

THESIS

Ryan J. Thompson, Capt, USAF

AFIT-ENY-MS-19-M-248

DEPARTMENT OF THE AIR FORCE
AIR UNIVERSITY

AIR FORCE INSTITUTE OF TECHNOLOGY

Wright-Patterson Air Force Base, Ohio

DISTRIBUTION STATEMENT A. APPROVED FOR PUBLIC RELEASE;
DISTRIBUTION UNLIMITED.

The views expressed in this thesis are those of the author and do not reflect the official policy or position of the United States Air Force, Department of Defense, or the United States Government.

AFIT-ENY-MS-19-M-248

WALL MODEL LARGE EDDY SIMULATION
OF A DIFFUSING SERPENTINE
INLET DUCT

THESIS

Presented to the Faculty
Department of Aeronautics and Astronautics
Graduate School of Engineering and Management
Air Force Institute of Technology
Air University
Air Education and Training Command
In Partial Fulfillment of the Requirements for the
Degree of Master of Science in Aeronautical Engineering

Ryan J. Thompson, BSAE
Capt, USAF

March, 2019

DISTRIBUTION STATEMENT A. APPROVED FOR PUBLIC RELEASE;
DISTRIBUTION UNLIMITED.

AFIT-ENY-MS-19-M-248

WALL MODEL LARGE EDDY SIMULATION
OF A DIFFUSING SERPENTINE
INLET DUCT

Ryan J. Thompson, BSAE
Capt, USAF

Approved:

Lt Col Jeffrey R. Komives, PhD
Committee Chairman

Date

Dr. Mark D. Polanka
Committee Member

Date

Lt Col Darrell S Crowe, PhD
Committee Member

Date

Abstract

The modeling focus on serpentine inlet ducts (S-duct), as with any inlet, is to quantify the total pressure recovery and flow distortion after the inlet, which directly impacts the performance of a turbine engine fed by the inlet. Accurate prediction of S-duct flow has yet to be achieved amongst the computational fluid dynamics (CFD) community to improve the reliance on modeling reducing costly testing. While direct numerical simulation of the turbulent flow in an S-duct is too cost prohibitive due to grid scaling with Reynolds number, wall-modeled large eddy simulation (WM-LES) serves as a tractable alternative. US3D, a hypersonic research CFD code developed by University of Minnesota was used with inviscid fluxes calculated using 4th order kinetic-energy consistent schemes by Subbareddy and Candler with a flux limiter by Ducro. The WM-LES model by Komives was applied with a constant Vreman sub grid scale model. The use of higher order numerical models on a fully structured grid were assessed with delayed detached eddy simulation (DDES) and WM-LES turbulence models to obtain increased prediction accuracy of the S-duct flow when compared to previous studies and test data. Further, a first of its kind dynamic Vreman model was derived, implemented, and validated in US3D using a flat plate model.

Acknowledgements

First, I sincerely thank my research advisor, whose continued support and mentorship made this research possible. Additionally, I greatly appreciate my committee members, whose guidance throughout the research was invaluable.

I would like to thank the Boeing Company for their sponsorship of this research. I would like to acknowledge the computational resources and assistance provided by the Department of Defense High Performance Computing Modernization Program that made this research a success. Also, I would like to thank the efforts of AFIT/CI for providing access and support to the UNIX Lab.

I am grateful to my wife for her continued encouragement and support. You have influenced where I am today and helped make this achievement possible.

Lastly, I owe many thanks to my family, friends, and professors, all of whom contributed to this great achievement. Especially to the Unix Lab Crew, this experience would not have been the same without you.

Ryan J. Thompson

Table of Contents

	Page
Abstract	iv
Acknowledgements	v
List of Figures	ix
List of Tables	xiv
List of Symbols	xvi
List of Abbreviations	xix
I. Introduction	1
1.1 Motivation and Background	1
1.2 Model Geometry	3
1.3 Research Objectives	4
1.3.1 Primary Objective	4
1.3.2 Secondary Objectives	5
1.3.3 Figures of Merit	6
1.4 Document Outline	7
II. Literature Review	9
2.1 Introduction	9
2.2 Viscous Flow	9
2.2.1 Boundary Layer	9
2.2.2 Turbulence	12
2.2.3 Oil Flow Visualization	13
2.2.4 Separated Flow Topology	14
2.3 Diffusing Serpentine Inlet Duct	17
2.3.1 Geometry	17
2.3.2 Fluid Flow	18
2.3.3 Flow Distortion	20
2.4 Reynolds Averaged Navier Stokes Turbulence Models	22
2.4.1 Assumptions	23
2.4.2 Formulation	23
2.4.3 Limitations	25
2.5 Large Eddy Simulation Turbulence Models	26
2.5.1 Turbulence Scale Filtering	27
2.5.2 Sub-Grid Stress Models	28

	Page
2.5.3 Large Eddy Simulation Models	32
2.6 Serpentine Inlet Testing	35
2.6.1 NASA Experiment	35
2.6.2 ONERA Experiment	41
2.7 Current Serpentine Inlet Turbulence Modeling	46
2.8 Chapter Summary	57
III. Methodology	59
3.1 Introduction	59
3.2 Computational Model	59
3.2.1 Navier-Stokes	60
3.2.2 LES	61
3.3 Grid Generation	63
3.4 Test Matrix	69
3.5 Data Collection	71
3.5.1 S-duct Surface Data	72
3.5.2 AIP Probe Data	72
3.5.3 Plane Slices	75
3.6 Post Processing Methods	76
3.6.1 Solution Convergence	77
3.6.2 Mass Flow Rate	79
3.6.3 Surface Statistics	80
3.6.4 AIP Probes	82
3.7 Grid Independence	86
3.8 Chapter Summary	87
IV. Results and Analysis	89
4.1 Introduction	89
4.2 Grid Independence Results	89
4.2.1 First Order Temporal Grid Independence	89
4.2.2 Modified Assessment of the First Order Temporal Grid Independence	97
4.2.3 Second Order Temporal Grid Independence	102
4.2.4 Grid Independence Comparison	105
4.2.5 Grid Independence Conclusion	108
4.3 Comparisons to Test Data	109
4.3.1 Mass Flow	109
4.3.2 Total Pressure Recovery	111
4.3.3 Instantaneous Center Plane Slice	118
4.3.4 Oil Flow Visualizations	121
4.3.5 Circumferential Flow Distortion	124

	Page
4.3.6 Comparison to Test Data Conclusion	126
4.4 Comparison of Pressure Recovery Mapping Methods	128
4.5 Slices from Video	130
4.6 Summary of Results	135
V. Dyanmic Vreman	137
5.1 Introduction	137
5.2 Methodology	137
5.2.1 Numerical Model	138
5.2.2 US3D Implementation	141
5.2.3 Test Model	143
5.2.4 Data Collection and Comparison	144
5.3 Results	145
5.4 Conclusion	148
VI. Conclusions and Recommendations	151
6.1 Summary and Conclusions	151
6.2 Recommendations and Future Research Areas	155
Appendix A. AIP Grid Probe Locations	158
Bibliography	161
Vita	164

List of Figures

Figure		Page
1.1	Diffusing serpentine inlet duct considered in this study	4
2.1	Boundary layer formation (Figure from Cantwell [6])	10
2.2	Non-dimensionalized incompressible turbulent boundary layer (Figure from Komives [8])	12
2.3	Eddy energy cascade (Figure from Pope [10, p.188])	13
2.4	Singular points in oil flow visualizations (Figure from Wellborn <i>et al.</i> [11])	14
2.5	Stream surface bifurcations (Figure from Wellborn <i>et al.</i> [11]) . . .	15
2.6	Stream surface bifurcations (Figure from Wellborn <i>et al.</i> [11]) . . .	16
2.7	Owl face of the first kind (Figure from Wellborn <i>et al.</i> [11])	17
2.8	Double S-duct comprised of two single S-ducts	18
2.9	Oil flow visualization along a plate inserted along centerline plane within the single turn S-duct flow moving from left to right. (Figure from Wellborn <i>et al.</i> [11])	19
2.10	Inlet flow distortion effects (Figure from Mattingly [18, p.890]) . .	21
2.11	Spectrum of homogeneous turbulence with a filter separating resolved and subgrid scales (Figure from Garnier, Adams, and Sagaut <i>et al.</i> [23])	29
2.12	Comparison of Hybrid RAN/LES (left), Wall-Resolved LES (center), and Wall-Modeled LES (right)	32
2.13	Experimental setup used by Wellborn <i>et al.</i> (Figure from Wellborn <i>et al.</i> [1])	36
2.14	Plane locatations throughout the S-duct (Figure from Wellborn <i>et al.</i> [11])	37
2.15	Close view of the oil flow visualization in the separation region on one half of the duct (Figure from Wellborn <i>et al.</i> [1])	38
2.16	Oil flow visualization on one half of the S-duct (Figure from Wellborn <i>et al.</i> [1])	38

Figure		Page
2.17	Pressure along the axial and plane surfaces of the S-duct (Figure from Wellborn <i>et al.</i> [1])	39
2.18	Pressure distribution on across the planes of the S-duct (Figure from Wellborn <i>et al.</i> [1])	39
2.19	Transverse Mach component of velocity across the planes of the S-duct (Figure from Wellborn <i>et al.</i> [1])	40
2.20	Scaled S-duct model used by ONERA and Boeing (Figure from Delot and Scharnhorst [2])	42
2.21	S-duct instrumentation (Figure from Delot and Scharnhorst [2])	43
2.22	Axial static pressure along the S-duct (Figure from Delot and Scharnhorst [2])	43
2.23	Circumferential static pressure along the S-duct (Figure from Delot and Scharnhorst [2])	44
2.24	Total pressure recovery and flow distortion at the AIP following S-duct (Figure from Delot and Scharnhorst [2])	45
2.25	Computational O-grid viscous mesh (Figure from Wellborn <i>et al.</i> [11])	46
2.26	Experimental and computational comparisson of pressure coefficient (Figure from Wellborn <i>et al.</i> [11])	47
2.27	Comparison of pressure recovery and flow distortion solutions presented for the baseline flow condition on the scaled Wellborn S-duct (Figure from Delot and Scharnhorst [2])	49
2.28	Comparison of pressure recovery at the AIP (Figure from Delot and Scharnhorst [2])	50
2.29	Comparison of surface pressure in the S-duct (Figure from Delot and Scharnhorst [2])	51
2.30	Single S-duct with a D-shaped thoat used in the 3rd Propulsion Aerodynamics Workshop (Figure modified from Winkler and Davis [3])	52
2.31	Single S-duct with a D-shaped Mach countours for different grids (Figure from Winkler and Davis [3])	52
2.32	Single S-duct with a D-shaped thoat pressure recovery for different grids (Figure from Winkler and Davis [3])	53

Figure		Page
2.33	Instantaneous Mach countour of the diffusing double S-duct with a flow rate of 2.40 kg/s (Figure from Lakebrink and Mani [4])	54
2.34	Flow separations of DDES skin-friction lines compared to the experimental oil flow (Figure from Lakebrink and Mani [4])	55
2.35	Comparison of different turbulence models and test data of the AIP (Figure from Lakebrink and Mani [4])	55
2.36	Instantaneous turbulent viscosity solutions of DDES and IDDES along the centerline and AIP (Figure from Lakebrink and Mani [4])	56
2.37	Upper flow separation differences between DDES and IDDES skin-friction solutions when compared to experimental oil flow visualization (Figure from Lakebrink and Mani [4])	57
3.1	Embedded wall-model mesh overlayed on the LES cells with a probe location in the 4th cell (Figure from Komives [8])	63
3.2	Surface and block topology of the AIP section	64
3.3	Structured grid slices throughout the geometry.	65
3.4	y^+ obtained on the surface of the S-duct.	67
3.5	Comparison of the smoothed medium density grids at the AIP . . .	68
3.6	Probe layout of the AIP probes.	73
3.7	Example of the convergence of the running average of the mass balance for the unsteady solution.	78
3.8	Example of the convergence of the running average of the pressure for the unsteady solution.	79
3.9	PSD of the half of the outer and inner rings of the AIP probes . . .	84
4.1	Comparison of total pressure recovery at AIP of three different grid densities using 4th order DDES using the full collected time history.	91
4.2	Comparison of upper flow separation region of three different grid densities using 4th order DDES.	93
4.3	Comparison of lower flow separation region of three different grid densities using 4th order DDES.	93
4.4	Comparison of coefficient of pressure along the upper and lower centerlines of three different grid densities to test data using 4th order DDES.	96

Figure		Page
4.5	Comparison of instantaneous center plane slices of the three grids using 4th order DDES with a 1st order temporal scheme.	98
4.6	Comparison of total pressure recovery at AIP of fine grid by averaging last data points from history using 4th order DDES.	100
4.7	Comparison of total pressure recovery at AIP of three different grid densities using 4th order DDES using the last 50,000 samples from the time history.	101
4.8	Comparison of total pressure recovery at AIP of three different grid densities using 4th order DDES using the last 50,000 samples from the time history for a 2nd order temporal scheme.	103
4.9	Comparison of instantaneous center plane slices of the three grids using 4th order DDES with a 2nd order temporal scheme.	106
4.10	Total pressure recovery and circumferential flow distortion trends over a range of mass flow rates (Figure from Lakebrink and Mani [4])	111
4.11	Comparison of total pressure recovery to different flow rates of test data.	112
4.12	Total pressure recovery comparison with 4th order flux scheme solutions of 1st order temporal DDES (pink), 2nd order temporal DDES (purple), and WM-LES (light blue) added (Figure adapted from Lakebrink and Mani [4])	114
4.13	Comparison of total pressure recovery at AIP of DDES using 4th order spatial fluxes in a) and b) against 2nd order spatial fluxes in c) and test data in d).	115
4.14	Comparison of total pressure recovery at AIP of DDES and WM-LES on structured grids to test data.	117
4.15	Comparison of instantaneous center plane slices of 4th order structured DDES and WM-LES solutions to 2nd order mixed grid DDES solution.	119
4.16	Comparison of upper flow separation region of the 1st order temporal DDES and WM-LES solutions compared to mixed grid DDES and test data.	122
4.17	Comparison of upper flow separation region of the time averaged WM-LES to the instantaneous WM-LES.	123

Figure		Page
4.18	Comparison of lower flow separation region of the 1st order temporal DDES and WM-LES solutions compared to mixed grid DDES and test data.	124
4.19	Comparison of lower flow separation region of the time averaged WM-LES to the instantaneous WM-LES.	125
4.20	Circumferential flow distortion comparison with 4th order flux scheme solutions of 1st order temporal DDES (pink), 2nd order temporal DDES (purple), and WM-LES (light blue) added (Figure adapted from Lakebrink and Mani [4])	126
4.21	Comparison of 40 probe AIP solution to the 72,000 point plane averaged solution from the full 320,000 sample time history of the fine grid.	129
4.22	DDES video frames of the total pressure recovery at the AIP taken 0.1 milliseconds apart.	132
4.23	WM-LES video frames of the total pressure recovery at the AIP taken 0.1 milliseconds apart.	134
5.1	Test filter averaging for interior faces, boundary faces, and shared faces	142
5.2	Instantaneous calculated c_d of a slice through the domain	145
5.3	Instantaneous density gradient magnitude of a slice through the developing flow	146
5.4	Time averaged wall shear on the surface of the flat plate	146
5.5	Time averaged wall shear and its mean at $x = 14\delta$ on the surface of the flat plate	148

List of Tables

Table		Page
2.1	Grid scaling requirements turbulent boundary layers with high Reynolds numbers (Table from Choi and Moin [27])	33
2.2	Distortion coefficients of the ONERA test cases.	45
2.3	Summary of solutions presented for the baseline flow condition on the scaled Wellborn S-duct (Figure from Delot and Scharnhorst [2])	48
3.1	Planned Test Matrix of Structured Approach	69
3.2	Planned Test Matrix of Wall Model Probe Sensitivity Study	70
3.3	Completed Test Matrix of Structured Approach	71
3.4	Deviations of probe location achieved from AIP probe locations in millimeters.	73
3.5	Probe locations of the AIP probes and the cell centers of the cells which the probe locations occur for the medium grid.	74
3.6	Grid densities of clustered grids used for independence study.	86
4.1	Outflow mass flow for the three grids using a 1st order temporal scheme.	90
4.2	Grid independence of total pressure recovery and circumferential flow distortion from full time history.	92
4.3	Total pressure recovery and circumferential flow distortion of the fine grid based on different sample sizes.	100
4.4	Grid independence of total pressure recovery and circumferential flow distortion from last 50,000 iterations for the 1st order temporal scheme.	101
4.5	Outflow mass flow for the three grids using a 2nd order temporal scheme.	102
4.6	Grid independence of total pressure recovery and circumferential flow distortion from last 50,000 iterations for the 2nd order temporal scheme.	104
4.7	Outflow mass flow for the three cases all using a 4th order flux scheme.	110

Table		Page
4.8	Total pressure recovery for the three cases all using a 4th order flux scheme.	113
4.9	Circumferential flow distortion for the three cases all using a 4th order flux scheme.	125
A.1	Probe locations of the AIP probes and the cell centers of the cells which the probe locations occur for the clustered coarse grid for DDES.	158
A.2	Probe locations of the AIP probes and the cell centers of the cells which the probe locations occur for the clustered fine grid for DDES.	159
A.3	Probe locations of the AIP probes and the cell centers of the cells which the probe locations occur for the unclustered medium grid for WM-LES.	160

List of Symbols

Symbol		Page
M	Mach Number	1
Re	Reynolds Number	1
δ	Boundary Layer Thickness	10
τ_w	Shear Stress at the Wall	10
ρ	Density	11
U_∞	Freestream Velocity	11
C_f	Coefficient of Friction	11
Re_x	Reynolds Number Based on Distance	11
u_τ	Friction Velocity	11
u^+	Velocity in Wall Units	11
y^+	Distance from the Wall in Wall Units	11
κ	von Karman Constant	12
B	Log-Law Constant	12
ℓ_0	Integral Length Scale	12
\mathcal{L}	Flow Length Scale	12
ℓ	Eddy Length Scale	13
ℓ_{EI}	Length Scale of Lower Bounds of Energy Containing Range	13
η	Kolmogorov Length Scale	13
ℓ_{DI}	Length Scale of Upper Bounds of Dissipation Range	13
$p_{t \max}$	Maximum Total Pressure	21
$p_{t \min}$	Minimum Total Pressure	21
$p_{t \text{ avg}}$	Average Total Pressure	21
τ_{ij}	Reynolds Stress Tensor	23
μ_T	Eddy Viscosity	23
\bar{S}_{ij}	Reynolds Averaged Strain Rate Tensor	23
k	Turbulent Kinetic Energy	23

Symbol		Page
δ_{ij}	Kronecker Delta	23
ϵ	Turbulent Dissipation Rate	25
ω	Specific Rate of Dissipation	25
τ_{ij}	Subgrid Stress Tensor	28
S_{ij}	Filtered Strain Rate Tensor	28
ν_T	Subgrid Viscosity	28
C_S	Smagorinsky Constant	30
Δ	Filter Width	30
$ \bar{S} $	Magnitude of the Strain Rate Tensor	30
u_i	Velocity Components	30
k_o	Kolomogorov Constant	30
C_d	Dynamic Constant	31
α_{ij}	Vreman Model Component	31
β_{ij}	Vreman Model Component	31
B_β	Vreman Model Component	31
c	Vreman Constant	32
N	Number of Grid Points	33
U	Vector of Conserved Variables	60
F_j	Flux Vectors	60
p	Static Pressure	60
E	Energy per Unit Mass	60
σ_{ij}	Viscous Stress Tensor	60
q_j	Heat Flux Vector	60
T	Temperature	61
λ	Bulk Viscosity	61
$\hat{\mu}$	Effective viscosity	61
$\hat{\kappa}$	Thermal Conductivity	61
R	Gas Constant	61

Symbol		Page
Q	Solution Vector with Density Decoupled	62
G_j	Reduced Set of Equations Flux Vector	62
e	Specific Energy	63
C_p	Coefficient of Pressure	80
p_0	Freestream Static Pressure	80
ρ_0	Freestream Density	80
U_0	Freestream Velocity Magnitude	80
T_{ij}	Germano Relationship	138
$\hat{\Delta}$	Test Filter	138
J_{ij}	Subgrid Model Kernal	139
K_{ij}	Subgrid Model Kernal	139
E_{ij}	Numerical Method Error	140
θ	Momentum Boundary Layer Thickness	147

List of Abbreviations

Abbreviation		Page
RANS	Reynolds-Averaged Navier-Stokes	1
DDES	Delayed Detached Eddy Simulation	1
CFD	Computational Fluid Dynamics	1
DNS	Direct Numerical Simulation	1
HPC	High Performance Computer	1
LES	Large Eddy Simulation	2
SGS	Sub-Grid Stress	2
WR-LES	Wall-Resolved Large Eddy Simulation	2
WM-LES	Wall-Modeled Large Eddy Simulation	2
AIP	Aerodynamic Interface Plane	3
IDDES	Improved Delayed Detached Eddy Simulation	5
ILES	Implicit Large Eddy Simulation	27
NASA	National Aeronautics and Space Administration	35
AIP	Aerodynamic Interface Plane	42
PNS	Parabolized Navier-Stokes	46
P-PNS	Partially-Parabolized Navier-Stokes	46
ADI	Alternating-Directional Implicit	46
PSD	Power Spectrum Density	83

WALL MODEL LARGE EDDY SIMULATION
OF A DIFFUSING SERPENTINE
INLET DUCT

I. Introduction

1.1 Motivation and Background

While diffusing serpentine inlets, or S-ducts, is not a new concept dating back to the introduction of the Boeing 727 in the 1960s, the largest developments in attempting to understand the complex flow features through testing and modeling began in the early 1990s [1]. For S-ducts the parameters of total pressure recovery and flow distortion following the inlet are the most important in the characterization of the flow entering the engine following the duct. These parameters are of primary interest because they directly impact the performance of the engine the inlet feeds, and ultimately could cause damage and subsequent failure of the engine with an elevated level of flow distortion.

There is the desire in industry to reduce the dependence on testing and have increased reliance on modeling as a means to reduce cost and increase development speed. Current modeling efforts presented in Section 2.7 show that Reynolds-Averaged Navier-Stokes (RANS) turbulence models have been predominately used, but Delayed Detached Eddy Simulations (DDES) have also been applied [2]. Through both unstructured and structured grids using different turbulence models on different Computational Fluid Dynamics (CFD) codes, none have provided a solution that matches the required parameters.

A Direct Numerical Simulation (DNS) could be applied to this problem, but at a velocity of approximately Mach number, M , of 0.6, the Reynolds number, Re , for the flow of 1×10^6 with the required grid size is too computationally expensive to perform on modern day high performance computers (HPC) from both a memory and time

standpoint. Therefore, a Large Eddy Simulation (LES) method could be applied in order to obtain accurate statistical turbulent solutions without the Reynolds number limitation of DNS.

LES relies upon the assumption that the small scales of turbulence are isotropic in homogeneous turbulence, as further discussed in Chapter II. This assumption allows for the separation between resolving the larger scales that contain the majority of the energy and modeling the isotropic scales. By having the cell size nearly the same throughout the entire grid and cubic, the number of cells is optimized and the grid acts as a filter between eddies resolved larger than the minimum cell dimension and modeling scales below that dimension. The Sub-Grid Scales (SGS) are typically modeled with a Smagorinsky model, but as it has been proven to be overly dissipative, a Vreman model could be used.

LES can be subdivided into Wall-Resolved Large Eddy Simulation (WR-LES), Hybrid RANS/LES, and Wall-Modeled Large Eddy Simulation (WM-LES), as discussed in Section 2.5. WR-LES is limited much like DNS, increasingly smaller cells are needed as you approach the walls in order to appropriately resolve the eddies. Hybrid RANS/LES is susceptible to the same flaws that RANS has by relying on RANS near the wall, thus requiring smaller cells at the wall, but it resolves the eddies through LES away from the walls. WM-LES does not have either of the preceding limitations, with the biggest limitations being the wall model itself and the size of the cells. While the size of the cells needs to be constrained to the size of the integral scale length of the turbulence, it does not need grid clustering near walls in order to resolve the boundary layer. This decreases the overall number of cells needed, subsequently easing the limitation on the Reynolds number that constrains DNS.

The serpentine inlet geometry used in recent studies over the last ten years has increased in complexity, further complicating the accurate prediction of the flow. Early geometries consisted of a single turn S-duct with a circular cross-section. Within the last three years, the single turn S-duct with a D-shaped throat cross-section tran-

sitioning to a circular cross-section was studied [3]. The most recent study conducted in 2018 utilized a double turn S-duct with a D-shaped throat that transitions to a circular cross-section [4].

The modeling conducted in these recent studies on diffusing S-ducts has provided a wide range of solutions, but lacks strong conclusions [2]. Chapter II highlights the various combinations of grids, CFD codes, and RANS models utilized to produce greatly differing results. The majority of the approaches used RANS based models, with some hybrid RANS/LES models starting to gain popularity. While some combinations are capable of accurately capturing aspects of the solution, none have been able to adequately predict all the figures of merit. One of the desired outcomes of this thesis is to apply a structured approach in a study in order to make stronger conclusions as proposed by Delot and Scharnhorst [2].

1.2 Model Geometry

The current study builds upon the latest study by using the same double turn diffusing S-duct geometry. The geometry was provided by Boeing as the sponsor for this study and is presented in Figure 1.1. The labels in Figure 1.1 identify the key portions of the geometry. The bell adapter connects the bell mouth to the D-shaped throat. The double S-duct transitions from the D-shaped cross-section at the throat to a circular cross-section of the Aerodynamic Interface Plane (AIP) with the modeled rakes. The modeling of the rakes is necessary to account for the blockage in the flow caused by the instrumentation and supporting infrastructure of the AIP. This blockage ensures the simulation reaches accurate mass flow rates. While a single S-duct typically produces one separation point (primary), there is the possibility of a second separation point (secondary) to occur on the upper surface following the second turn as indicated in Figure 1.1.

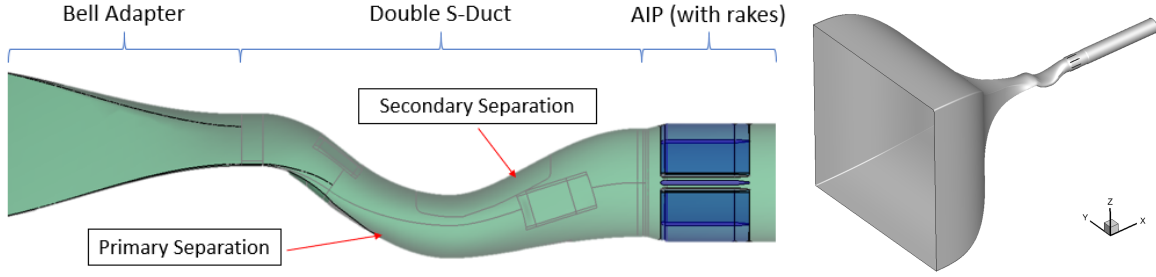


Figure 1.1: Diffusing serpentine inlet duct considered in this study

1.3 Research Objectives

The primary objective is to identify a better turbulence modeling approach for a diverging double turn serpentine inlet duct with flow separation by accurately predicting the flow separations and subsequent total pressure recovery and flow distortion at the AIP. This primary objective can be split up into several sub tasks that build upon each other. In addition, several secondary objectives exist for this thesis. These objectives compliment the primary objective by further defining guidelines for WM-LES implementation and advancing SGS modeling.

1.3.1 Primary Objective. The primary objective of increasing the accuracy of flow predictions through a diffusing S-duct is split into four tasks defined as:

Task 1: Create a fully structured grid for the provided geometry. While unstructured grids, unstructured grids with structured wall wraps, and overset grids have been applied in the past, a fully structured grid for this geometry with the included AIP rakes has not been completed. Completion of this task allows for higher order flux schemes in Task 2 to be used.

Task 2: Run the fully structured grid at higher than 2nd order flux schemes. The use of 2nd order flux schemes have been predominately used on S-ducts throughout the previous studies, primarily due to limitations of unstructured grids. To the knowledge of the author, the use of higher order methods applied to a serpentine inlet duct has not previously been attempted. Although the goal was to use a 6th order scheme, a 4th order scheme would still provide less truncation error than previous studies.

Task 3: Complete simulations using DDES and Improved Delayed Detached Eddy Simulation (IDDES) turbulence models. A few attempts of DDES and IDDES have been applied to the S-duct problem, the vast majority of prior studies have implemented various forms of RANS methods. Building off of the second objective, DDES and IDDES have not been run with a spatial flux scheme above a 2nd order method.

Task 4: Apply a WM-LES turbulence model to the S-duct. A WM-LES has been suggested for this problem, but until now it has not been attempted.

These tasks combined can be used to improve upon the understanding of DDES, IDDES, and WM-LES, methods applied to the S-duct and obtain definitive conclusions between the different approaches a structured approach is implemented. Differences between a structured and unstructured grid will be assessed using DDES with a 2nd order flux scheme. Higher order flux schemes, such as a 4th or 6th order scheme, are then compared to the 2nd order scheme, both using DDES. Lastly, IDDES and WM-LES are run at higher order flux schemes to provide comparisons between the three different models at a higher order. Ultimately, the conclusions made through the structured approach lead to the recommendations of how to more accurately predict the flow within a diffusing S-duct.

1.3.2 Secondary Objectives. In addition to comparing the primary objective, several secondary objectives exist for this thesis. These objectives compliment the primary objective by further defining guidelines for WM-LES implementation and advancing SGS modeling.

Secondary Objective 1: Characterize the sensitivity of the y^+ value for the first cell off of the wall when using WM-LES. Recommended values for the height of the first cell vary greatly, and there are no definitive requirements for the first cell height. By characterizing the impact on the solution for several cell heights, a better understanding would be formulated.

Secondary Objective 2: Conduct a sensitivity study of wall model probe location for WM-LES. Much like the cell height requirement for WM-LES being unknown, the number of cells off the wall where the wall model probe is placed is also ill defined. Although, it is generally agreed upon that the first cell is not acceptable and the third cell is a soft recommendation, a study is needed to remove potential solution dependence from the probe location.

Secondary Objective 3: Derive and implement a dynamic Vreman SGS model. While Vreman's model produces results similar to a dynamic Smagorinsky model without the increased computational cost, he notes that it could be further expanded by applying the dynamic procedure to it [5]. Following an extensive literature review, it has been concluded that the derivation and implementation of a dynamic Vreman SGS model has not been completed in an article to date, leading to the inclusion of this objective.

1.3.3 Figures of Merit. In order to assess the results and determine the accuracy of the solutions gathered in this study, figures of merit are defined for comparison. Test data provided by the sponsor is the baseline for all accuracy comparisons. The primary figures of merit come from the data collected at 40 probe locations on the AIP. The locations in the simulation align with the test set up. The total time histories of the probes are assessed for total pressure recovery and flow distortion. Additionally, the time histories can be assessed for frequency content attributed to the eddies and acoustic waves in the solution. Surface statistics temporally averaged on the S-duct are used to assess the coefficient of pressure and friction along the upper and lower centerlines, in order to identify regions of flow separation. Further, the shear stress components on the surface are used to generate oil flow visualizations to further aid in characterization of the flow above the surface and regions of flow separation. The simulated oil flow visualizations are compared to test data to provide qualitative arguments regarding the accuracy of the model.

1.4 *Document Outline*

Chapter II presents a review of literature relevant to the S-duct problem through several sections. The background information on viscous flows, turbulence, and flow separation are provided in Section 2.2. Additionally, flow visualizations and their interpretations are included. Knowledge of the foundational flow physics is necessary to understand the methods and results obtained in the completion of the objectives. Section 2.3 delves into S-ducts, the geometry, specific S-duct flow features, and the definition of flow distortion created by the duct. Following the specifics of the problem, methods applied in turbulence modeling are presented throughout Sections 2.4 and 2.5 on RANS and LES respectively. The history of recent serpentine inlet testing is discussed in Section 2.6. The data from these tests were used in large modeling studies aimed to improve the accuracy of S-duct flow prediction. Section 2.7 contains these modeling studies and even includes studies published within the last year. The objectives in Section 1.3 directly build off the results of the most recent modeling studies and advance the prediction capabilities of the modeling community.

Following the background necessary to the current problem, Chapter III presents the methodology applied in this study to obtain the objectives. Section 3.3 discusses the steps to creating a fully structured grid in support of the Primary Objective 1. The computational model used is included in Section 3.2. To complete the primary objectives and make definitive conclusions, the proposed test matrix and the completed test matrix are discussed in Section 3.4. The data collection method in Section 3.5 and the post processing of that data in Section 3.6 obtain meaningful visualizations and capture the figures of merit from Section 1.3.3 for analysis of the accuracy of simulations. Following grid independence as discussed in Section 3.7, the remaining tests from the test matrix were conducted.

The results from this study are collected in Chapter IV. The completion of the grid independence studies using two different temporal accuracy schemes with 4th order spatial DDES are presented first in Section 4.2. With a selected grid density

and temporal scheme to use, solutions were obtained using both DDES and WM-LES on structured grids for comparison to test data and previous DDES solutions with a multiblock grid in Section 4.3. The comparisons were made with mass flow rates, total pressure recovery, oil flow visualizations and flow distortion using methods from Chapter III. Section 4.4 provided an analysis on the effects of using 40 AIP probes to define the flow as opposed to using a full time averaged slice at the AIP. While a full slice is not obtainable with testing, it does provide insight as to how many probe locations should be used. Finally, Section 4.5 details the instantaneous AIP total pressure recovery patterns that exist and how they differ from the time averaged solution.

Chapter V contains the incorporation a dynamic Verman model into the flow solver. This was conducted to achieve Secondary Objective 3. The desire for the dynamic Vreman model and background information are contained in Sections 2.5 and 5.1. The full derivation of the model and incorporation into a flow solver is detailed in Section 5.2. Further, this section contains the flat plate model used to exercise the dyanmic Verman model. The results of the dyanmic Vreman model can be found within Section 5.3. The overall success of the effort is highlighted in Section 5.4.

Lastly, Chapter VI summarizes the completion of objectives and work completed in this study. Recommendations and future areas of study are also identified based upon lessons learned.

II. Literature Review

2.1 Introduction

This chapter will provide an overview of separated flows, diffusing serpentine inlet ducts, turbulence modeling, and the testing and computational methods currently employed to assess serpentine inlet ducts. The driving fluid flow physics for the serpentine inlet will be presented in Section 2.3 to provide a foundation to understand the methods and analysis conducted to assess the use of higher ordered flux schemes with DDES and WM-LES turbulence models. Details of LES will be discussed in Section 2.5 in addition to RANS turbulence models in Section 2.4. Previous experimental efforts are included as baseline information for model validation throughout Section 2.6. Finally, the chapter will conclude with Section 2.7 outlining current modeling approaches and results for serpentine inlets.

2.2 Viscous Flow

The flow propagating through an S-duct is dominated by viscous flow phenomena, and an understanding of viscous flow is required in order to appropriately model the flow. The boundary layer develops as a result of viscous forces. In order to visualize the effects of viscous flow on a surface subjected to fluid flow, oil flow visualizations are commonly applied. While oil flow visualizations provide a two-dimensional result, an understanding of surface patterns leads to inferring the three-dimensional topology. Most importantly, this can be applied to regions of separated flow to understand its development and progression downstream.

2.2.1 Boundary Layer. The viscous boundary layer evolves from the no-slip boundary condition. For a no-slip boundary condition, the flow velocity on the surface is exactly zero. In order for the velocity to transition from zero velocity on the surface to the freestream velocity away from the wall, large velocity gradients exist normal to the wall. The velocity profile can be plotted showing the gradients and the transition over a flat plate as in Figure 2.1. This figure contains both laminar and turbulent

boundary layers. The laminar boundary layer can be identified by fluid particles flowing along highly ordered streamlines. In Figure 2.1 the laminar boundary layer develops starting at the beginning of the flat plate and continues growing in thickness as it develops. The thickness of the boundary layer, δ , is defined as the point when the boundary layer velocity reaches 99% of the freestream velocity, also referred to as δ_{99} . Conversely, the turbulent boundary layer is largely chaotic with irregular, three dimensional, unsteady rotational structures with multiple length scales. In turbulent flow, the boundary layer is thicker with a larger δ_{99} than laminar flow that continues to grow, but it contains greater velocity gradients at the wall. The region between the laminar flow and turbulent flow is the transition region. The transition includes instabilities developing and growing resulting from increasing Reynolds number or irregularities on the surface. As the Reynolds number is the ratio of inertial forces to viscous forces, higher Reynolds numbers have inertial dominated flow that lacks the order preserving nature of viscous dominated flows.

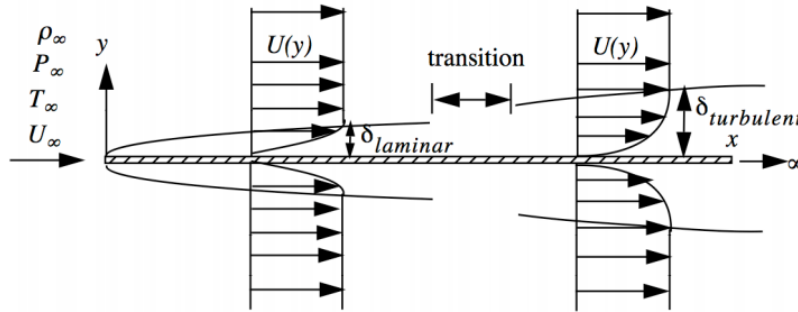


Figure 2.1: Boundary layer formation (Figure from Cantwell [6])

As a result of the velocity gradient near the wall, shear forces are exerted in the fluid and a coefficient of friction can be computed at the wall. The shear stress at the wall, τ_w is calculated as:

$$\tau_w = \frac{C_f \rho U_\infty^2}{2} \quad (2.1)$$

with ρ as density and U_∞ as the freestream velocity [7]. The coefficient of friction, C_f , for a turbulent boundary layer also presented by White for a flat plate as:

$$C_f = \frac{0.026}{Re_x^{1/7}} \quad (2.2)$$

where the coefficient is dependent on the Reynolds number based on distance, Re_x [7]. This is a nondimensional representative of the physical quantity of the shear stress at the wall. The shear stress at the wall can also be used to calculate the friction velocity, u_τ , as:

$$u_\tau = \sqrt{\frac{\tau_w}{\rho}} \quad (2.3)$$

in order to nondimensionalize the velocity in the boundary layer, u^+ , and the distance from the wall, y^+ , using scales related to the wall shear as:

$$u^+ = \frac{u}{u_\tau} \quad (2.4)$$

$$y^+ = \frac{yu_\tau}{\nu} \quad (2.5)$$

which are commonly referred to as “wall units” [8].

Non-dimensionalizing a zero pressure gradient incompressible turbulent boundary layer by wall units across Reynolds numbers results in the profile presented in Figure 2.2 known as the law of the wall [9]. The profile in Figure 2.2 can be separated into three regions the viscous sublayer, log-law layer, and the velocity-defect layer. The first region, the viscous sublayer, extends up to $y^+ \approx 10$ where the viscous effects dominate the flow and $y^+ = u^+$ [10, p.273]. The log-law region is the second region in Figure 2.2, that aligns with the dashed line and extends over $30 \leq y^+ \leq 1000$ [10, p.275]. The log-law region adheres to a logarithmic law of the wall determined by von Karman to be:

$$u^+ = \frac{1}{\kappa} \ln y^+ + B \quad (2.6)$$

where κ is the von Karman constant and B is a constant [10, p.274]. While the constants can vary, they are typically within 5% of $\kappa = 0.41$ and $B = 5.2$ [10, p.274]. The last region is the velocity-defect region and extends from the outer region of the log-law region to the outer edge of the boundary layer, where the flow is dominated by inertial effects of large eddies in the outside edge of the boundary layer [8].

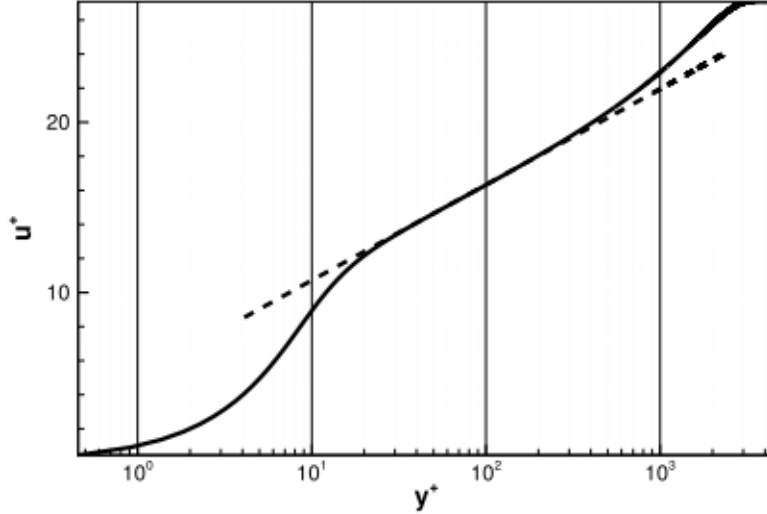


Figure 2.2: Non-dimensionalized incompressible turbulent boundary layer (Figure from Komives [8])

2.2.2 Turbulence. Understanding the different regions and how energy is transferred within turbulence provides the basis for methods used within turbulence modeling, especially within LES that resolves more of the energy than RANS. Turbulence is generally described as unsteady rotational motion with multiple length scales. It commonly forms as a result of unsteadiness occurring on the boundary of a surface, and is sustained by mean shear. Turbulent eddies break down from the largest eddies into smaller eddies until fluid viscosity dissipates the energy into heat following Richardson’s Energy Cascade [10, p.183]. The largest eddies are defined with the integral length scale, ℓ_0 , which is on the order of the flow length scale, \mathcal{L} , and thus the Reynolds numbers for both the flow length scale and the integral length scale are on the same order [10, p.183].

The transition of energy is shown in Figure 2.3 from right to left beginning with production, passing through the inertial subrange, then finally terminating with dissipation. Kolmogorov devised several hypotheses to support the energy cascade. First, the hypothesis of local isotropy in which the small scale turbulent motion ($\ell \ll \ell_0$) are statistically isotropic [10, p.184]. To further define whether eddies are considered isotropic, a separation length scale is defined as $\ell_{EI} \approx \frac{1}{6}\ell_0$. The region above ℓ_{EI} is considered the energy containing range and below ℓ_{EI} the eddies are considered locally isotropic [10, p.184]. The smallest turbulence scale, η , is defined as the Kolmogorov length scale which occurs when the Reynolds number based on the Kolomogorov length scale is exactly one [10, p.185]. Defining a length scale $\ell_{DI} = 60\eta$ specifies a separation between viscosity dominated flow and inertial dominated flow [10, p.186]. This separation, ℓ_{DI} , outlines the maximum size of the dissipation range energy in the small eddies to heat in the viscosity dominated region [10, p.186-187]. Conversely, ℓ_{DI} is the minimum of a region called the inertial subrange that is capped by ℓ_{EI} where the viscous effects are negligible [10, p.186-187].

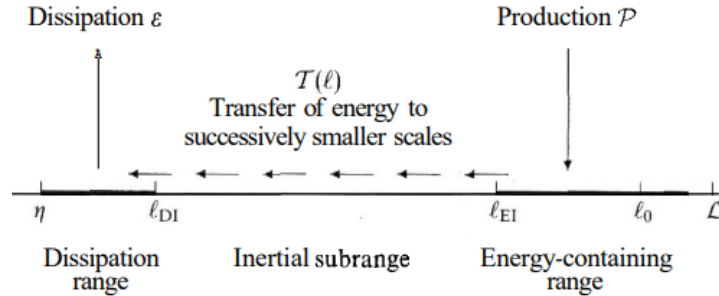


Figure 2.3: Eddy energy cascade (Figure from Pope [10, p.188])

2.2.3 Oil Flow Visualization. The use of oil flow visualization techniques are commonly applied to assess the fluid flow on the surface of an object [11]. The technique includes applying oil as a thin film, usually less than 1.27 millimeters, or as a dot matrix across the desired surface, then running the experiment allowing the patterns in the oil to develop [12]. The method can be applied to a wide range of flows from low speed water and wind tunnels to supersonic wind tunnels, with the

main consideration being the ratio of the viscosity of the fluid in the boundary layer to that of the oil, which for wind tunnels lies between 10^{-2} to 10^{-4} [12].

The main assumptions of oil flow visualization technique is that the oil streaklines follow the streamlines of the flow near the surface and that the oil has negligible impact on the boundary layer flow [12]. Squire derived oil flow equations from the viscous equations of slow motion by assuming that the oil and the air share the same velocity and viscous stresses [12]. The primary parameter in resolving flow visualizations with oil and the equations is the ratio of the viscosity of the fluid in the boundary layer to that of the oil [12]. Further testing by Squire showed the oil curves are not affected by the oil thickness, airflow speed, or velocity distributions [12]. Separated regions in oil flow visualizations form an accumulation of oil upstream of the true separation point, this indication of separation can underestimate the separation distance by as much as 5% in compressible flows, but it can be less pronounced for turbulent flows than for laminar flows [12].

2.2.4 Separated Flow Topology. While the previous section discussed the methodology of oil flow visualizations, the interpretation of the surface patterns surrounding a separated regions and its translation into three-dimensions requires knowledge of the topology of the flows and the definition of standard terms. Oil flow visualizations resolve the skin friction lines of an experiment, and when the skin friction is exactly zero, singular points occur. Singular points can be classified into nodal points, spirial nodes (foci), or saddle points as presented in Figure 2.4 [13].

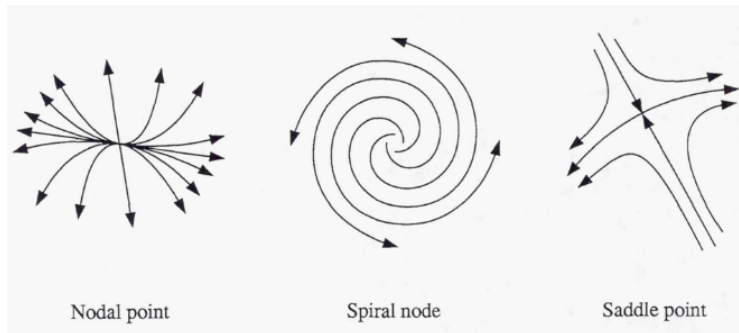


Figure 2.4: Singular points in oil flow visualizations (Figure from Wellborn *et al.* [11])

Nodal points are a singular point common to an infinite number of skin friction lines, and can be further classified into a nodal point of attachment or separation depending if the flow is away from the point or towards the point, respectively [13]. The nodal point displayed in Figure 2.4 is a nodal point of attachment. Spiral node is a point that has no common tangent line where the lines spiral around a point, and like the nodal point, can be points of attachment, as seen in Figure 2.4, or separation [11]. Lastly, the saddle point has only two lines that pass through it, one that is pointing into the point and one out of the point, the line created by these two act as a divider for all other skin friction lines that closely miss the singular point [13]. Saddle points typically occur to separate nodal points of attachment [13].

Transitioning to three-dimensional flows, the stream surface is created by the projection of the lines passing through a saddle point and terminating at nodal points [13]. Steady state three-dimensional flows have geometries that appear to bifurcate along a stream surface, with the surface acting as a dividing surface just as the saddle point acts as a dividing line [13]. Positive bifurcations occur along a stagnation line, where negative bifurcations usually come from uplifting counter-rotating vortices as shown in Figure 2.5 [14].

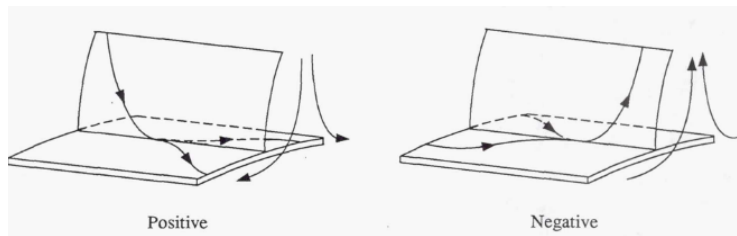


Figure 2.5: Stream surface bifurcations (Figure from Wellborn *et al.* [11])

A common way of presenting oil flow visualizations consists of mapping it on a “skeleton” drawing by cutting the S-duct along the upper surface centerline and unwrapping the oil flow visualization onto a flat horizontal surface with the bottom centerline in the middle of the figure [11]. The left hand side of Figure 2.6 shows the unwrapped lower region of a serpentine region that contains two saddle points and two spiral nodes along with both positive and negative bifurcation stream lines [11].

The pattern presented is common for separation regions and has been named “owl face” separation [15]. The right hand side of Figure 2.6 presents a more possible representation of the flow at a given snapshot because it is considered an impossible solution to have a single streakline passing through two saddles without a node in between as it is unstable [15]. This more possible separation was justified by saying the unsteadiness causes oscillations between the spiral nodes and the saddles [15].

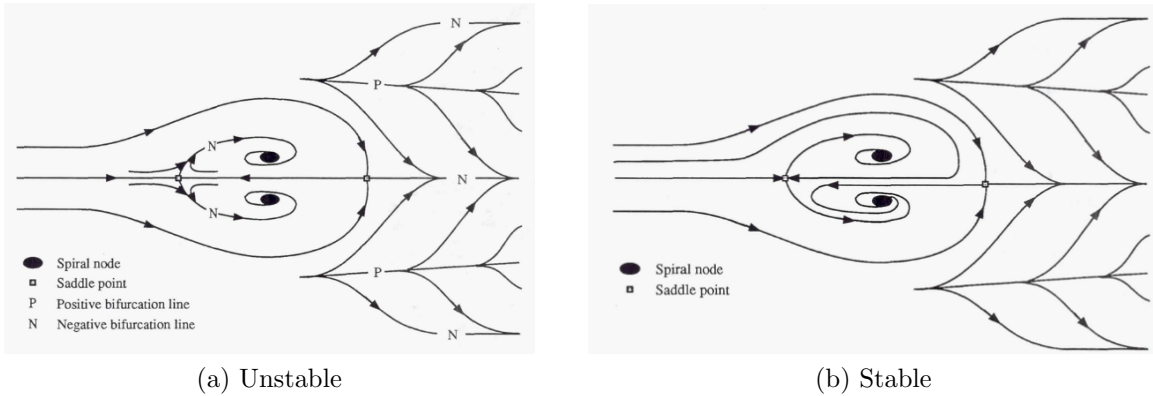


Figure 2.6: Stream surface bifurcations (Figure from Wellborn *et al.* [11])

Because of the lack of visible spiral node along the centerline, it is considered an “owl face of the first kind” which is displayed in three dimensions in Figure 2.7. The stream surfaces coil around the flow creating two tubes representing the two vortical structures that can be observed in the flow [13]. As the dividing surface rolls up around the vortical cores as it develops downstream, the well-defined core that results is called a vortex [13].

The diffusing serpentine pressure driven inlet is a viscosity dominated problem. The impact of viscosity on the development of the boundary later and effects in turbulence have been discussed in order to understand the physics that is being modeled. While oil flow visualizations of a wind tunnel will not be conducted in this study, the modeled solutions will produce surface streamlines that will be used to compare to oil flow visualizations previously completed, assisting with the determination of the location of separated flow.

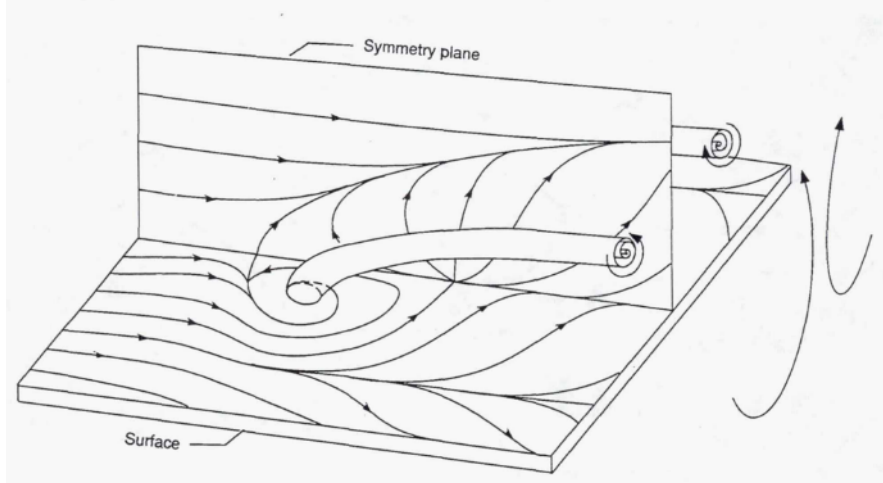


Figure 2.7: Owl face of the first kind (Figure from Wellborn *et al.* [11])

2.3 Diffusing Serpentine Inlet Duct

The first application of a diffusing serpentine inlet duct was in the rear center tail engine of the Boeing 727, and the first studied S-ducts were conducted during the design [1]. Since then, this type of inlet has been used on General Dynamics F-16 and the McDonnell-Douglas F-18 [1]. Diffusing serpentine inlet ducts, like Figure 1.1, are dominated by compressible subsonic flow driven by the geometry of the inlet. S-duct geometry often results in flow separation and subsequent reattachment on the lower surface of the duct which will be further discussed in Section 2.3.2. Flow distortion detrimental to the turbine engine results from the separation bubbles within the duct and is discussed further in Section 2.3.3.

2.3.1 Geometry. At the core, diffusing serpentine inlet ducts, commonly referred to as S-ducts, contain an offset to the flow direction between the inflow and outflow. Serpentine inlet can contain a single turn (drop down) or double turn (drop down - rise up) S-duct as shown in Figure 2.8. Each turn can be broken down into two bends. In the case of the single turn S-duct, the first bend begins the transition downward and the second bend returns the flow direction to be parallel to the flow at the throat before the first bend. For a double S-duct the two bends within the first turn are identical to a single turn S-duct, and are reversed within the second

turn. Similarly, since the flow physics of the single are essentially experienced again within the second, so this section focuses on the flow within a single turn diffusing serpentine inlet duct. The diffusing inlet gradually and continuously increases in diameter throughout the serpentine inlet creating the diffusion required to decrease the flow velocity, preparing it for what would be a turbine engine compressor fan, while trying to minimize the flow distortion and total pressure loss [16, p.460].

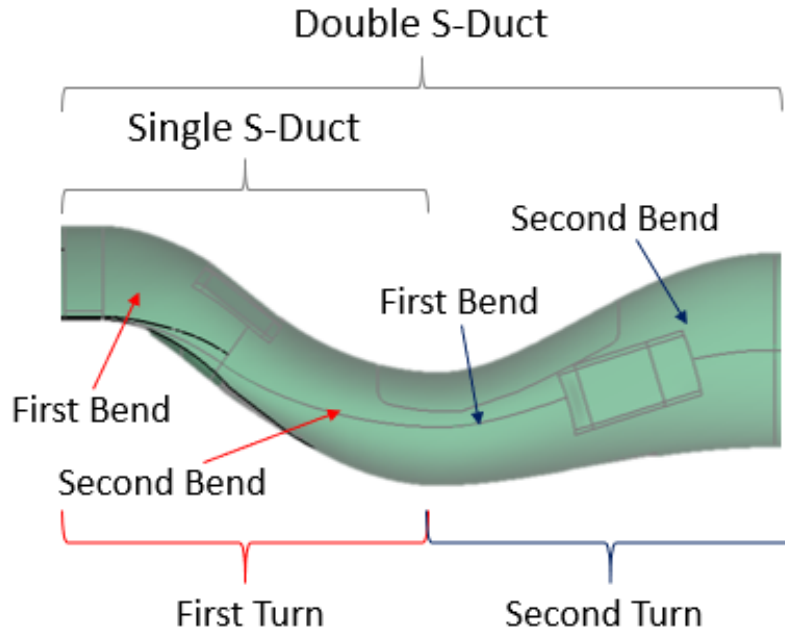


Figure 2.8: Double S-duct comprised of two single S-ducts

2.3.2 Fluid Flow. The flow is dominated by the momentum of the inflow that upon reaching the first bend, overshoots the lower bend and is forced downward along the upper surface creating an adverse pressure gradient on the upper surface and a favorable pressure gradient on the lower surface [1]. This results with an increased pressure coefficient on the upper surface with decelerating flow, and a corresponding decrease in pressure coefficient on the lower surface with accelerating flow. Also affected by the redirection of the flow is the boundary layer thickness, which is the thinnest on the top and thickest on the bottom, being attributed to the axial pressure gradients with accelerated flow near the bottom and slower flow near the top [1].

The decrease in fluid in the lower portion of the inlet is replaced by pressure driven flow perpendicular to the serpentine centerline from the boundary layers to the lower surface centerline [1]. Fluid is continually moved from the boundary layer into the low momentum region along the bottom surface convecting the low momentum region higher in the duct, while developing and exciting the two counter-rotating vortices [11]. Additionally, a local minimum of the total pressure is achieved in the duct [1].

The separation in the bottom part of the duct is caused by a blockage of the flow creating a favorable pressure gradient, accelerating the flow into the second bend of the single turn S-duct. Even though the flow was separated, a noticeable increase in static pressure was caused by the continued diffusion of the duct [1]. Figure 2.9 shows the flow traveling from left to right through a single turn S-duct with oil flow visualizations along the center plane. The separated region continues in the bottom of the duct until the flow reattaches as the region of reversed flow thins resulting from the continuous inflow of boundary layer fluid [11]. At this point, the region of low momentum fluid is lifted off of the wall developing into a region of low velocity and low total pressure in the bottom half of the duct [11].

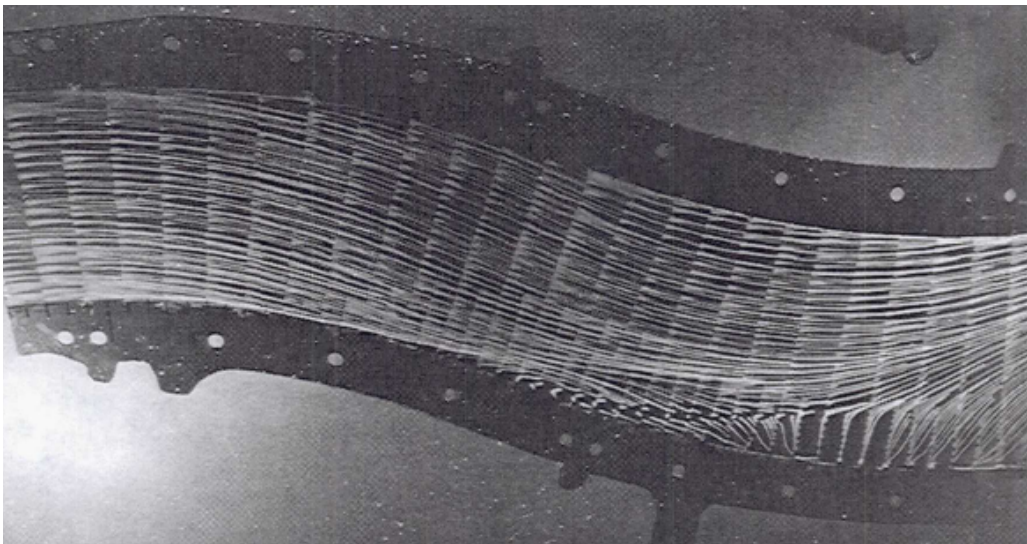


Figure 2.9: Oil flow visualization along a plate inserted along centerline plane within the single turn S-duct flow moving from left to right. (Figure from Wellborn *et al.* [11])

In the second bend of the single turn S-duct, the cross-flow pressure gradient begins to reverse with boundary layer flow flowing towards the upper centerline [11]. Although this is a similar trend to the lower surface in first bend, no large scale vortical structures or flow separation occurs on the upper surface in the second bend because the pressure gradients and boundary layer flow is not as strong as in the first bend [11]. This is shown in Figure 2.9 with flow along the second bend on the upper surface being attached without the indication of recirculating flow.

In the case of the double, or two turn, S-duct, the flow features observed by Wellborn *et al.* [1] within the first two bends comprising the single S-duct are repeated within the second turn. The second turn within a double S-duct is an upward offset, as opposed to the downward offset in the single turn S-duct in Figure 2.9. The first turn will still contain the separation region on the bottom surface in the second bend, but the separation in the second bend of the second turn is now on the upper surface. Therefore, much of the same flow features observed in the single turn S-duct will be experienced twice within the double turn S-duct as the driving physics remains the same in both turns.

2.3.3 Flow Distortion. Vortices within the flow create distortion of the flow by degrading the uniformity and the magnitude of the total pressure profile. The fully evolved pair of counter-rotating vortices in the lower half of the duct, like the vortices within the owl face of the first kind in Figure 2.7, continue to move low momentum fluid towards the duct's center extending above the centerline [11]. At this point the flow has returned to a downstream direction and the cross-stream static pressure gradients have subsided [1]. The difference in momentum in a cross-stream plane presents as a difference in velocity, each with an associated dynamic pressure. With a constant static pressure, the dynamic pressure variance across the plane results in a difference in total pressure across the plane. As the total pressure profile is not consistent across the plane, the flow is considered distorted. A simple calculation of

the inlet distortion is:

$$\text{Inlet Distortion} = \frac{(p_{t \max} - p_{t \min})}{p_{t \text{ avg}}} \quad (2.7)$$

where the difference in maximum and minimum total pressure, $p_{t \max}$ and $p_{t \min}$, is divided by the time averaged total pressure, $p_{t \text{ avg}}$ [16, p.425]. When the maximum and minimum total pressure values across the plane are the same, the inlet distortion would calculate results with the ideal value of zero. As the difference between the maximum and minimum total pressures increase, the inlet distortion also increases. The inlet distortion varies with mass flow rate and angle of attack, but a typical design point has an inlet distortion of less than 0.1 for a good inlet [17]. Increasing the angle of attack increases the inlet distortion as the flow is not perpendicular to the beginning of the duct [16]. For S-ducts, the increase of mass flow also increases the inlet distortion as the strength and size of the separated region increases [4]. Additionally, the total pressure of the flow is compared to the total pressure before the inlet in order to assess the total pressure recovery. The flow distortion resulting from a serpentine inlet lowers the engines surge line as in Figure 2.10, the line above which it is impossible to operate the engine without the possibility of damage to the engine and aircraft [16, p.164,425]. Further, the decrease in the surge line lowers the pressure ratios that can be obtained in turn lowering the possible thrust of the engine [16].

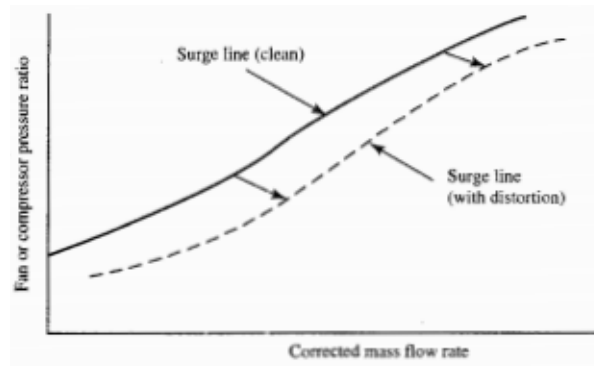


Figure 2.10: Inlet flow distortion effects (Figure from Mattingly [18, p.890])

Formal definitions and methods of determining both circumferential and radial flow distortion are outlined by the Society of Automotive Engineers [19]. The definition of circumferential distortion comes from the combination of intensity, extent, and multiple-per-revolution [19]. The intensity, or magnitude, of the distortion is the ratio of the value of the pressure defect for the ring divided by the face average pressure ($\Delta PC/P$), while the extent defines the portion of the ring that is below the average ring pressure [19]. Lastly, the multiple-per-revolution is the number of low pressure regions that exist around the ring [19]. The difference between the average pressure of a ring and the average pressure of the face ($\Delta PR/P$) defines the radial distortion of the ring, which can be positive or negative depending if the difference is above or below the face average respectively [19].

Diffusing serpentine inlet ducts have seen increased use since the first production application in the Boeing 727 as a means to locate the engine and inlet in more convenient locations. Although the number of different variations could be infinite, the general shape includes a duct that increases in cross sectional area while directing the flow downward then back. The fluid flow generally produces separated flow at the bottom part of the bend, which propagates into large counter-rotating vortices that create flow distortion at the compressor plate. Inlet designers characterize the distortion level to provide to the engine manufactures. In turn the engine manufactures determine if the level is acceptable for a particular engine. Different engines can have different levels that are determined “acceptable” and as such there is no definition of acceptable levels of distortion. The importance of this study is determining guidance to better predict the distortion observed for a given geometry based on modeling for implementation by inlet designers.

2.4 Reynolds Averaged Navier Stokes Turbulence Models

RANS turbulence models are commonly used for turbulent flows in CFD as they are computationally inexpensive compared methods like LES or DNS, resulting

from modeling rather than resolving the turbulent viscosity. This section lays out the assumptions, formulation, and limitations associated with RANS models.

2.4.1 Assumptions. In order to model the turbulence, RANS models solve for the Reynolds stress using the Boussinesq hypothesis for first order closures. The Reynolds stress is an additional term introduced by performing Reynolds or Farve averaging to the Navier-Stokes equations, resulting in a closure problem. The Boussinesq hypothesis is used to solve the closure problem and relates turbulent stresses as linearly proportional to mean strain rate via the eddy viscosity [20]. This relation is dominated by the observation that momentum transfer within turbulent flow is primarily driven by mixing resulting from the large energetic eddies [20]. The Boussinesq hypothesis relationship for incompressible Reynolds averaged equations can be expressed as

$$\tau_{ij} = 2\mu_T \bar{S}_{ij} - \frac{2}{3}\rho k \delta_{ij} \quad (2.8)$$

where τ_{ij} is the Reynolds stress tensor, μ_T is the eddy viscosity, \bar{S}_{ij} is the Reynolds averaged strain rate tensor, k is the turbulent kinetic energy, and δ_{ij} is the Kronecker delta [20].

Another assumption commonly applied is Morkovin's hypothesis. This hypothesis assumes that density fluctuations do not notably impact the turbulent boundary layer [20, p.220]. Morkovin's hypothesis is not applicable to hypersonic flows, compressible free shear layers, or combustion flows with heat transfer [20, p.220]. Yet, this hypothesis is still used in these applications to make the problems more tractable.

2.4.2 Formulation. The RANS equations are arrived by averaging the Navier Stokes equations. The first method was proposed by Reynolds in 1895 and thus the basis of the name Reynolds-Averaged Navier-Stokes [20, p.217]. Reynolds averaging can be applied by decomposing the governing equations into mean and fluctuating components, then solving for the mean component [20, p.217]. The breakdown into

the two components can be expressed as:

$$u = \bar{u} + u' \quad (2.9)$$

where the bar denotes the mean component and the prime denotes the fluctuating component. This breakdown can be applied to each velocity component, density, and pressure. The mean component can be achieved by three different averages: a time average, spatial average, or ensemble average, and thus is applicable for stationary turbulence [20, p.217]. Spatial averaging occurs across a control volume and thus is appropriate for homogenous turbulence [20, p.217]. Lastly, ensemble average is applied by averaging across a number of samples, which lends itself useful for general turbulence [20, p.218].

A different approach to Reynolds averaging can be applied to situations when the density is not constant by applying Favre averaging to the Navier-Stokes equations. This is of particular importance for flows where Morkovin's hypothesis is not applicable, when performing a Reynolds average would produce additional unknown terms including a triple product, but Favre decomposition prevents these additional terms. The Favre averaging takes the form:

$$\tilde{u} = \frac{\overline{\rho u}}{\bar{\rho}} \quad (2.10)$$

in which the tilde denotes the Favre averaged quantity and the bar represents averaged quantities.

The most common method is a combination of Reynolds averaging and Favre averaging to produce a model that is applicable to a wider range of flows. For this method, Reynolds averaging is applied to density and pressure, while all the remaining variables are Favre averaged for the compressible Navier-Stokes equations [20, p.220].

There are different types of first order RANS models including 0-equation, 1-equation, and 2-equation models. A 0-equation model such as Baldwin-Lomax model

is an algebraic model that does not solve for any additional transport. The most popular 1-equation model is the Spalart-Allmaras model, and it solves for the transport equation for eddy viscosity coded into the equation for turbulent kinematic viscosity. The Spalart-Allmaras model reasonably models adverse pressure gradients and flow separation and is best suited for airfoil and wing applications [20, p.225]. $k - \epsilon$ solves for the transport of turbulent kinetic energy k and the turbulent dissipation rate ϵ , and while likely the most popular 2-equation turbulence model, it requires a damping function in order to stay valid throughout the viscous sublayer [20, p.228]. $k - \omega$ is very similar to $k - \epsilon$ except solving for the specific rate of dissipation $\omega = \epsilon/k$, which has better resolution near walls [10, p.383]. The Mentor SST model combines the two through a blending function to take advantage of the strengths by using $k - \epsilon$ away from the wall and $k - \omega$ near the wall.

For second order closures, the Boussinesq hypothesis is no longer assumed, which results in the addition of six additional unknown terms. Reynolds Stress models are a second order closure RANS models that solve for the six unknown terms through six additional equations. This method includes empirical relations but it includes advection/diffusion flow history, normal stresses that behave appropriately to sudden changes in strain, and allows convection and production terms to respond to curvature, rotation, and stratification [20].

2.4.3 Limitations. There are several limitations to RANS models in addition to those previously listed for individual methods. First, RANS turbulence models have strict requirements for near wall spacing in order to accurately solve for the surface quantities and boundary layer. Typically, the first cell needs to have a height that is kept under one wall unit ($y^+ = 1$) [8]. The small spacing restricts the maximum timestep, as defined from Von Neuman stability analysis, which in turn increases the number of iterations run to reach a solution increasing the computational cost, core hours, needed for the simulation. Additionally, the maximum Reynolds number for the problem is limited due to a decreasing boundary layer thickness for higher

Reynolds number flows driving the requirement for more cells near the wall increasing the memory requirement for simulations above resource limitations.

The basis of first order turbulence closures, the Boussinesq hypothesis, is also limited with its applications. Specifically, it loses validity for flows with significant streamline curvature, boundary layer separation and reattachment, sudden change of mean strain rate, rotation and stratification, and secondary flows in ducts [20, p.223]. As these are all flow features present in the S-duct, a RANS turbulence model would be a poor choice for modeling the flow.

This section provided a brief overview of RANS turbulence models, while there is much more on the topic, the main points relative to the current study were presented. The assumptions allow for RANS models to resolve less of the turbulent eddies than LES or DNS, which allows for cheaper and faster computational simulations. Conversely, these assumptions come at a cost of lower fidelity and the potential for inaccurate solutions if applied incorrectly. Modifying the governing equations through Reynolds averaging, Favre averaging, or the combination of the two is core to the methodology of RANS methods, but each average has its uses and limitations. In regards to a diffusing S-duct, the limitations for RANS have thus far prevented accurate predictions of the flow distortion, total pressure recovery, and separation locations from a single model [3]. A more detailed discussion on recent applications of RANS models to the diffusing S-duct can be found in Section 2.7.

2.5 Large Eddy Simulation Turbulence Models

LES serves itself as a turbulence modeling alternative that is less cost prohibitive than DNS but can yield more accurate results than RANS models. DNS does not use a turbulence model and resolves all temporal and spatial scales with the turbulent flow. For this reason DNS requires cells on order of the Kolomogorov length scale and the time step to match the Kolomogorov time scale. The primary difference between DNS and LES is LES resolves turbulent energy containing scales that are larger than

a filtered size, usually on the order of the cell size, and models the scales smaller than the resolved scales using a sub-grid stress (SGS) model. The observation that small scales of turbulence are relatively isotropic allows for a simple SGS model to compute rather than fully resolving it making LES possible [21]. Energy containing turbulent eddies are eddies larger than $1/6$ of the integral length scale, which provides a scale for the cell size [10, p.184]. For the S-duct in this study, this falls on the order of 10 to 100 micrometers. In order to compute appropriate wall shear and heat transfer for the boundary layer at the wall within a LES turbulence model, Wall-Resolved LES or Wall-Modeled LES can be applied to account for the boundary layer. Wall-Modeled LES can be classified as Hybrid RANS/LES method or Wall-stress model method [22].

2.5.1 Turbulence Scale Filtering. Defining the separation between resolved and modeled scales can be completed using either an explicit or implicit method. The explicit method uses a filtering equation like a tophat, sharp Fourier cut-off, or Gaussian filter to separate large and small scale turbulence [20, p.236-237]. Implicit turbulence scale separation can be achieved by allowing the scale of the grid size to be the filter [21]. Note that this implicit filtering is different than Implicit Large Eddy Simulation (ILES) which uses numerical dissipation within the model to act as a subgrid model without the use of an actual subgrid model [23]. While the implicit filtering is less computationally demanding by not needing additional equations, it requires a carefully constructed grid where all cells are roughly cubes of the same size [21]. The need for cubes stems from the fact that the smallest eddy that can fully be resolved by the cell must be larger than the cell, therefore, the largest dimension of the cube defines the scale that can be resolved. Defining isotropic turbulence scales as scales that are not the large energy containing scales and are on the order of less than $1/6$ of the integral length scales, sets a maximum size that the cells must be to resolve the flow [10, p.184]. The size of the integral scale is specific to the generation of the turbulence and thus could have different sizes for different types of flow conditions and geometries. In the S-duct used in this study, the separation was considered to be

between 10 to 100 micrometers. For this same reason, the explicit method is limited to having a filter size larger than the maximum cell size in the domain. The largest difference between the methods is that the explicit method can define a universal filter length to be used everywhere while the implicit method can vary from cell to cell if they are not of identical sizes, but the explicit method comes at a cost of increased coding complexity and computational time. Both methods separate scales that will be resolved through the Navier-Stokes equations and scales that will be modeled through subgrid scale models then combined together to account for all scales in the flow.

2.5.2 Sub-Grid Stress Models. Once filtered, the SGS model dissipates the energy in length scales smaller than resolved length scales to heat from friction. The Smagorinsky and Vreman SGS models are presented along with their advantages and limitations.

The stress tensor is comprised of the pressure and viscous terms from the filtered momentum equation. The subgrid scale stress tensor is the tensor used for the scales not resolved by the model. Valid models of the subgrid scale stress tensor meet four general restrictions [23]. First, the interaction between resolved and subgrid scales is purely energetic to balance the transfer of energy, and the amount of energy in the subgrid scales is enough to describe the unresolved scales [23]. Figure 2.11 shows this transfer of energy from resolved to subgrid scales. Second, the method of transfer of energy from the resolved to unresolved scales is similar to mechanism of the molecular viscosity in the diffusion term, which is known as the Boussinesq Hypothesis [23]. The application of this hypothesis results in the subgrid stress tensor to be modeled as:

$$\tau_{ij}^d = \tau_{ij} - \frac{1}{3}\delta_{ij}\tau_{kk} = -\bar{\rho}\nu_T(\widetilde{S}_{ij} - \frac{1}{3}\delta_{ij}\widetilde{S}_{kk}) \quad (2.11)$$

in which τ_{ij} is the subgrid stress tensor, S_{ij} is the filtered strain rate tensor, and the subgrid viscosity ν_T are used [23]. Third, scales are either resolved or subgrid and there is a complete separation between them, indicating that the subgrid viscosity is a property of the flow, not the fluctuating fluid [23]. The sharp cutoff between

resolved and subgrid scales in Figure 2.11 further emphasizes this point. Lastly, no accumulation exists at any frequency and there is constant energy equilibrium, and the shape of the energy spectrum remains unchanged with time [23]. This implies that the energy transferred into the subgrid scales is equal to the amount of energy dissipated to heat through viscous dissipation. Figure 2.11 represents this as a linear continuous line passing across the filter width without a jump discontinuity.

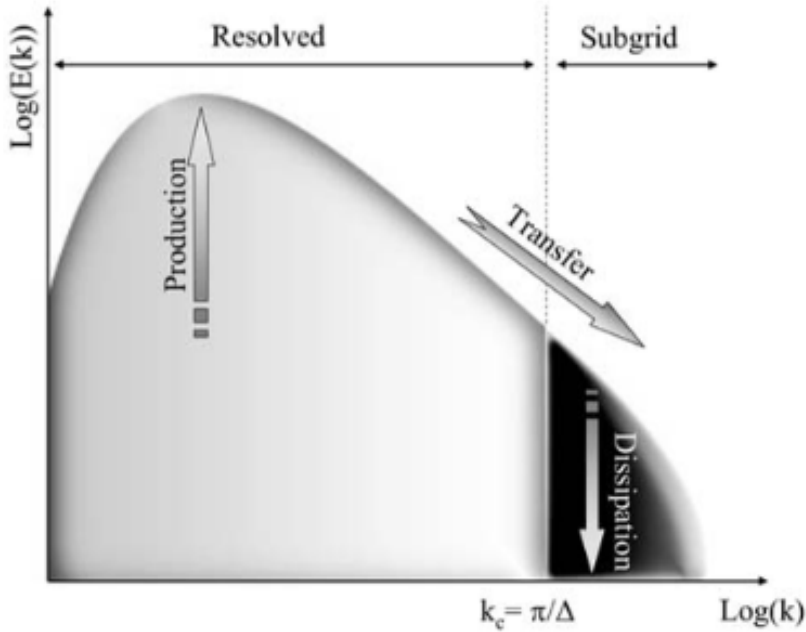


Figure 2.11: Spectrum of homogeneous turbulence with a filter separating resolved and subgrid scales (Figure from Garnier, Adams, and Sagaut *et al.* [23])

The Smagorinsky SGS model is a commonly applied SGS model within LES applications. The model is easy to implement within a LES code, which coupled with its validation and widespread use have set a precedent with the selection of this model. The Smagorinsky model was originally developed for use in meteorological applications, and is only capable of handling turbulent flows, meaning it cannot handle regions of the model that are laminar or transitional [24]. The Smagorinsky model uses the Boussinesq relationship, which assumes that the turbulent stress is linearly proportional to the mean strain rate and can be modeled with eddy viscosity, similar

to the viscous stress tensor [20, p.241]. The algebraic model is expressed as:

$$\nu_T = (C_S \Delta)^2 |\bar{S}| \quad (2.12)$$

where C_S is the Smagorinsky constant, Δ being the filter width defined as two times the average grid size or $\Delta = 2(\Delta_{x_1} \Delta_{x_2} \Delta_{x_3})^{1/3}$, and $|\bar{S}|$ as the magnitude of the strain rate tensor defined as $|\bar{S}| = (2\bar{S}_{ij}\bar{S}_{ij})^{1/2}$ [20, p.241]. Further, the strain rate tensor can be expanded using Favre averaged values as:

$$\widetilde{S}_{ij} = \frac{1}{2} \left(\frac{\partial \widetilde{u}_i}{\partial x_j} + \frac{\partial \widetilde{u}_j}{\partial x_i} \right) \quad (2.13)$$

in which u_i are the velocity components, the tilde denoting Favre averaged values, and x_i are the directional components. The Smagorinsky constant, C_S , proportionally relates the characteristic filtered rate of strain to the filter width in calculating the eddy viscosity [10]. Theoretically, $C_S = 0.18$ for homogeneous isotropic turbulence as defined by $C_S = \frac{1}{\pi} \left(\frac{3k_o}{2} \right)^{-3/4}$ with the use of the Kolomogorov constant $k_o = 1.4$ [23]. In practice, C_S can be tailored to the problem ranging from 0.1 to 0.2 in order to prevent the mismatch of energy transfer from the resolved to the modeled scales [23].

The primary drawbacks to the Smagorinsky model are that it is too dissipative in laminar regions, special care is required near walls and transitional regions, and the Smagorinsky constant within the model is not uniquely defined [20, p.241]. Another problem the Smagorinsky model has is that the eddy viscosity does not appropriately vanish at the wall as physics requires [21]. As a result of the models shortcomings, especially being overallly dissipative, and considering it has only been validated on simple decaying turbulence flows, it is not recommended for general LES simulations [21].

To expand the capability of the Smagorinsky model and address some of its limitations, Germano *et al.* introduced a dynamic procedure that prevents the mismatch of energy in the cascade at the filter width [25]. A test filter larger than the subgrid

scale filter is used to assess the slope of the turbulent kinetic energy spectrum, as the slope is constant through the region of the two filters [25]. By knowing the actual slope of the energy transfer, the constant can be solved for to allow the dissipation of the subgrid scale model to match at the filter width. The dynamic Smagorinsky model replaces C_S with C_d as shown in:

$$\nu_T = C_d(\vec{r}, t)\Delta^2|\bar{S}| \quad (2.14)$$

with the dynamic constant, C_d calculated through the dynamic procedure being a function of time and position [25]. The full derivation on how to calculate $C_d(\vec{r}, t)$ is provided by Blazek [20, p.241-242]. To prevent instabilities in the model, an *ad hoc* clipping method is applied following the filtering operations and ensemble averaging in homogeneous directions to remove negative eddy viscosities from occurring [5]. The additional equations and explicit filtering needed to solve for the slope through the dynamic procedure increases the computational cost by taking more computational core hours to solve.

To overcome the limitations of the Smagorinsky model and the increased computation time required by the dynamic Smagorinsky model, Vreman developed a model based of the Smagorinsky model as:

$$\nu_T = c\sqrt{\frac{B_\beta}{\alpha_{ij}\alpha_{ij}}} \quad (2.15)$$

where the components α_{ij} , β_{ij} , B_β are defined as:

$$\alpha_{ij} = \partial_i \bar{u}_j = \frac{\partial \bar{u}_j}{\partial x_i} \quad (2.16)$$

$$\beta_{ij} = \Delta_m^2 \alpha_{mi} \alpha_{mj} \quad (2.17)$$

$$B_\beta = \beta_{11}\beta_{22} - \beta_{12}^2 + \beta_{11}\beta_{33} - \beta_{13}^2 + \beta_{22}\beta_{33} - \beta_{23}^2 \quad (2.18)$$

to better account account for appropriate dissipation of the model [5]. The Vreman constant is defined as $c = 2.5c_s^2$ [5]. The Vreman model can handle laminar, transitional, and turbulent regions like the dynamic Smagorinsky model and produces similar results, but the Vreman model computational effort costs 50% of the dynamic Smagorinsky model [5]. Vreman verified and validated his model against the Smagorinsky model, dynamic Smagorinsky model, and DNS data, to prove that his model performs as well as the dynamic Smagorinsky model in capturing the solution obtained by DNS [5]. In every case, the Vreman model outperformed the standard Smagorinsky model [5]. While the method presented was run using second order numerical methods, it was noted that higher order numerics and applying a dynamic procedure would likely increase the accuracy of the model [5]. Chapter V builds from these points through derivation and fourth-order application of a dynamic Vreman model.

2.5.3 Large Eddy Simulation Models. The three main categories of LES that will be discussed in this section are Wall-Resolved LES, Wall-Modeled LES, and Hybrid RANS/LES as shown in Figure 2.12.

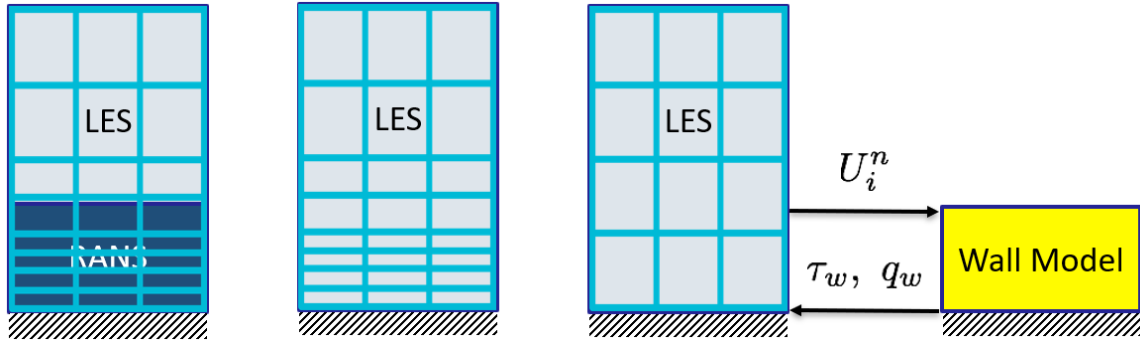


Figure 2.12: Comparison of Hybrid RAN/LES (left), Wall-Resolved LES (center), and Wall-Modeled LES (right)

Wall-Resolved LES decreases the size of the cells closer to a surface, clustering the cells to capture the boundary layer, which allows for the code to resolve the smaller scales present near the wall as shown in the middle image of Figure 2.12. In general the WR-LES will fully resolve 80% of the energy everywhere in the flow, including

Table 2.1: Grid scaling requirements turbulent boundary layers with high Reynolds numbers (Table from Choi and Moin [27])

Direct Numerical Simulation	$N \approx Re^{37/14}$
Wall-Resolved LES	$N \approx Re^{13/7}$
Wall-Modeled LES	$N \approx Re$

the near wall region [10, p.560]. The remaining 20% of the energy is computed in the SGS model and is used on the energy scales where the turbulent eddies are isotropic. Isotropic turbulence scales can be considered as length scales less than 1/6 of the integral length scale [10, p.184]. The spacing at the wall requires $y^+ = 1$ for the maximum height of the first cell on the wall drastically increasing the number of overall cells needed in the domain, approaching the number of cells needed for DNS [26]. As the Reynolds number increases, the turbulent length scales decrease, in turn requiring smaller cell sizes to resolve the eddies. This scaling is summarized by Choi and Moin in Table 2.1 [27]. It shows how the computational requirement, in number of grid points N , scales based on the scaling of skin friction at high Reynolds numbers Re [27]. Based on this table, most high Reynolds numbers of engineering interest become unfeasible for DNS and WR-LES, but are still obtainable with WM-LES. Further, by applying Von Neumann stability analysis, it can be deduced that the smaller cells require smaller time steps. The combination of small cells and small step sizes results in an expensive calculation that approaches the cost of DNS [26].

The Wall-Modeled LES tries to maintain a lower number of overall cells and obtain a smaller computational cost by resolving 80% of the energy away from the wall but not the energy in the near wall region [10, p.560]. Kawai and Larsson separate WM-LES into two categories, models that model wall shear stress directly and Hybrid RANS/LES models [22]. One advantage of WM-LES is the ability to assess problems with larger Reynolds numbers than what is achievable using WR-LES due to computational cost [10, p.637].

Wall-stress modeling approach to WM-LES includes formally defining LES all the way to the wall but solved on a grid that resolves only the outer layer motion [22],

as shown in the right image of Figure 2.12. The grid being inherently too coarse to resolve the flow at the wall then uses a wall-stress model to resolve the wall shear stress and heat transfer at the wall. The wall-stress models can be further classified into models based on mathematical or physical arguments [26]. Math-based wall-stress models apply control theory and mathematical filtering through mathematical arguments to predict slip velocity and wall stresses [28]. Physics-based models differ by relying on the physical arguments of the conservation of momentum in a nearly parallel shear flow [28]. Physics-based wall-stress models can either be equilibrium with exact balancing of the convection and pressure-gradient terms or non-equilibrium that accounts for all of the physics at an increased computational cost [26]. The wall-stress models use the data from a probe off of the wall to provide flow information to the model that computes the shear stress and heat transfer at the wall. Those values are returned to the LES solver in the form of boundary conditions at the wall. The probe placement can be placed within the cell adjacent to the wall, but increased accuracy of skin friction predictions is obtained when the probe is placed a few cells off of the wall [22].

The Hybrid RANS/LES uses LES to resolve the large scale turbulent energy within the region away from the wall but then models the region at the wall with a RANS model, as shown in the left image of Figure 2.12. Differing from a purely RANS approach, the movement of the large scale eddies are captured [28]. While the energetic energies and their associated frequencies are resolved away from the wall, the information is lost near the wall within the RANS model. The grid requirements for Hybrid RANS/LES requires a $y^+ = 1$ for the first cell off of the wall for the RANS model and growing from the wall. Although the grid is like that required for WR-LES, the act of using the RANS model near the wall reduces the computation time that would be required to fully resolve the flow.

Three common Hybrid RANS/LES models are DES, DDES, and IDDES. In DES, the distance from the solid surface is used as a switch between RANS at the wall and LES in the separated region away from the wall [20]. DDES includes an

enhancement to DES includes a shielding function that prevents the transition from RANS to LES to occur within an attached boundary layer as a result of the grid [29]. A further enhancement was made within IDDES where the model uses wall modeled LES if the inflow contains resolved eddy content and normal DDES in all other locations [30].

The ability to resolve the energy containing eddies while modeling smaller eddies produces improved turbulence simulations over RANS models that do not resolve any of the eddies. While not as accurate as DNS, LES comes at a lower computational cost than DNS. To achieve LES, a filter width needs to be set in order to separate modeled or resolved eddies. For modeling eddies smaller than the filter, a Vreman model is better than a Smagorinsky model because of reduced dissipation it provides. For this study, the primary focus is using a WM-LES, but a Hybrid RANS/LES model is also run for comparison.

2.6 Serpentine Inlet Testing

Wind tunnel testing of diffusing serpentine ducts has primarily focused on producing data sets to be used for turbulence modeling comparison and development. The largest tests, conducted by the National Aeronautics and Space Administration (NASA) and the French Aerospace Lab ONERA, were conducted on representative S-ducts that produce the complex flow features. While this type of geometry does not mimic the geometry used in this study, the flow phenomena were much the same and applicable to the understanding of what is to be modeled.

2.6.1 NASA Experiment. In 1992, NASA's Lewis Research Center conducted experimentation on a diffusing S-duct to provide an understanding of the complex flow and provide a data set for use in comparing CFD models in order to improve the modeling capability. The study was brought about by modeling studies that suggested the formation of counter-rotating vortices within the S-duct, but little information and data had been collected on this type of flow features [1]. The single

turn S-duct design selected by Wellborn *et al.* incorporated complex three dimensional flow features, like separation, that are typically found in S-duct configurations. The test setup in Figure 2.13 included a settling chamber complete with wires, meshes and screen to ensure a low turbulence intensity at the inlet entrance, a single turn S-duct test section, and a mass flow plug prior to the blow down exhaust used to control the flow rate.

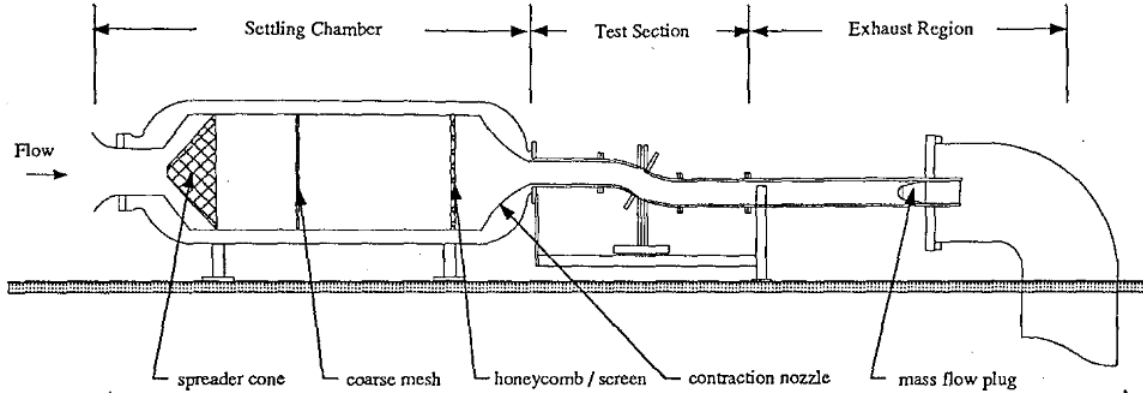


Figure 2.13: Experimental setup used by Wellborn *et al.* (Figure from Wellborn *et al.* [1])

The precision made S-duct had a 10.21 cm inlet radius and a 12.57 cm exit radius. The S-duct was instrumented to include five cross-flow measurement planes perpendicular to the centerline shown in Figure 2.14 with pressure taps located around each plane and holes for a probe to be inserted to characterize the flow. A five hole probe was used in Planes B-E to capture total pressure, static pressure, and velocity components. Plane A used a three hole probe because the flow was only in one direction. The probe was inserted at various lengths to capture measurements throughout the plane. In addition, static pressure taps were placed running lengthwise down the duct at 10° off of the top centerline, the side of the duct, and 10° off of the bottom centerline, totaling 220 taps. The data collected was averaged across a number of measurements.

For the experiment, the freestream flow along the centerline of the duct at the inlet was measured at 0.6 Mach, which yielded a $Re = 2.6 \times 10^6$ when using the inlet

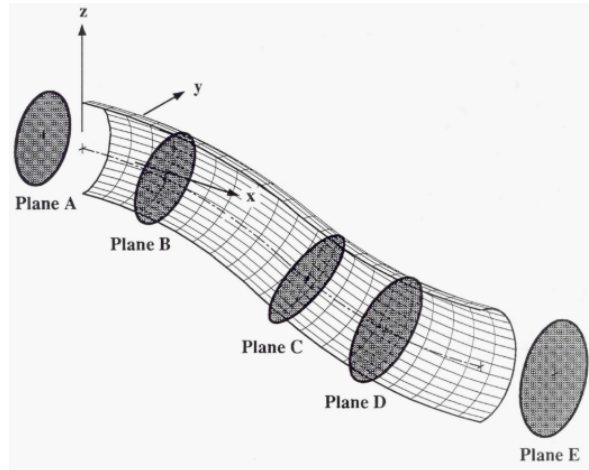


Figure 2.14: Plane locations throughout the S-duct (Figure from Wellborn *et al.* [11])

diameter as the reference length. The inflow turbulence level was determined to be 0.65% based upon hot wire measurements collected at 50kHz along the centerline [31].

To assess the near surface flow, oil flow visualizations were obtained by applying a matrix of small oil dots consisting of a fluorescent dye mixed into 140 weight oil, then running the experiment for 10 minutes allowing the surface flow features to fully develop. There were three main conclusions that Wellborn *et al.* were able to obtain from the oil flow measurements. First, the flow was symmetric between the right and left halves of the tunnel. To reach this conclusion, different color dye was used on each half of the duct, and after the experiment the different colors remained separate from each other without mixing. One further test for symmetry was conducted using a splitter plate that divided the two halves, and the results matched the surface oil flows without the plate, even with the additional shear stress from the plate. Second, Figure 2.15 shows a large region of separated flow existed consisting of two saddle points on the bottom centerline, corresponding to the attachment and reattachment point, and two spiral nodes, one being on each symmetric half separated by the bottom centerline. Third, boundary layer cross flow was observed. The first bend had streaks dropping towards the lower surface and then diverging in the second bend, which is noticeable in Figure 2.16.

The consolidation of the axial and cross stream wall pressure tap data is presented in Figure 2.17. The axial pressures on the left of the figure show the gradual rise in pressure coefficients with the distinct flatline along the bottom and side of the duct and accompanying drop along the upper surface indicating the existence of separated flow as indicated on the graph.

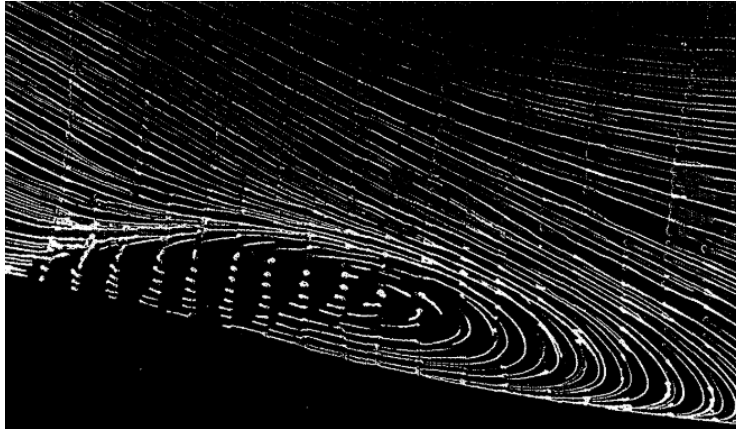


Figure 2.15: Close view of the oil flow visualization in the separation region on one half of the duct (Figure from Wellborn *et al.* [1])

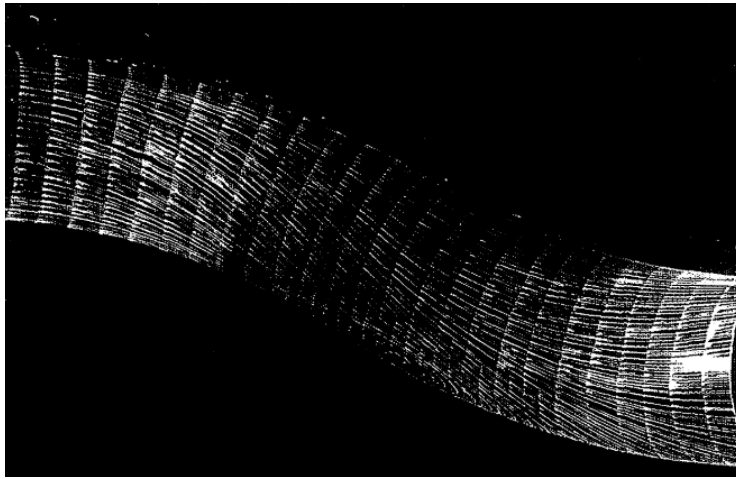


Figure 2.16: Oil flow visualization on one half of the S-duct (Figure from Wellborn *et al.* [1])

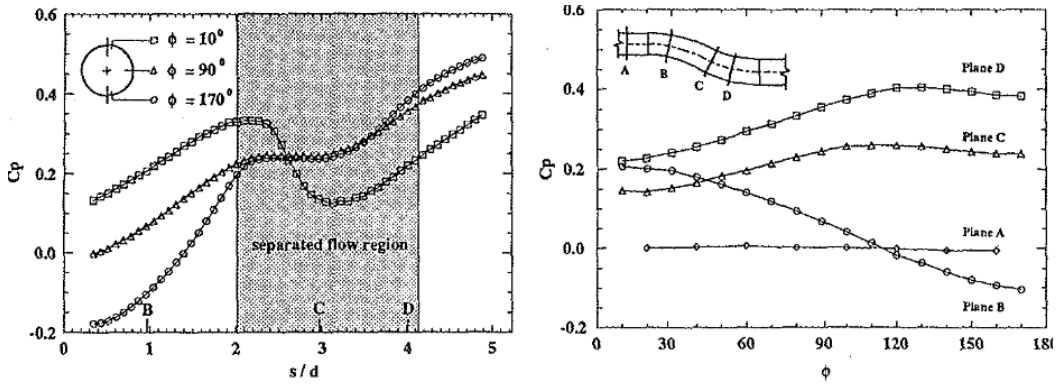


Figure 2.17: Pressure along the axial and plane surfaces of the S-duct (Figure from Wellborn *et al.* [1])

In addition to the right graph in Figure 2.17, Figures 2.18 and 2.19 show the pressure distribution and cross flow at each plane to assess the flow features in the S-duct. Each plane will be discussed based upon the results by Wellborn *et al.* in the NASA Report [11].

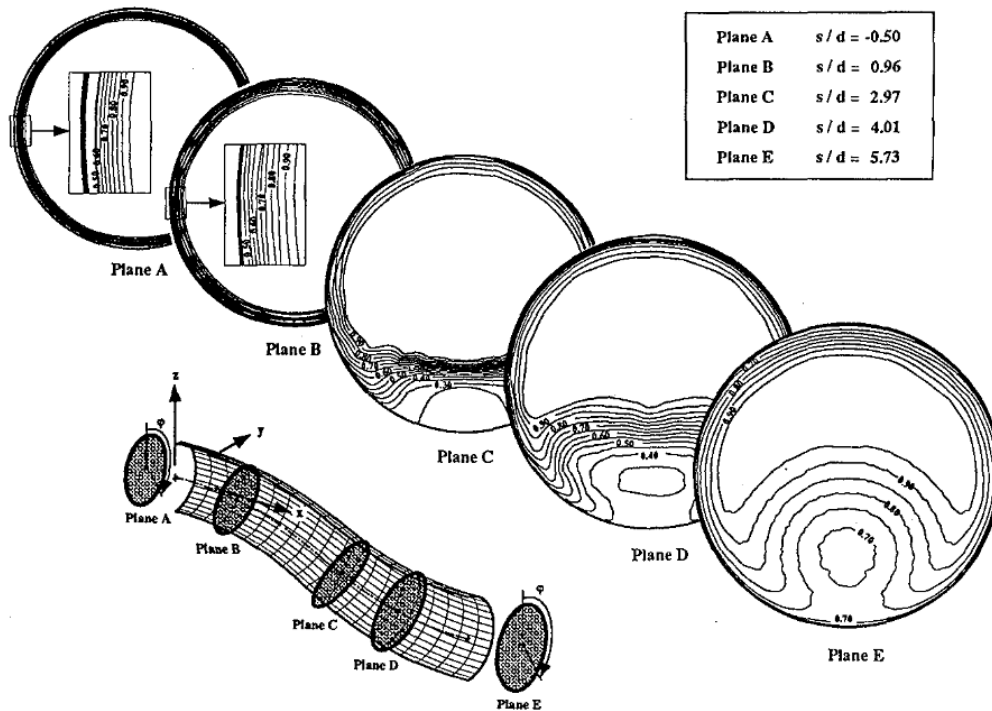


Figure 2.18: Pressure distribution on across the planes of the S-duct (Figure from Wellborn *et al.* [1])

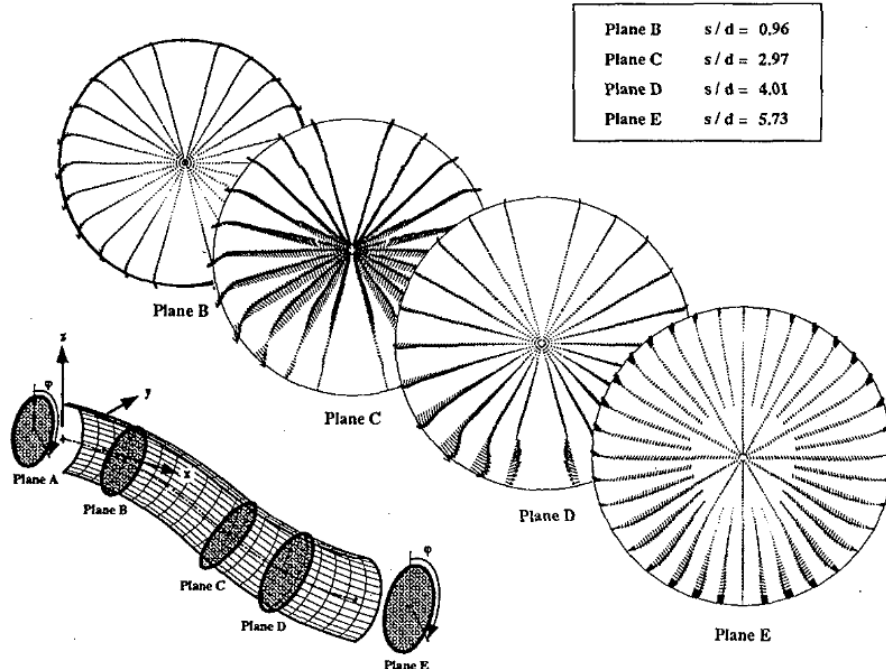


Figure 2.19: Transverse Mach component of velocity across the planes of the S-duct (Figure from Wellborn *et al.* [1])

Starting with Plane B, the cross-stream static pressure gradients developed as a result of the core flow adapting to the geometry [11]. The maximum static pressure was measured on the top surface and minimum on the lower surface. Additionally, the boundary layer thickness varied around Plane B with the thickest on the top centerline and the thinnest on the lower centerline that was attributed to the axial pressure gradients with accelerated flow near the bottom surface and slower flow on the top surface [1]. Although cross-stream flows driven by pressure gradients existed, the large region of low momentum fluid at the bottom of the surface did not develop until Plane C [1].

Plane C is located within the second bend. There was a reversal of the cross-stream static pressure gradients that existed in Plane B [11]. A region of relatively constant local minimum static pressure was measured in the lower half of the duct [11]. This indicated a region of small fluctuations of velocity indicative of a separation region [11]. Fluid was moved from the boundary later into the low momentum region convection the low momentum region higher in the duct, while exciting the two

counter-rotating vortices [11]. As a result of the separation creating a blockage in the flow accompanied with an adverse streamwise pressure gradient and the vortical structures, the flow along the centerline at the plane was directed upward, which was captured in the measurements [11].

Moving farther down the S-duct, Plane D shows increased flow development of the low velocity and low total pressure region in the bottom half of the duct through measurements of the total pressure [11]. As a result of the low momentum fluid being lifted off of the wall, a region of near zero velocity was observed away from the wall [11]. Like in Plane C, the gradient driven cross flow forcing boundary layer fluid into the low momentum region still existed, with the continued presence of the strong counter-rotating vortices, but the global flow returned to a more streamwise direction [11]. The pressure gradients begin to reverse, and the boundary layer near the upper surface begins to cross flow upwards towards the upper centerline, present in Figure 2.19 [11]. Unlike the large scale vortical structure that was observed on the lower surface resulting from this phenomenon in Plane C, no large scale vortical structure was observed on the upper surface [11].

The last plane, Plane E, shows that the pair of counter-rotating vortices have fully evolved in the lower half and they continue to move low momentum fluid towards the duct's center, even extending the region into the upper half [11]. The existence of the low momentum region reduced the uniformity of the total pressure across the duct [11]. Referring back to Equation 2.7, a larger change in uniformity increased the value in the numerator subsequently increasing the inlet distortion.

2.6.2 ONERA Experiment. Over 20 years after the experiments performed by Wellborn *et al.* at NASA, the French Aerospace Lab ONERA in conjunction with Boeing conducted experiments on a scaled model of NASA's original S-duct design, and ONERA's setup is displayed in Figure 2.20. The experiment used a fine copper wire at the end of the bellmouth to ensure that flow was fully turbulent [2]. While Delot and Scharnhorst acknowledged the work done by NASA, there was the desire

for increased flow distortion and pressure recovery data collected with a 40 pressure port Aerodynamic Interface Plane (AIP) positioned downstream of the S-duct, that based on its size required the model to be scaled [2].

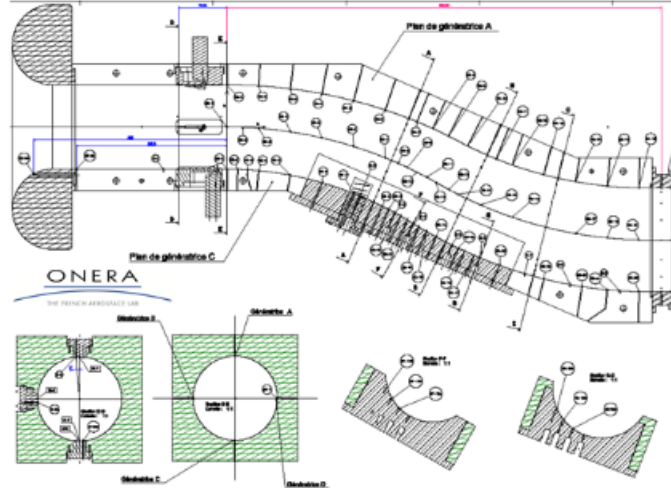


Figure 2.20: Scaled S-duct model used by ONERA and Boeing (Figure from Delot and Scharnhorst [2])

Like the NASA experiments, both axial and circumferential pressure ports were located on the surface of the S-duct, as shown in Figure 2.21 [2]. The three circumferential planes were similar to Planes B through D in the NASA experiments. The axial pressure ports were located at the top centerline, bottom centerline and along the mid side, with the first two differing from the 10° offset from centerlines done by NASA [2].

Two primary test cases were considered during testing. Case 1 consisted of a throat Mach number of 0.6 resulting in a Reynolds number of 1.4×10^6 and Case 2 had a slightly slower throat Mach number of 0.4 reducing the Reynolds number to 1.0×10^6 [2]. The cases are referred to as Baseline Flow Conditions and Optional Flow Conditions, because they were used for a large modeling study discussed in Section 2.7.

Figure 2.22 shows Delot and Scharnhorst's axial pressure profiles along the surface of the S-duct. Much like NASA's results, the wall static pressure increased then

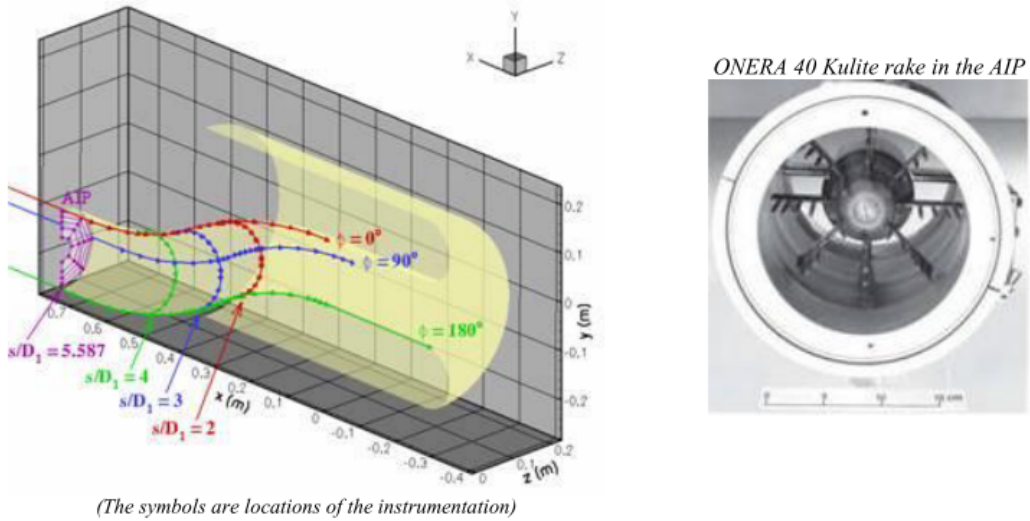


Figure 2.21: S-duct instrumentation (Figure from Delot and Scharnhorst [2])

decreased along the upper surface, red line in Figure 2.22, as a result of the flow decelerating then accelerating through the bends. The flat plateau in the static pressure on the lower surface and on the side of the duct, the green and blue lines respectively in Figure 2.22, indicates the large flow separation.

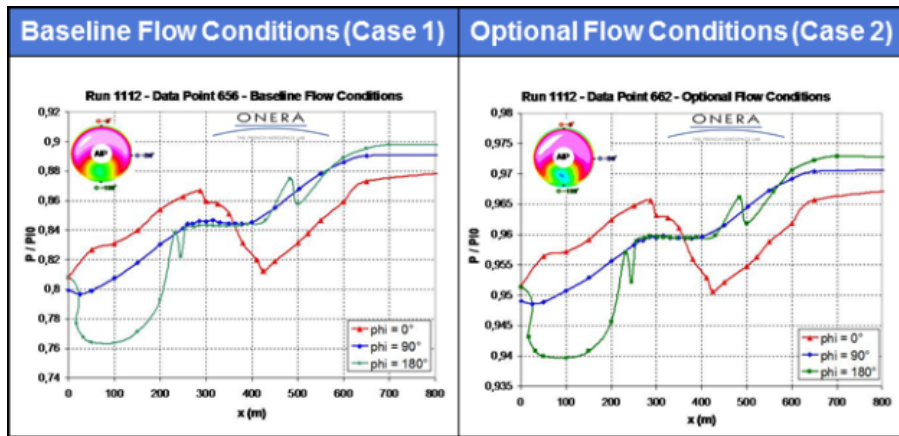


Figure 2.22: Axial static pressure along the S-duct (Figure from Delot and Scharnhorst [2])

The measurements of the static pressure ports located circumferentially around the S-duct at Positions 2, 3, and 4, as indicated in Figure 2.20, are presented in Figure 2.23. The wall static pressure was non uniform at each location, wherein the lowest

static pressure corresponds to the highest velocities that were located at the bottom of Position 2 and top of Positions 3 and 4, as expected [2].

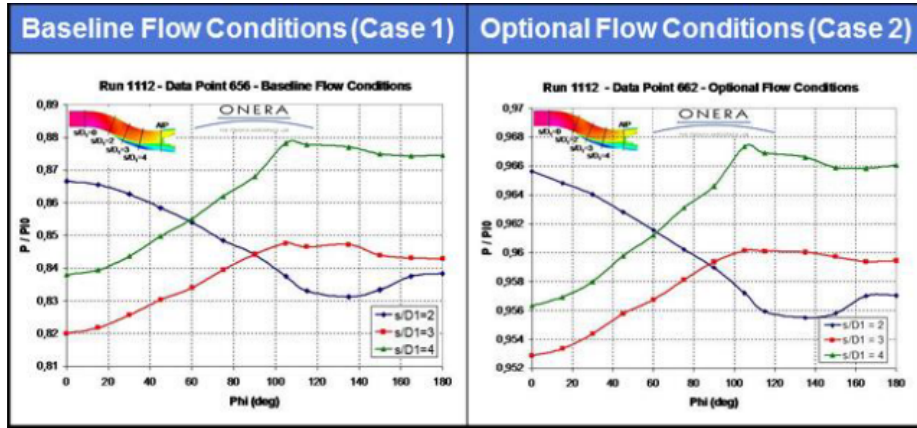


Figure 2.23: Circumferential static pressure along the S-duct (Figure from Delot and Scharnhorst [2])

Using the data from the 40 pressure taps on the AIP, Figure 2.24 was created by Delot and Scharnhorst to display the flow distortion in terms of the total pressure recovery [2]. Excluding the white circle in the center of the Figure 2.24, the white and light pink region dominating the upper region show the greatest pressure recovery at and near one, which is the highest recovery that can be obtained. As a result of the counter-rotating vortical structures conducting the lower momentum flow upwards, there was a decrease in the pressure recovery in the lower half of the duct of Figure 2.24. The resulting large color gradients in the lower half of Figure 2.24 highlight the flow distortion.

In addition to presenting the plots of the total pressure recovery at the AIP, the circumferential and radial distortions were classified separately. These two parameters were selected as they are of primary interest to engine suppliers to ensure the engine can operate with the given conditions [2]. Table 2.2 presents the distortion coefficients obtained from the two test cases. While the specific numbers for the distortion of the two cases are not important by themselves, it is important to note that Case 1 provided greater distortion. The case with a greater flow distortion is more stressing case for computational modeling because it contains more complex flow phenomena that is

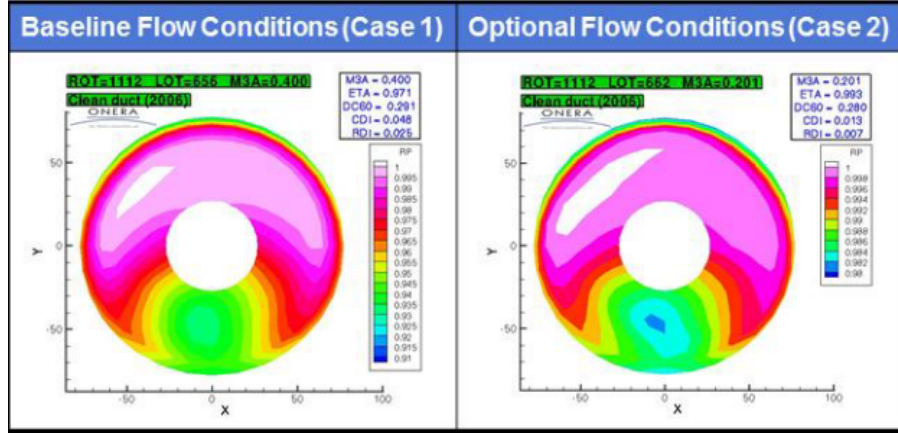


Figure 2.24: Total pressure recovery and flow distortion at the AIP following S-duct (Figure from Delot and Scharnhorst [2])

Table 2.2: Distortion coefficients of the ONERA test cases.

Case	Circumferential	Radial
1	0.0483	0.0251
2	0.0126	0.0070

more difficult to accurately predict in turbulence modeling. Therefore it was selected to provide a challenging problem used in the computational study discussed in Section 2.7. Additionally, as noted in Section 2.3.3, specific numbers of flow distortion are best used in comparison to each other because exact ramifications of the value are engine dependent with no defined level of an acceptable flow distortion.

The NASA and ONERA testing both were conducted on the same Wellborn S-duct design, and were focused on generating data for comparison to modeling. Further testing is ongoing with the inclusion of flow control devices in the ONERA setup, but flow control devices used to reduce distortion are outside of the current study. While both studies generated information on the pressure recovery and distortion of the flow through the duct, the values are not important for a design perspective because they will not be used with an engine, but they are important in comparing modeling techniques to predict the flow.

Section 2.7 includes modeling attempts made on the Wellborn and ONERA geometries and compared to the test data. In this study, the flow is further complicated

by adding a second turn to the S-duct to complete a drop down-rise up design as shown in Figure 2.8. The previous modeling attempts made on double S-ducts are also included within Section 2.7 from which this study builds upon.

2.7 Current Serpentine Inlet Turbulence Modeling

In conjunction to the 1991 NASA experiment, Wellborn *et al.* conducted modeling of the S-duct using a parabolized Navier-Stokes (PNS) algorithm, a form of RANS model. The PNS algorithm was used as it provides more resolution than potential flow equations but does not require solving the full Navier-Stokes equations [11]. As the flow occurs within the subsonic realm, the PNS equations can be refined with the acknowledgement that for ducted flows a predominant flow direction exists allowing for the effect of momentum diffusion in the streamwise direction to be negligible resulting in partially-parabolized Navier-Stokes (P-PNS) equations [11]. The P-PNS equations derived by Wellborn *et al.* were solved using an alternating-directional implicit (ADI) algorithm from a Crank-Nicolson spatial differencing [11]. The viscous flow solutions were obtained using an O-grid with 77 x 49 x 49 grid points in the streamwise, circumferential, and radial directions respectively, with clustering added near the wall as shown in Figure 2.25 to help resolve flow separation [11]. By today's standards this grid is nowhere dense enough to resolve the flow, but in 1991 they were largely restricted by computational memory.

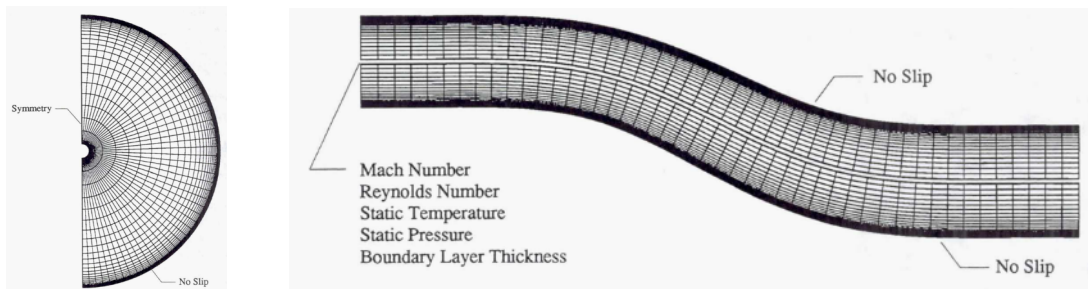


Figure 2.25: Computational O-grid viscous mesh (Figure from Wellborn *et al.* [11])

The comparison of the model and experiments in Figure 2.26 shows similar trends, but differences in values. When assessing the axial static pressure coefficients,

the largest discrepancies occur after the second bend of the duct, where the model predicts a separated region that occurs later than measured [11]. Wellborn *et al.* noted that the P-PNS results were similar to the results generated using a fully-elliptic Navier-Stokes algorithm with a $k - \epsilon$ turbulence model [11]. In the comparison of the circumferential static pressure coefficients, Plane C shows the largest discrepancy between model and experimental results because the computed separated region occurs later than the measured values as previously indicated on the axial plot [11]. It was concluded that the computational model did not convect as much low momentum fluid from the boundary layer into the center of the duct as the experimental flow was measured to convect [11].

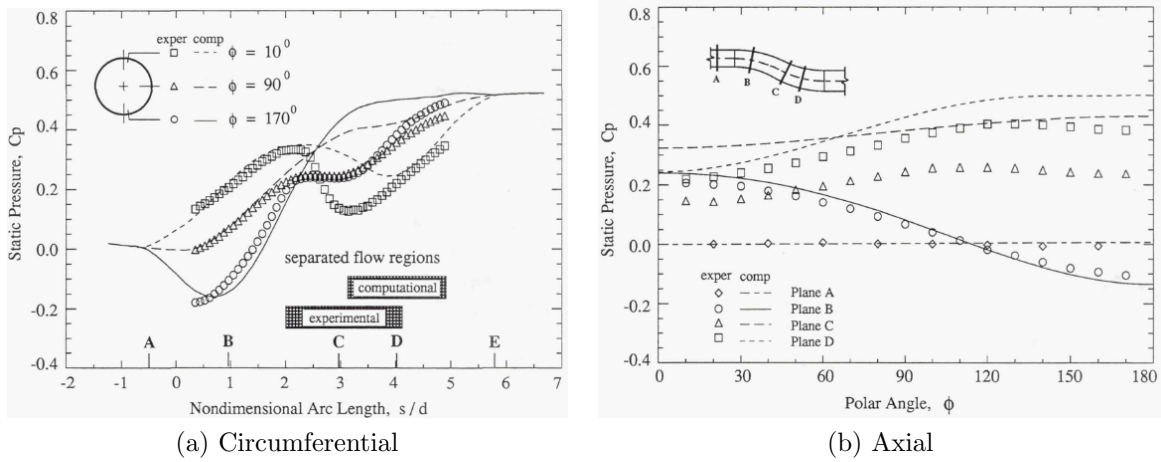


Figure 2.26: Experimental and computational comparison of pressure coefficient (Figure from Wellborn *et al.* [11])

While modeling was first conducted by Wellborn *et al.* following their experiments, the largest modeling effort was conducted following the ONERA experiments, which included a wide variety of CFD codes, turbulence models, approaches, and grids completed by 10 participants at the first AIAA Propulsion Aerodynamics Workshop in July 2012 [2]. From the 10 participants, Figure 2.3 displays the 63 different solutions were generated for the study [2].

Although there are many differences between the results, all the turbulence models used were all RANS models, thus suffering from the limitations listed in Section

Table 2.3: Summary of solutions presented for the baseline flow condition on the scaled Wellborn S-duct (Figure from Delot and Scharnhorst [2])

Solution Number	Solver	Grid			Turb Model*
		Character	Description	Density	
1	Falcon 4	Struct	Coarse	4,031,352	k-kl
2	Falcon 4	Struct	Coarse	4,031,352	ASM
3	Falcon 4	Struct	Medium	8,015,184	k-kl
4	Falcon 4	Struct	Medium	8,015,184	ASM
5	Falcon 4	Struct	Fine	15,942,834	k-kl
6	Falcon 4	Struct	Fine	15,942,834	ASM
7	Falcon 4	Struct	XCoarse	2,030,927	k-kl
8	Falcon 4	Struct	XCoarse	2,030,927	ASM
9	Falcon 4	Unstruct	Coarse	5,728,555	k-kl
10	Falcon 4	Unstruct	Coarse	5,728,555	ASM
11	Falcon 4	Unstruct	Fine	15,226,222	k-kl
12	Falcon 4	Unstruct	Fine	15,226,222	ASM
13	CFD++	Struct	Coarse	4,031,352	Goldberg Rt (1eq)
14	CFD++	Struct	Coarse	4,031,352	k-c
15	CFD++	Struct	Medium	8,015,184	Goldberg Rt (1eq)
16	CFD++	Struct	Medium	8,015,184	k-c
17	CFD++	Struct	Fine	15,942,834	Goldberg Rt (1eq)
18	CFD++	Struct	Fine	15,942,834	k-c
19	CFD++	Unstruct	XCoarse	2,030,927	Goldberg Rt (1eq)
20	CFD++	Unstruct	XCoarse	2,030,927	k-c
21	CFD++	Unstruct	Coarse	5,728,555	Goldberg Rt (1eq)
22	CFD++	Unstruct	Coarse	5,825,555	k-c
23	CFD++	Unstruct	Fine	15,226,222	Goldberg Rt (1eq)
24	CFD++	Unstruct	Fine	15,226,222	k-c
25	OVERFLOW	Struct	Medium	11,000,000	SST
26	WIND-US	Struct	Coarse	2,391,933	k-c
27	WIND-US	Struct	Coarse	2,391,933	SA
28	WIND-US	Struct	Coarse	2,391,933	SST
29	WIND-US	Struct	Medium	7,729,996	k-c
30	WIND-US	Struct	Medium	7,729,996	SA
31	WIND-US	Struct	Medium	7,729,996	SST
32	CFD++	Struct	Medium	10,700,000	SST
33	CFD++	Unstruct	Fine	31,300,000	SST

Solution Number	Solver	Grid			Turb Model*
		Character	Description	Density	
34	FLUENT	Struct	Medium	8,000,000	k-ε
35	FLUENT	Struct	Medium	8,000,000	SST
36	FLUENT	Unstruct	Medium	8,000,000	k-c
37	FLUENT	Unstruct	Medium	8,000,000	SST
38	CFD++	Unstruct	Medium	7,360,000	SA
39	CFL3D	Struct	Medium	7,550,000	SA
40	BCFD	Struct	Fine	23,644,966	BL
41	BCFD	Struct	XCoarse	65,520	SST
42	BCFD	Struct	Coarse	395,845	SST
43	BCFD	Struct	Medium	3,024,952	SST
44	BCFD	Struct	Fine	23,644,966	SST
45	STAR CCM+	Unstruct	Medium	8,430,000	SST
46	Tensai	Struct	Medium	7,793,809	k-ω
47	BCFD	Unstruct	XCoarse	666,273	SA
48	BCFD	Unstruct	XCoarse	666,273	SST
49	BCFD	Unstruct	Coarse	2,828,830	SA
50	BCFD	Unstruct	Coarse	2,828,830	SST
51	BCFD	Unstruct	Medium	12,478,211	SA
52	BCFD	Unstruct	Medium	12,478,211	SST
53	BCFD	Unstruct	Fine	60,679,030	SA
54	BCFD	Unstruct	Fine	60,679,030	SST
55	elsA	Struct	Medium	7,808,214	SA
56	elsA	Struct	Fine	13,177,503	SA
57	elsA	Struct	Fine	13,177,503	K-ε
58	elsA	Struct	Fine	13,177,503	k-kl EARSM
59	elsA	Struct	Fine	13,177,503	SA
60	FLUENT	Struct	Medium	8,000,000	RSM
61	FLUENT	Struct	Fine	19,000,000	RSM
62	FLUENT	Unstruct	Medium	8,000,000	RSM
63	FLUENT	Unstruct	Medium	8,000,000	SA

2.4.3. Because of these limitations, the solutions from Figure 2.3 vary widely as shown in Figure 2.27. Out of the results, none of them matched the pressure recovery and the flow distortion parameters, and furthermore, the location of the flow separation varied among the different solutions [2].

For the structured grids assessed, the results were plotted next to the experimental results for the pressure recovery in Figure 2.28. Delot and Scarnhorst noted “it appears that most codes and turbulence models can either do well in terms of matching total pressure recovery or distortion but generally not both simultaneously” [2]. A Spalart-Almaras turbulence model using CFL3D was the one exception and was the only combination for structured grids to fall within a 95% interval for all four parameters at the AIP [2]. Figure 2.29 shows that while CFL3D with SA performed well at the AIP, it poorly predicted the axial static pressure along and around the

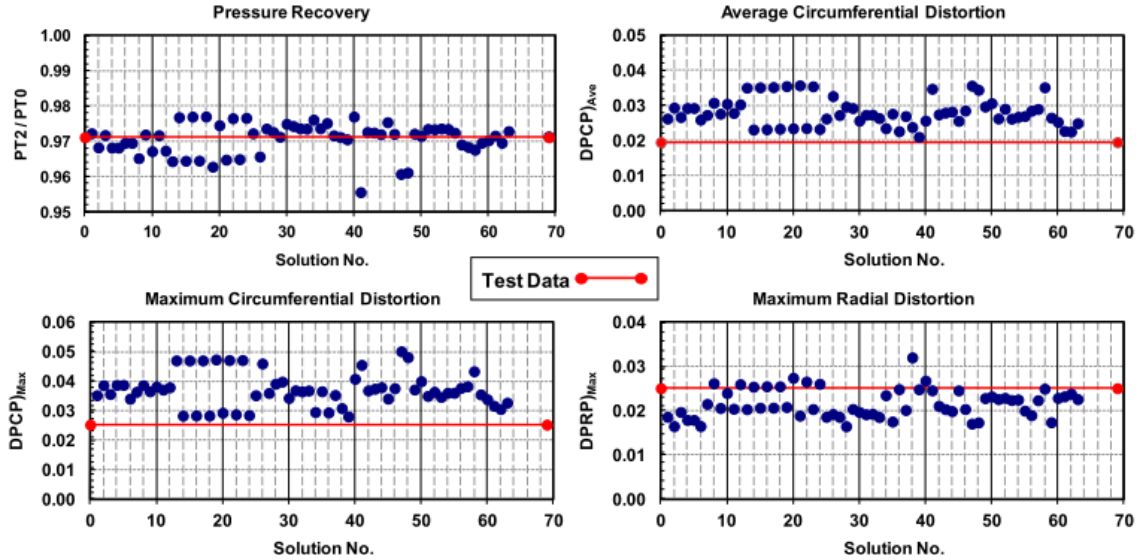


Figure 2.27: Comparison of pressure recovery and flow distortion solutions presented for the baseline flow condition on the scaled Wellborn S-duct (Figure from Delot and Scharnhorst [2])

S-duct [2]. OVERFLOW with a SST turbulence model most closely matched the axial static pressure ports, but poorly predicted the AIP results [2].

A side study was completed by ONERA to assess the affect of a symmetry plane on the solution to determine if a full geometry was needed as an attempt to reduce computational cost [2]. The results from the study showed that the total pressure recovery is not affected by the plane with a variation of 0.1%, but the distortion values were affected with variations for both the maximum and average radial and circumferential distortion of 3% and 7% respectively [2]. This is a result of the counter-rotating flows that develop in the separated region not stable oscillation between the two spiral nodes from Figure 2.6 in the development in the “owl face of the first kind”.

Both studies focused on a Wellborn S-duct that is of similar design to the S-duct in this study. Further testing and modeling has been conducted using flow control devices to reduce the flow distortion in the ONERA test setup, but it is not the focus of this study [32]. While some meaningful comparisons were made with the solutions provided, it lacked a structured approach, such as using the same code and grid with

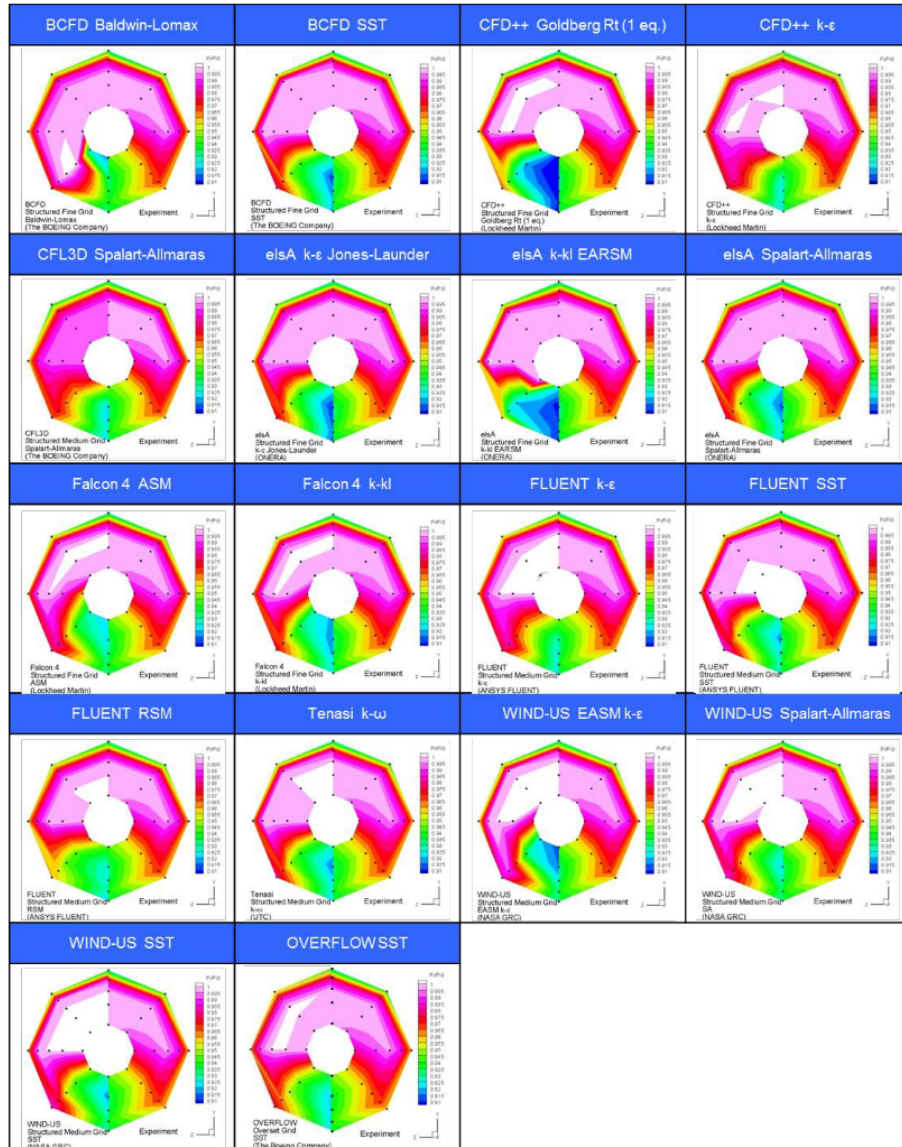


Figure 2.28: Comparison of pressure recovery at the AIP (Figure from Delot and Scharnhorst [2])

RANS, URANS, DES, and LES to produce statistically-meaningful results, that could have led to stronger conclusions [2].

Like the study compiled by Delot and Scarnhorst in the Onera experiment, another large effort study conducted by many groups was compiled by Winkler and Davis in conjunction with the 3rd Propulsion Aerodynamics Workshop [3]. For the group study, the geometry was changed to include a single turn S-duct that had a

D-shaped throat shown in Figure 2.30, rather than purely circular ducts previously studied. The throat for this geometry matches the throat studied in this thesis, but with a double S-duct. The test data was collected at Georgia Tech Transonic Tunnel with a 0.127 meter diameter 40 probe AIP used to assess the static pressure recovery and flow distortion following the inlet [3]. The test included setting the mass flow plug at the end of the extension to obtain the correct flow rate of 2.5 kilograms per second where the total pressure was 99,250 Pascals and total temperature of 294 Kelvin to produce a AIP Mach number of 0.63 [3]. Grids were provided with different grid densities consisting of structured grid without AIP modeled and unstructured grids both with and without the AIP modeled [3]. To ensure consistent results, the full time histories of the 40 AIP probes were requested to be assessed using a single internal Boeing code that meets ARP 1420B [19] requirements for flow distortion characterization [3].

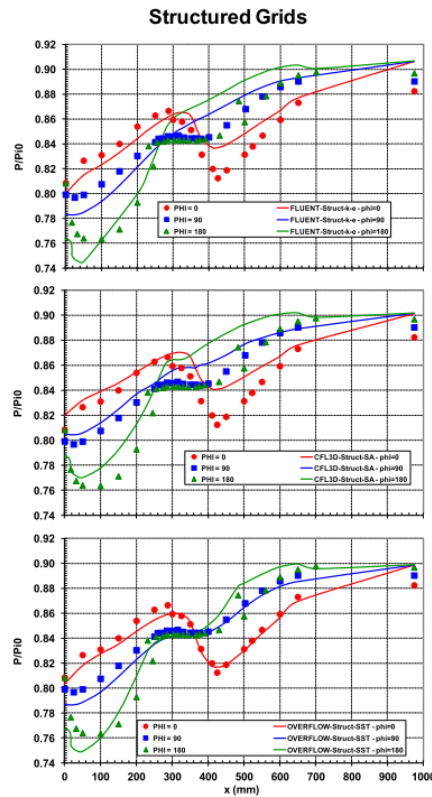


Figure 2.29: Comparison of surface pressure in the S-duct (Figure from Delot and Scharnhorst [2])

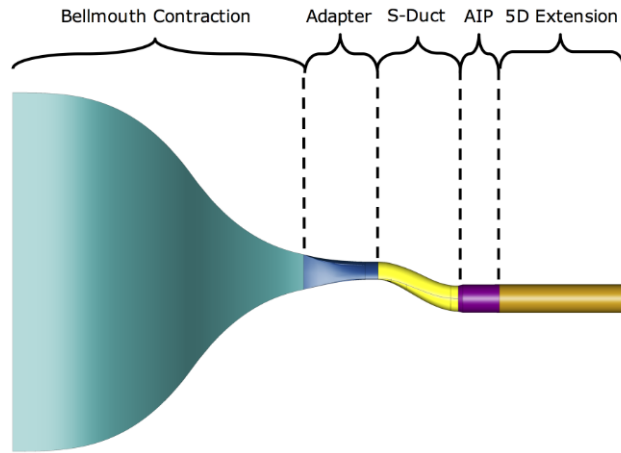


Figure 2.30: Single S-duct with a D-shaped throat used in the 3rd Propulsion Aerodynamics Workshop (Figure modified from Winkler and Davis [3])

In the results, Winkler and Davis noted that in grids without the AIP modeled, the solution consistently under-predicted the total pressure recovery compared to when the AIP was modeled leading to the conclusion that the obstruction caused by the AIP is required to accurately predict the flow [3]. By not modeling the AIP, the flow on the upper surface that separates following the second turn never reattaches as shown in the Mach and total pressure recovery contours from NASA Langley's FUN3D in Figures 2.31 and 2.32 [3]. Additionally, like the results compiled by Delot and Scarnhorst, the results of the total pressure recovery at the AIP for grids without the AIP modeled showed a wide range of solutions, with STAR-CCM+ with a $k - \epsilon$ turbulence model being highlighted for its agreement with the test case [3].

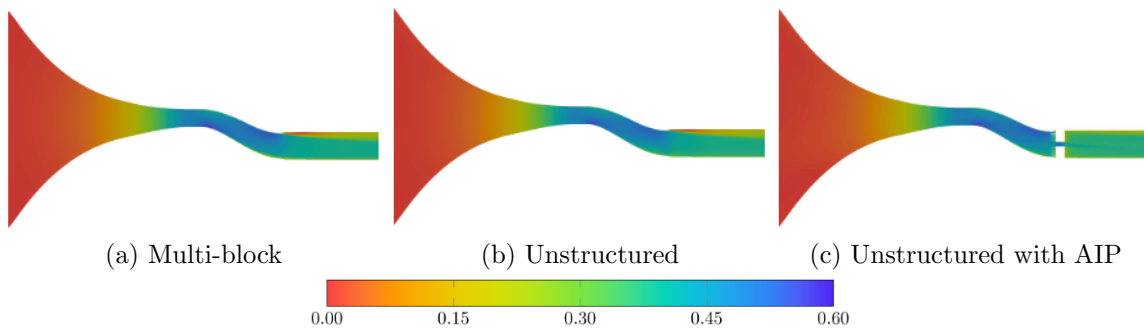


Figure 2.31: Single S-duct with a D-shaped Mach contours for different grids (Figure from Winkler and Davis [3])

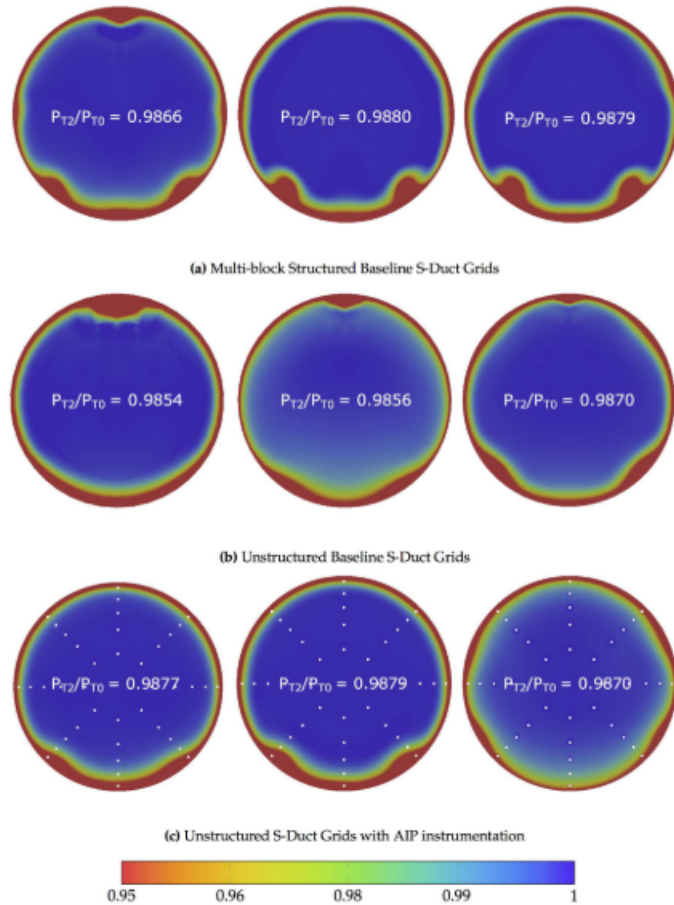


Figure 2.32: Single S-duct with a D-shaped throat pressure recovery for different grids (Figure from Winkler and Davis [3])

Solutions of the S-duct with the AIP modeled were predominantly unstructured due to the complexity of the geometry, but an overset grid and Cartesian approach were provided [3]. BCFD and OVERFLOW were noted to have solutions closer to test data than other codes [3]. Additionally, as these approaches were completed on unstructured grids, it was concluded that no preference is evident for structured or unstructured methods [3]. While true for the study, 2 structured grid solutions out of 29 solutions does not form a strong argument, fueling the desire for a truly structured grid to be generated and run within this thesis.

The first study conducted on the double diffusing S-duct with a D-shaped throat was conducted by Lakebrink and Mani [4]. In the study, the identical geometry to

the one used in this thesis, Figure 1.1, was used. The study consisted of testing at Gerogia Tech Transonic Tunnel and modeling efforts conducted using BCFD with RANS, DDES, and IDDES turbulence models [4]. Like the study compiled by Winkler and Davis, a 40 probe AIP was used with the same post processing software adhering to SAE standard ARP 1420B [19]. For time accurate solutions (DDES and IDDES) a global timestep of 4 microseconds was used to match the sampling rate of the Kulite pressure sensors in the AIP. While three mass flows were evaluated to obtain different flow conditions, the 2.36 kilograms per second provided the most stressing environment, which matches the flow rate used in this thesis. Other flow parameters include a total pressure of 98,870.8 Pascals and a total temperature of 292.2 Kelvin [4]. The flow includes a shock developing in the throat as well as first-turn and second-turn separation as shown in Figure 2.33 [4]. Like previous studies, windows were used on the walls to collect PIV measurements and oil flow visualizations were collected in regions of separation. The test data was collected at 12 mass flows including and between 1.81 kg/s and 2.49 kg/s [4]. Throughout this range, the total pressure recovery averaged across the 40 AIP planes decreased through increasing mass flow rate, which correlated with increasing circumferential distortion [4].

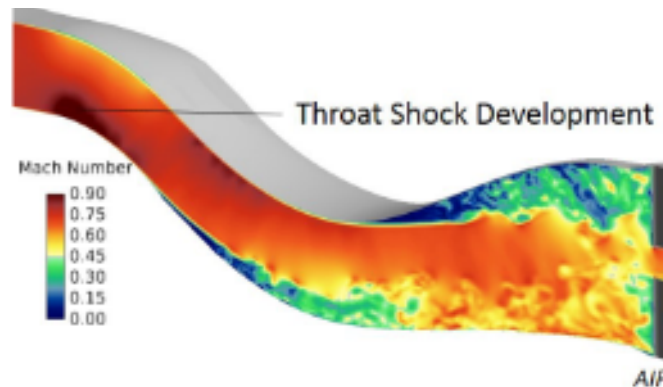


Figure 2.33: Instantaneous Mach countour of the diffusing double S-duct with a flow rate of 2.40 kg/s (Figure from Lakebrink and Mani [4])

The time averaged solution of the shear stresses on the wall were used to provide skin-friction lines comparable to experimental oil flow data. Figure 2.34 compares the DDES model within BCFD to test data [4]. The skin-friction lines on both the upper

and lower separation locations showed close qualitative agreement to the oil flow visualizations from the experiment [4].

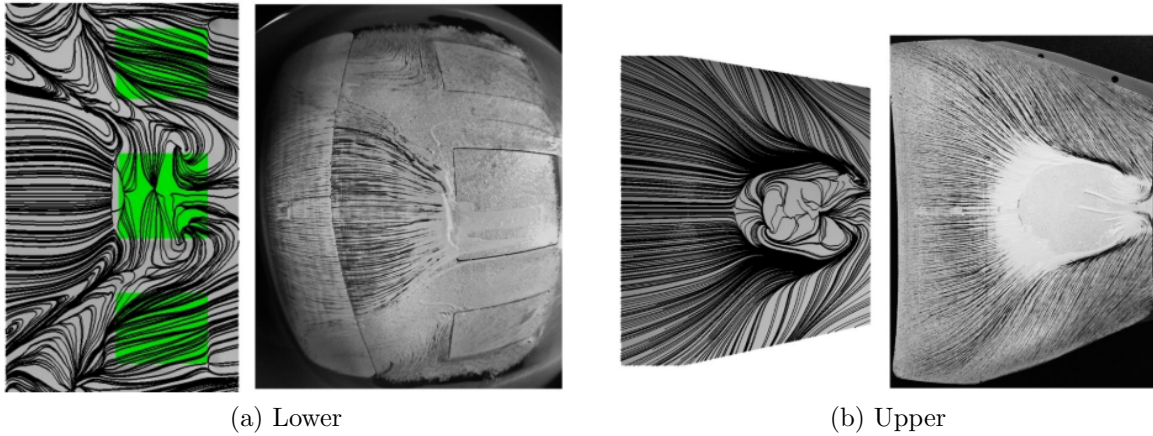


Figure 2.34: Flow separations of DDES skin-friction lines compared to the experimental oil flow (Figure from Lakebrink and Mani [4])

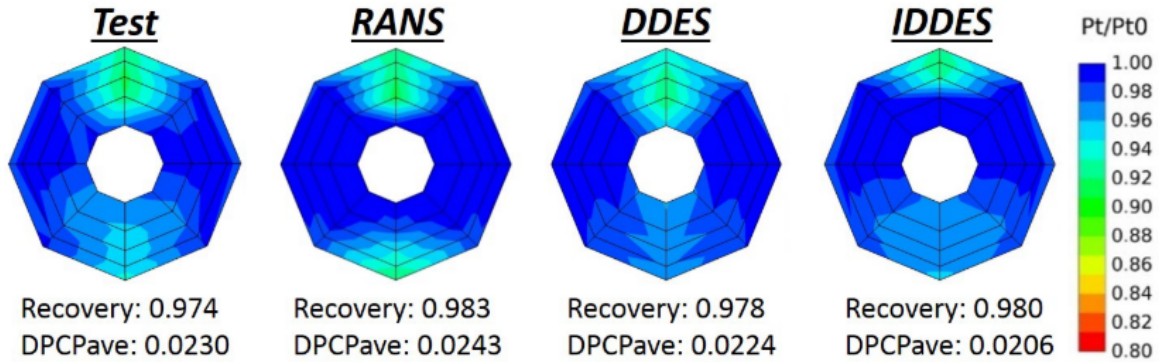


Figure 2.35: Comparison of different turbulence models and test data of the AIP (Figure from Lakebrink and Mani [4])

IDDES solutions were then obtained by Lakebrink and Mani to then be compared against the RANS and DDES solutions as well as the test data for a flow rate of 2.0 kg/s [4]. The AIP comparison in Figure 2.35 shows that DDES performed the best at predicting the test data out of the three models [4]. The IDDES solution obtained greater pressure recovery on the upper surface, deviating from test data, but it did compute the shape of the lower surface the best [4]. The overprediction of the pressure recovery results in an underprediction of the distortion [4]. Both the

DDES and IDDES lack the intensity of the total pressure loss in the lower portion of the AIP as compared to the test data [4].

Further comparisons by Lakebrink and Mani included assessing the turbulent intensity along the centerline plane between DDES and IDDES as shown in Figure 2.36 [4]. The loss of the white band along the upper and lower surface indicating the high-viscosity region in IDDES compared to DDES was noted [4]. Little to no separation was noted following the second bend as a result of IDDES failing to regenerate the near-wall turbulence viscosity after the first window on the lower surface [4]. This has the further ramification in the plot of the oil flow visualizations in Figure 2.37 of IDDES failing to produce the separated flow as the model resorts to DDES without resolved turbulent content and relaminarizes the flow in the first bend of the second turn [4].

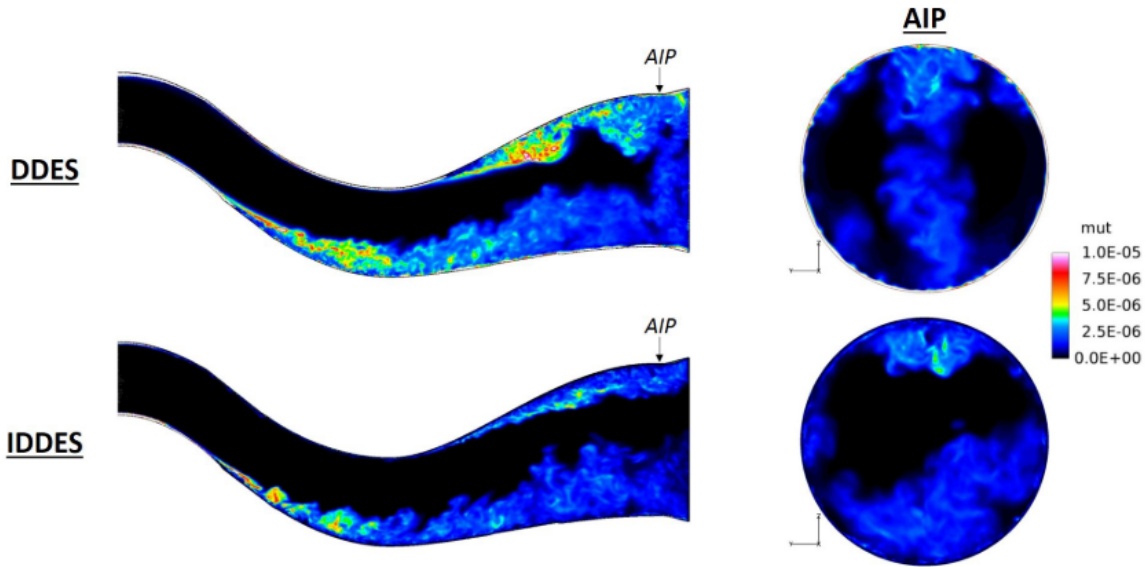


Figure 2.36: Instantaneous turbulent viscosity solutions of DDES and IDDES along the centerline and AIP (Figure from Lakebrink and Mani [4])

The focus of this study is to provide stronger conclusions in modeling diffusing S-ducts. Structured grids, higher order numerical methods and the use of DDES and WM-LES will be used in order to compare solutions obtained in this study to the previously presented solutions.

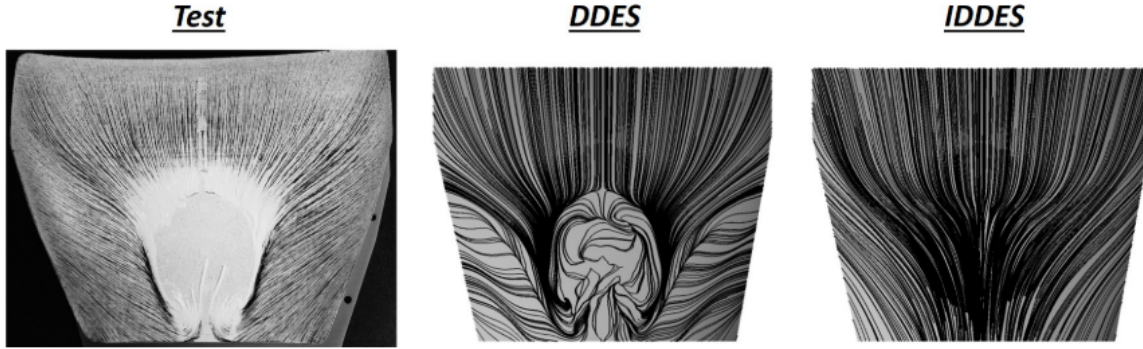


Figure 2.37: Upper flow separation differences between DDES and IDDES skin-friction solutions when compared to experimental oil flow visualization (Figure from Lakebrink and Mani [4])

2.8 Chapter Summary

This chapter focused on areas relevant to understanding the methods and research conducted in this study. Section 2.2 contained a brief overview of viscous flow physics and how it relates to boundary layer formation, turbulence development, and separated flow. The viscosity driven problem in a diffusing serpentine inlet develops important flow features that affect the total pressure recovery and flow distortion after the inlet that is critical for engine and aircraft designers, as discussed in Section 2.3. Section 2.4 presented RANS turbulence models that are obtained by Reynolds or Favre averaging, and while they could be, and have been, applied to S-duct geometry, their limitations imply that RANS should not be used in this application. RANS models was followed by LES modeling in Section 2.5, that outlined the development of a SGS model to model small eddies while resolving the larger energy containing eddies with the grid in order to produce more accurate solutions. Three different LES types were discussed, but the primary focus is on WM-LES. Testing on S-ducts has primarily been conducted on simple representative single S-ducts as outlined in Section 2.6 in order to provide the baseline data for the modeling presented in Section 2.7. The current efforts of modeling methods are insufficient to be a reliable method of predicting accurate separation location, pressure recovery, and flow distortion on a simple S-duct, let alone any given S-duct geometry. Even through the large sample

of 63 test runs consolidated by ONERA, the variety between software, turbulence models, and grids prevented strong conclusions from being obtained. As a result, this study is focused on applying a structured approach to obtain solutions for different turbulence models with the same software and grid in order to have definitive conclusions and community guidance to advance the difficult problem of modeling S-ducts.

III. Methodology

3.1 Introduction

The computational model is derived in Section 3.2 that is used to calculate the solution of the fully structured grids developed in Section 3.3. Section 3.4 specifies the runs required to complete the objectives by obtaining solutions that can be compared to draw strong conclusions about the different turbulence models used. The data collected from the unsteady turbulent solutions includes full time histories of the AIP probes and averaged surface pressure and shear stress, as outlined in Section 3.5. The ability to draw conclusions from the data stems from the ability to process the large amounts of data obtained by CFD to be processed into meaningful comparisons. Section 3.6 details the post processing methods and comparisons made between the solutions and the test data. This also includes determining when the solution has reached a converged state. Lastly, the methodology of ensuring the solution is independent of the grid is covered in Section 3.7. While ensuring grid independence must be done prior to collecting the solutions identified in the test matrix, the same figures of merit will be used, thus using the same data collection and post processing methods. The methods detailed throughout this chapter allow for a systematic approach of assessing the use a WM-LES on a diffusing serpentine inlet with a structured grid and its comparison to DDES and test data.

3.2 Computational Model

US3D, a parallel implicit unstructured hypersonics research CFD code developed by the University of Minnesota, was used for all simulations. Within US3D, inviscid fluxes are calculated using 2nd, 4th, and 6th order kinetic-energy consistent schemes by Subbareddy and Candler [33] with a flux limiter by Ducros [34]. Temporal integration was completed using both a 1st and 2nd order scheme. The 1st order scheme is an implicit Euler time integration with line relaxation. A implicit Crank-Nicolson time integration with point relaxation was used for the 2nd order scheme. The use of the 6th order spatial flux and 2nd order temporal integration schemes was

the most desired combination as it reduces the overall error within the simulation. The decreased error, specifically decreased truncation error, results from modeling higher order terms that were omitted in lower order schemes. The mathematical model is based on the compressible Navier-Stokes equations and is the framework for LES simulations.

3.2.1 Navier-Stokes. With flow conditions primarily expected within the subsonic regime and local pockets of sonic flow, a single species model of a perfect gas can be used for the compressible Navier-Stokes equations written in divergence form as:

$$\frac{\partial U}{\partial t} + \frac{\partial F_1}{\partial x_1} + \frac{\partial F_2}{\partial x_2} + \frac{\partial F_3}{\partial x_3} = 0 \quad (3.1)$$

where the vector of conserved variables, U , and the flux vectors, F_j , are defined as:

$$U = \begin{pmatrix} \rho \\ \rho u_1 \\ \rho u_2 \\ \rho u_3 \\ E \end{pmatrix}, \quad F = \begin{pmatrix} \rho u_j \\ \rho u_1 u_j + p \delta_{1j} - \sigma_{1j} \\ \rho u_2 u_j + p \delta_{2j} - \sigma_{2j} \\ \rho u_3 u_j + p \delta_{3j} - \sigma_{3j} \\ (E + p) u_j - \sigma_{kj} u_k - q_j \end{pmatrix} \quad (3.2)$$

with density ρ , velocity component u_i , static pressure p , and energy per unit mass E which is given by:

$$\rho E = \rho \left(c_v T + \frac{1}{2} u_i u_i \right) \quad (3.3)$$

which provides an expression relating pressure to energy. Within the energy equation, the viscous stress tensor, σ_{ij} , and the heat flux vector, q_j , are:

$$\sigma_{ij} = 2\hat{\mu} S_{ij} + \lambda \frac{\partial u_k}{\partial x_k} \delta_{ij} \quad (3.4)$$

$$q_j = \hat{\kappa} \frac{\partial T}{\partial x_j} \quad (3.5)$$

where T denotes temperature. The viscous stress tensor is defined with the rate of strain tensor, S_{ij} , a symmetric tensor as:

$$S_{ij} = \frac{1}{2} \left(\frac{\partial u_i}{\partial x_j} + \frac{\partial u_j}{\partial x_i} \right) \quad (3.6)$$

The application of Stokes hypothesis defines the bulk viscosity, λ , as:

$$\lambda = -\frac{2}{3}\mu \quad (3.7)$$

The effective viscosity, $\hat{\mu}$, and thermal conductivity, $\hat{\kappa}$, are obtained by the Boussinesq approximation that each have a molecular and turbulent component:

$$\hat{\mu} = \mu + \mu_t, \quad \hat{\kappa} = \kappa + \kappa_t \quad (3.8)$$

For a perfect gas, the following equation of state can be used with the Navier-Stokes equations:

$$p = \rho RT \quad (3.9)$$

in which R is the gas constant.

3.2.2 LES. The filtered set of Navier-Stokes equations for the LES model within US3D were obtained through both spatial filtering and Favre averaging as outlined in Section 2.5. The particular set of SGS and wall model in US3D were implemented and developed by Komives [8].

3.2.2.1 Vreman SGS Model. As discussed in Section 2.5.2, the Vreman model provides a less dissipative model than the Smagorinsky model with results comparable to that of the dynamic Smagorinsky model without the increased computational cost. The model included within US3D by Komives matches that of the

original development by Vreman as:

$$\nu_T = c \sqrt{\frac{B_\beta}{\alpha_{ij}\alpha_{ij}}} \quad (3.10)$$

where,

$$\alpha_{ij} = \partial_i \bar{u}_j = \frac{\partial \bar{u}_j}{\partial x_i} \quad (3.11)$$

$$\beta_{ij} = \Delta_m^2 \alpha_{mi} \alpha_{mj} \quad (3.12)$$

$$B_\beta = \beta_{11}\beta_{22} - \beta_{12}^2 + \beta_{11}\beta_{33} - \beta_{13}^2 + \beta_{22}\beta_{33} - \beta_{23}^2 \quad (3.13)$$

The expansion of the constant Vreman model into a dynamic Vreman model was completed as a secondary objective. The derivation, incorporation, and validation of the model are included in Chapter V.

3.2.2.2 WM-LES. The wall model implemented by Komives uses a reduced set of the Navier-Stokes equations obtained through several assumptions to account for compressibility, inertial effects, and heat transfer within the modeled region off the wall. The first assumption allows the decoupling of the conservation of the wall-normal momentum and conservation of mass equations from the full Navier-Stokes equation sets by allowing the pressure in the wall-normal direction to be a constant. Equations 3.1 and 3.2 with respect to a wall based coordinate frame become:

$$\frac{\partial Q}{\partial t} + \frac{1}{\rho} \left[\frac{\partial G_1}{\partial x_1} + \frac{\partial G_2}{\partial x_2} \right] = 0 \quad (3.14)$$

where the solution vector with density decoupled, Q , and the reduced set of equations flux vector, G_j , are:

$$Q = \begin{pmatrix} u_1 \\ u_2 \\ e \end{pmatrix}, \quad G_j = \begin{pmatrix} -\sigma_{1j} \\ -\sigma_{2j} \\ -\sigma_{kj}u_k - q_j \end{pmatrix} \quad (3.15)$$

in which e is the specific energy [8]. Additionally, the convective and pressure gradients can be omitted in an equilibrium wall-model, such as this one. Equations 3.14 and 3.15 are then solved using a strategy by Bond and Blottner in which the flow primitive variables and density field are updated in an outer loop which the remaining governing equations are solved in an inner loop in a decoupled fashion [35]. Further, the equations can be discretized on a node-based mesh in the near wall region that is embedded within the LES grid as shown in Figure 3.1. With the embedded mesh, the innermost node lies on the wall and the outermost node is the location of the wall-model probe located in a cell several above the wall as suggested by Kawai and Larsson as presented in Section 2.5.3 [22].

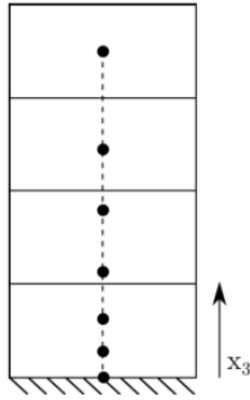


Figure 3.1: Embedded wall-model mesh overlaid on the LES cells with a probe location in the 4th cell (Figure from Komives [8])

3.3 Grid Generation

The generation of a fully structured grid with grid independent results was critical to the outcome of this thesis by allowing for higher order methods to be considered in order to produce more accurate solutions. Link3D, a structured grid design software developed by GoHypersonic Incorporated [36], was the primary grid design tool used to define the grid topology for the provided geometry shown in Figure 1.1. The provided geometry consisted of half of the symmetric S-duct, and thus Link3D was used to generate a grid for half of the S-duct. The extension downstream

of the AIP section was not grided within Link3D, and its inclusion will be detailed later. The most complicated region of the geometry, the AIP section with rakes, was used as the starting point to build the grid, as it would define the remainder of the grid in the core flow. The grid began with two-dimensional surface topology applied to the rakes of the AIP and developed into a three-dimensional topology through the AIP section as shown in Figure 3.2. Once the AIP section was completed, the topology from the AIP was extruding through the S-duct and D-shaped throat to the bell mouth as shown in Figure 3.3. Subsequently the topology for the duct and bell regions was completed in the same fashion. After the topology was defined through the S-duct, it was smoothed using the parallel smoothing processor within Link3D to equally distribute and stretch the cells to obtain the highest orthogonality of the structured grid possible [36].

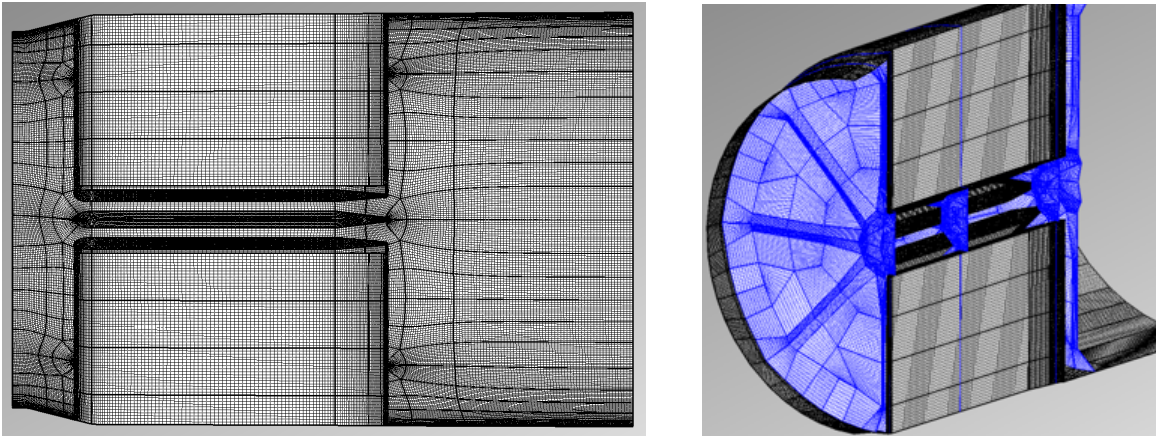


Figure 3.2: Surface and block topology of the AIP section

Following the export of the smoothed half grid from Link3D, Pointwise was used to complete the full grid. First, the outflow extrusion was generated from the back of the AIP section. The outflow extrusion was 0.79 meters long and meshed with a growth rate of 30% and an initial spacing equal to the spacing the the last cell in the AIP section. This was done in order to provide a large dissipation region to damp out and prevent flow effects from the outflow boundary affection the solution upstream. The grid was then mirrored in Pointwise to generate a full grid. Boundary conditions

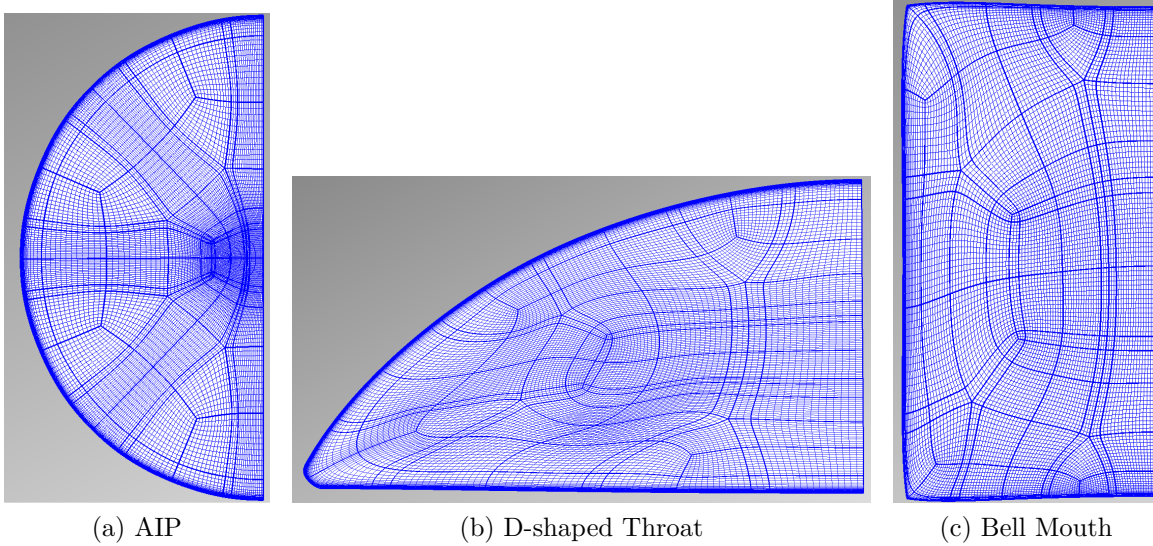


Figure 3.3: Structured grid slices throughout the geometry.

and volume conditions needed to be applied within Pointwise in order to export a case file. A solver of ANSYS was selected with a fluid volume condition applied to all cells. The boundary conditions were walls for the S-duct and rakes, velocity inlet for the bell inlet, and outlet for the outflow of the extension. While these conditions were applied in Pointwise, they can be overwritten within US3D in order to more closely match test conditions with the boundaries included in US3D. Following the exportation of the grid case file from Pointwise, the file was run through US3D's preprocessing routine to generate a grid file and a connector file in HDF5 format that would be used for the simulations.

For the model, boundary conditions were assigned based of the functionality of the test setup within US3D. A no-slip adiabatic wall condition was applied to the exterior of the duct and the rakes protruding into the flow. The initial temperature for the walls was set to 292.2 K to match the test conditions from Lakebrink and Mani [4]. With a subsonic flow, the inlet and outlet were set to subsonic inflow and subsonic outflow respectively. These boundary conditions within US3D allow for the specification of the pressure at each opening, which allows for a similar condition to

the test setup. The pressures of 98870.8 Pa and 82737.1 Pa were used for the inlet and outlet.

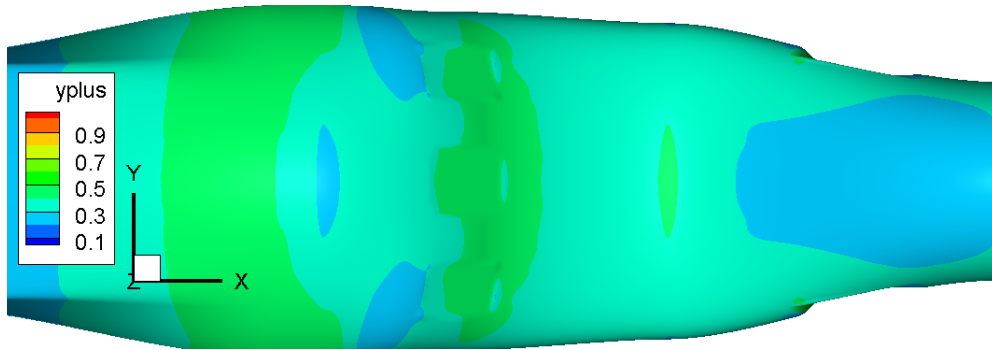
Lastly, wall cell clustering was added within Link3D in order to resolve the boundary layer in the DDES simulations. WM-LES grids did not have the wall clustering added because the use of a wall model specifically prevents that requirement. Furthermore, LES operates best when using perfect isotropic cubes as cells, but in this case a ratio of around 2:1:1 was achieved for length:width:height for most of the S-duct. One reason for the aspect ratio achieved is that with Link3D, the cells blew out into the bell mouth, and attempts made to contain them within the S-duct created folds within the grid while smoothing. Using the achieved ratio prevented doubling the overall cell count in order to obtain more cubic cells. The additional cells are added to the first block touching the surface with a specified initial spacing and growth rate to achieve the desired wall spacing, typically $y^+ = 1$. The complex geometry with varying boundary layer thicknesses and properties prevented the initial height of y^+ to be the same throughout the geometry. With the S-duct being the section of primary investigation, a $y^+ = 1$ at any location within the S-duct was used as the requirement to ensure the boundary layer was adequately resolved.

An initial grid was made with an approximation of the initial grid spacing, Δs , based on the approximate flow expected using Equations 2.1 to 2.5. The growth rate of 10% was applied as it is a common choice for wall clustering. The initial grid generated with these values was run using a RANS turbulence model. The use of a RANS model was to quickly reach a steady state solution. Equations 2.3 and 2.5 were combined and rearranged with Δs replacing y as:

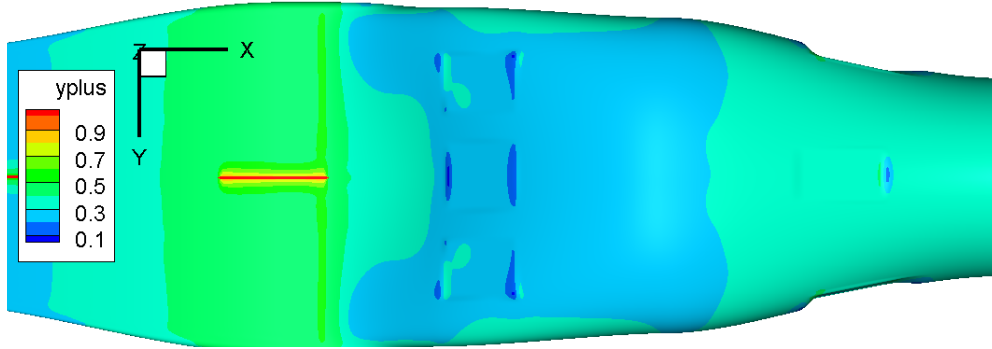
$$\Delta s = \frac{y^+ \nu}{\sqrt{\frac{\tau_w}{\rho}}} \quad (3.16)$$

where $y^+ = 1$ and the values of ν , τ_w , and ρ were extracted from the solution of the initial run. By assessing this equation at the maximum value of shear stress found on the surface of the S-duct an initial spacing was determined. An initial

$\Delta s = 3.597$ micrometers was identified from this method to meet the requirement for $y^+ \leq 1$ within the S-duct. The growth rate was kept at 10%. Using these values, the majority of the S-duct had a y^+ of much less than one as shown in Figure 3.4. The red line of high y^+ along the midplane of the lower surface that occurs just before the throat is an artifact of the grid folding over itself. This fold within the grid was corrected before subsequent runs, but it did not change the y^+ achieved on the surface throughout the rest of the S-duct.



(a) Upper



(b) Lower

Figure 3.4: y^+ obtained on the surface of the S-duct.

Figure 3.5 shows a sample of the clustering applied in Link3D. For the medium grid, the clustered grid obtained an average value for the S-duct of $y^+ \approx 0.5$. In comparison, the unclustered grid had an average $y^+ \approx 90$ for the S-duct. It is important to note that cells outside of the wall clustering are identical for both grids,

which starts with the seventh cell in the unclustered grid. The increase in y^+ in the unclustered grid cut the number of cells within the entire grid in half from 102,005,964 to 53,496,880.

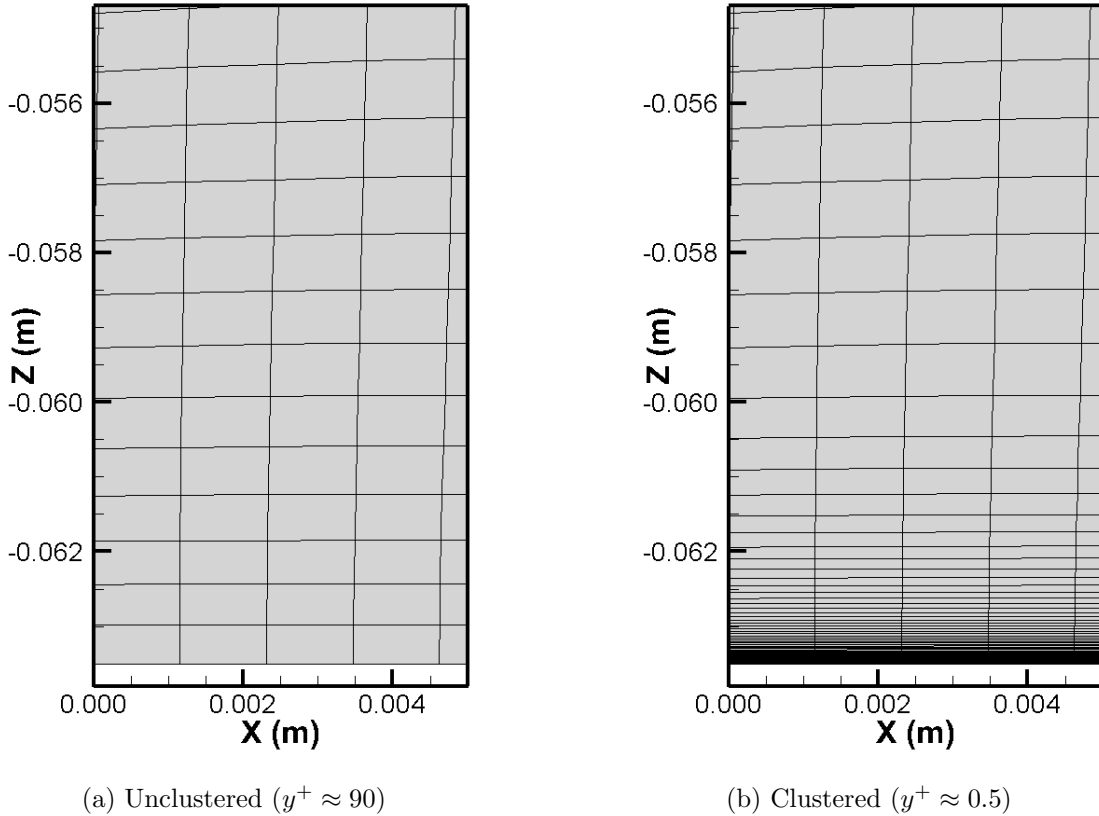


Figure 3.5: Comparison of the smoothed medium density grids at the AIP

One of the main limitations of the wall model incorporated by Komives is the inability to have the wall model overlap from two different surfaces. In the S-duct geometry used, this occurs at the perpendicular intersection between the S-duct and the rake. To avoid the overlap, when the wall model was used, it was only applied to the S-duct as this was the primary area of investigation. With the wall model run on a grid without any wall clustering, this required the rakes to not have clustering or a wall model applied. While computing a poorly WR-LES on the rakes is not desired, it was necessary for the model to run. The error introduced by this approach was

determined to be minimal as the main purpose of the rakes was to provide a blockage necessary to achieving the correct mass flow rate. Even though the flow was subsonic and changes of the solution downstream of the S-duct would affect the solution, the poor resolution of the boundary layer on the rake would have little impact.

3.4 Test Matrix

The test matrix was developed to follow a methodical approach to answering the primary objective by only changing one variable at a time as presented in Table 3.1. A baseline, Case 1, was achieved by running the existing unstructured grid with a 2nd order DDES turbulence model in US3D to identify differences between US3D and BCFD previously used by Lakebrink and Mani [4]. The generated structured grid for the geometry with grid independent results provided the basis for all grids. The procedure for proving grid independence is discussed in Section 3.7 with the results presented in Section 4.2. In the case of DDES and IDDES, clustered cells resolve the boundary layer appropriately with a $y^+ \leq 1$ while the clustering is removed for WM-LES. From Case 1 to Case 2, the only variable changed is the grid type from unstructured to structured allowing for conclusions to be drawn about the impact of the grid used. By using a structured grid, it allowed for the use of higher order flux schemes as in Case 3 that increases to a 6th order flux scheme. Case 3 can be compared to Case 2 to observe the differences in the solution resulting from the order of the flux scheme. Cases 3 through 5 all use 6th order flux schemes with differing turbulence models in order for trends between the models to be identified.

Table 3.1: Planned Test Matrix of Structured Approach

Case	Grid Type	Turbulence Model	Spatial Accuracy
1	Unstructured	DDES	2nd
2	Structured (w/ clustering)	DDES	2nd
3	Structured (w/ clustering)	DDES	6th
4	Structured (w/ clustering)	IDDES	6th
5	Structured	WM-LES	6th

Table 3.2: Planned Test Matrix of Wall Model Probe Sensitivity Study

Case	Grid Type	Turbulence Model	Spatial Accuracy	Probe Cell Location
5a	Structured	WM-LES	6th	3
5b	Structured	WM-LES	6th	5

Case 5 can further be broken down for the wall-model probe location sensitivity study in which the probe location off of the wall is varied displayed in Table 3.2. This additional sensitivity study would be used for a secondary objective to provide better guidance regarding how far off the wall the wall-model probe should be placed.

The planned test matrix was not completed as planned for several reasons. First, the simulation of an unstructured 2nd order DDES was not completed within US3D. This simulation was intended to be a direct baseline comparison of BCFD to US3D. Since the mixed grid used in BCFD was only for half of the geometry, it needed to be mirrored to generate a full grid as required because the flow is not truly symmetric as noted by Wellborn *et al.*, and using only half the duct produces a different result [1]. There were no grid generation tools available to handle the file format of the mixed grid, so generation of the full mirrored mixed grid was not possible for this study. Also, due to limited computational resources, the structured grid 2nd order DDES simulation was not conducted. The comparison of Boeing’s 2nd order DDES on a mixed grid could still be made to the 6th order structured grid DDES results from US3D.

Second, while attempting to run the grids through a 6th order DDES turbulence model, instabilities were identified for the structured grid generated using a 6th order flux scheme. This was expected as it is common for 6th order methods to develop instabilities with cells that do not have perpendicular edges, and to fit the complex geometry the stretching prevents fully perpendicular edges. The flux scheme was subsequently reduced 4th order which proved stable on the structured grid.

Third, an IDDES solution was not conducted. Due to the results presented by Lakebrink and Mani [4] outlined in Chapter II, it was determined the shortcomings

of the model, caused from the interaction of the LES and RANS models within IDDES, would not be overcome by using a higher order flux scheme and a fully structured grid.

The achieved test matrix is presented in Table 3.3. Both DDES cases were conducted on three grids each in support of the grid independence study further detailed in Section 3.7.

Table 3.3: Completed Test Matrix of Structured Approach

Case	Grid Type	Turbulence Model	Temporal	Spatial
1	Structured (w/ clustering)	DDES	1st	4th
2	Structured (w/ clustering)	DDES	2nd	4th
3	Structured	WM-LES	2nd	4th

While, the WM-LES case was intended to be further subdivided to assess the effects of the probe location on the solution, due to a lack of computational resources and schedule slip, this was not conducted. The height of the wall-model probe used was in the third cell off the wall as identified in Case 5a. This follows the recommendations of Kawai and Larsson as noted in Section 2.5.3 [22]. Completing the probe height sensitivity study is recommended for follow on research.

3.5 Data Collection

The turbulent statistics of the unsteady solution were collected using a combination of methods to best identify and characterize the flow separation within the S-duct and the AIP properties of total pressure recovery and flow distortion. All statistics were collected following a period of initialization for the selected case parameters to allow for transients to wash out of the solution. While a freestream velocity does not truly exist within the S-duct, the velocity on the centerline passing through the middle of the S-duct was averaged to obtain a mean freestream velocity. This mean velocity was then used to assess the time required for two flow times, defined as two times the duration it takes a particle to travel completely through the S-duct from

throat to AIP. The time required for two flow times was used as the initialization period to wash out the transients.

All statistics were collected for the clustered grids using a timestep of 2.0×10^{-7} seconds, as it was determined to be the largest stable step size that could be run with the three grids. While common to complete a timestep sensitivity study to ensure that the solution does not change with changing the timestep, it was not conducted in this study for a few reasons. First, the timestep is over an order of magnitude smaller than the one Boeing used which indicates it is sufficiently small to resolve the frequencies obtained by Boeing. Second, the number of additional cases required to be completed to achieve the timestep independence study was not obtainable through a lack of allocated computational time.

The unclustered grids were also run using a timestep of 2.0×10^{-7} seconds for two main reasons. First, it was a timestep that was determined to be stable for the models and methods applied. Second, while a slightly faster timestep may have been stable, it was determined that the DDES and WM-LES comparison and frequency analysis would benefit from using the same timestep.

3.5.1 S-duct Surface Data. Statistics on the surface of the S-duct are obtained using build in routines within US3D. The routines time average the solution from one iteration to the next as well as calculating the standard deviation [37]. The time averaged solution contains pressure, temperature, heat flux, and shear stress components [37]. For the S-duct, the pressure and shear stress components were the variables of primary concern used to produce the coefficient of pressure plots and oil flow visualizations. The mean and standard deviation for the variables are then post processed within US3D in order for TecPlot to view the solution.

3.5.2 AIP Probe Data. The specific locations for the 40 AIP probes are listed by Winkler and Mani [3]. While the probe locations provided in Winkler and Mani were for a single turn S-duct, they used the same AIP for both tests and thus

the values were shifted up to be centered within the current geometry. The alignment of the 40 AIP probes are presented in Figure 3.6 with the view point of looking from the rakes back into the S-duct. The probe numbers in Figure 3.6 correspond to the positions listed in Table 3.5.

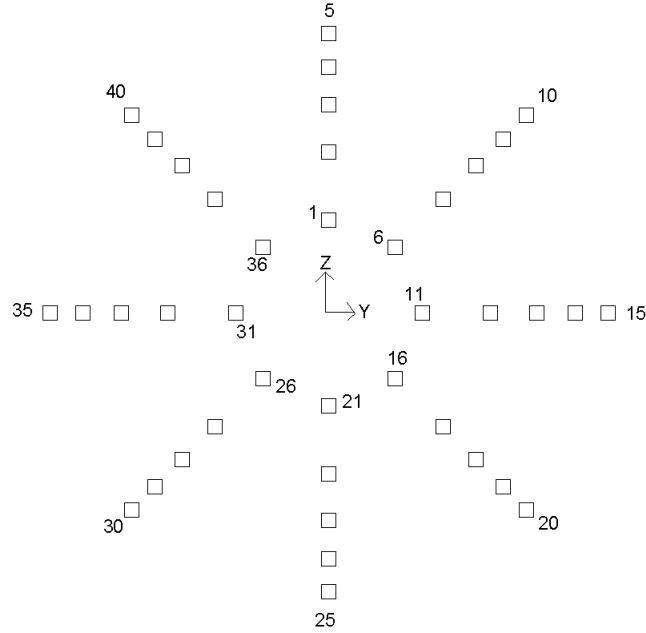


Figure 3.6: Probe layout of the AIP probes.

Table 3.4: Deviations of probe location achieved from AIP probe locations in millimeters.

	Max x	Max y	Max z	Avg x	Avg y	Avg z
Coarse	0.817	0.594	0.593	0.474	0.259	0.231
Medium	0.649	0.264	0.385	0.308	0.118	0.156
Fine	0.508	0.349	0.294	0.268	0.159	0.123
WM-LES Medium	0.649	0.264	0.385	0.308	0.120	0.153

Table 3.5: Probe locations of the AIP probes and the cell centers of the cells which the probe locations occur for the medium grid.

Probe Number	Rake Leg	Ring	Requested Locations (m)			Achieved Locations (m)		
			x	y	z	x	y	z
1	1	1	3.18E-03	0.00E+00	2.01E-02	3.73E-03	2.16E-04	2.00E-02
2	1	2	3.18E-03	0.00E+00	3.48E-02	3.66E-03	2.44E-04	3.50E-02
3	1	3	3.18E-03	0.00E+00	4.49E-02	2.76E-03	-2.27E-04	4.47E-02
4	1	4	3.18E-03	0.00E+00	5.31E-02	3.39E-03	-2.38E-04	5.28E-02
5	1	5	3.18E-03	0.00E+00	6.02E-02	2.82E-03	-2.64E-04	6.01E-02
6	2	1	3.18E-03	1.42E-02	1.42E-02	2.87E-03	1.43E-02	1.39E-02
7	2	2	3.18E-03	2.46E-02	2.46E-02	3.09E-03	2.46E-02	2.48E-02
8	2	3	3.18E-03	3.18E-02	3.17E-02	3.55E-03	3.16E-02	3.17E-02
9	2	4	3.18E-03	3.76E-02	3.76E-02	2.94E-03	3.76E-02	3.77E-02
10	2	5	3.18E-03	4.26E-02	4.26E-02	3.82E-03	4.26E-02	4.25E-02
11	3	1	3.18E-03	2.01E-02	-1.27E-06	3.55E-03	2.00E-02	-9.93E-05
12	3	2	3.18E-03	3.48E-02	-1.27E-06	3.20E-03	3.48E-02	1.87E-04
13	3	3	3.18E-03	4.49E-02	-1.27E-06	2.53E-03	4.49E-02	1.07E-04
14	3	4	3.18E-03	5.31E-02	-1.27E-06	3.36E-03	5.34E-02	8.29E-05
15	3	5	3.18E-03	6.02E-02	-1.27E-06	3.10E-03	6.03E-02	7.56E-05
16	4	1	3.18E-03	1.42E-02	-1.42E-02	2.54E-03	1.44E-02	-1.42E-02
17	4	2	3.18E-03	2.46E-02	-2.46E-02	3.58E-03	2.46E-02	-2.44E-02
18	4	3	3.18E-03	3.18E-02	-3.18E-02	3.19E-03	3.18E-02	-3.21E-02
19	4	4	3.18E-03	3.76E-02	-3.76E-02	3.00E-03	3.76E-02	-3.74E-02
20	4	5	3.18E-03	4.26E-02	-4.26E-02	2.85E-03	4.25E-02	-4.28E-02
21	5	1	3.18E-03	0.00E+00	-2.01E-02	3.77E-03	2.05E-04	-2.03E-02
22	5	2	3.18E-03	0.00E+00	-3.48E-02	3.50E-03	2.52E-04	-3.47E-02
23	5	3	3.18E-03	0.00E+00	-4.49E-02	3.23E-03	2.25E-04	-4.51E-02
24	5	4	3.18E-03	0.00E+00	-5.31E-02	3.09E-03	2.34E-04	-5.34E-02
25	5	5	3.18E-03	0.00E+00	-6.02E-02	2.94E-03	-2.56E-04	-6.02E-02
26	6	1	3.18E-03	-1.42E-02	-1.42E-02	2.54E-03	-1.44E-02	-1.42E-02
27	6	2	3.18E-03	-2.46E-02	-2.46E-02	3.58E-03	-2.46E-02	-2.44E-02
28	6	3	3.18E-03	-3.18E-02	-3.18E-02	3.19E-03	-3.18E-02	-3.21E-02
29	6	4	3.18E-03	-3.76E-02	-3.76E-02	3.00E-03	-3.76E-02	-3.74E-02
30	6	5	3.18E-03	-4.26E-02	-4.26E-02	2.85E-03	-4.25E-02	-4.28E-02
31	7	1	3.18E-03	-2.01E-02	-1.27E-06	3.55E-03	-2.00E-02	-9.93E-05
32	7	2	3.18E-03	-3.48E-02	-1.27E-06	3.20E-03	-3.48E-02	1.87E-04
33	7	3	3.18E-03	-4.49E-02	-1.27E-06	2.53E-03	-4.49E-02	1.07E-04
34	7	4	3.18E-03	-5.31E-02	-1.27E-06	3.36E-03	-5.34E-02	8.29E-05
35	7	5	3.18E-03	-6.02E-02	-1.27E-06	3.10E-03	-6.03E-02	7.56E-05
36	8	1	3.18E-03	-1.42E-02	1.42E-02	2.87E-03	-1.43E-02	1.39E-02
37	8	2	3.18E-03	-2.46E-02	2.46E-02	3.09E-03	-2.46E-02	2.48E-02
38	8	3	3.18E-03	-3.18E-02	3.17E-02	3.55E-03	-3.16E-02	3.17E-02
39	8	4	3.18E-03	-3.76E-02	3.76E-02	2.94E-03	-3.76E-02	3.77E-02
40	8	5	3.18E-03	-4.26E-02	4.26E-02	3.82E-03	-4.26E-02	4.25E-02

The full time histories of the 40 AIP probes were obtained using a user routine added to US3D. The user routine consists of two parts, a find element step and a print element step. The first step consists of finding the cells (elements) in which specified coordinates occur. It returns the cell number as well as the coordinates of the center of the cell. Following this procedure for the medium density grid, Table 3.5 was generated showing the requested locations corresponding to the locations of the AIP probes and the location achieved corresponding to the cell center of the cell which the requested point exists.

Assessing the values in Table 3.5, the maximum deviation from the requested location was obtained per probe for each of the three directions. Further the average deviation could be calculated. The results for the medium grid are presented in Table 3.4 along with the coarse and fine grids that were assessed in the same fashion. The small magnitude of the deviations from the AIP probe locations to the ones of the cell centers show that cells selected to represent the AIP probes are reasonable. Further, the WM-LES Medium grid closely aligned with the Medium grid. Since the two grids only differed with the wall clustering, all cell locations for probes should be the same with the exception of the outer ring, so alignment was expected for the two grids.

The second step includes collecting the full time history of the probe. For this step, a similar user routine added to US3D writes out the solution for each of the cells identified from the first step for each solution. In the case of the S-duct where 40 AIP probes were used, the US3D script prints out 40 files, one for each probe, with the full time history of the probe including time, three velocity components, density, temperature, and pressure. These individual files are then post processed assessing total pressure recovery and flow distortion at the AIP, two of the primary figures of merit. Additionally, power spectrum density plots can be generated from the time histories to identify the frequencies within the flow.

3.5.3 Plane Slices. The last type of data collection implemented time and spatially averaged planes. This type of averaging was done to obtain averaged slices

along the centerline of the S-duct and a cross cut at the AIP location. While instantaneous slices could have easily been obtained with US3D, they would not show the time averaged unsteady flow. To obtain these two slices, a user routine was written providing the center value, tolerance value, and number of planes. The number of planes are the number of cells that fall within the window generated by the center value plus and minus the tolerance value. In the case of the AIP location, the center value was $x = 3.18 \times 10^{-3}$ meters corresponding with the AIP location and the tolerance was set to the maximum x deviation listed in Table 3.4, which would result in a value of one for the number of planes as it would encapsulate the thickness of a single cell. A similar procedure was used to define the centerline plane with $y = 0.0$ meters and a tolerance based on the maximum y deviation from Table 3.4 of the rake legs lying on the centerline plane, corresponding to Legs 1 and 5, with the number of planes again being equal to one. While the script is set up to collapse the number of planes into one plane providing a spatial average, with only one plane it just provides the temporal average that then occurs from iteration to iteration. The averaged values for each plane are output in separate files for use in post processing. These time averaged slices of a single cell width are not necessary for any of the objectives or figures of merit of this thesis, but they provide a better representation of the flow than an instantaneous snapshot.

3.6 Post Processing Methods

Following the extraction of the necessary data from the simulation, post processing routines are implemented to obtain results that can be compared to previous studies and test data. The first task is determining that the solution has reached a converged state, prior to further data analysis. The average surface pressure and shear stress can then be assessed to determine the locations of the separation and reattachment in the S-duct. The AIP probe data is processed to extract the total pressure recovery and the flow distortion of the S-duct.

3.6.1 Solution Convergence. Before meaningful results can be extracted from the unsteady solution, a converged solution needs to be obtained. While steady solutions, such as RANS simulations can rely on indicators such as residual as an indicator of a converged solution, it is not necessarily an indicator of a converged solution for unsteady flow. The residual is a measure of the amount of change from one iteration to the next, with a variety of ways it can be calculated. In the case of unsteady simulations, even in a converged solution, the amount of change from eddies passing from one cell to the next is reflected in a large residual value that does not decrease like that of a steady simulation. For this reason, different indicators of convergence are needed. Since this solution is a compressible, unsteady, turbulent problem, the indicators selected should reflect characteristics specific to the problem. For example, a characteristic such as coefficient of pressure, which is independent of a compressible flow, would be a poor indicator of a converged solution, but it is still a valid indicator of flow separation regions. For the S-duct, the two indicators selected were the mass balance and the pressure of the AIP probes.

The mass balance was selected as it is a common convergence indicator that would be applicable to this simulation. Within US3D, the mass balance is provided in the convergence file along with the root mean squared residual. The mass balance is the sum over all cells of the difference between the mass into and out of the cell. If the solution is converged, it would reach a value of zero. For the S-duct, the mass-balance would never reach zero, but rather oscillate around a value near zero, with a fixed frequency of approximately 100 Hz, as shown in Figure 3.7 based on a 50,000 iteration cycle with a fixed timestep of 2×10^{-7} seconds. This was the lowest frequency observed in the solution, but higher frequencies are clearly present. The oscillations were assessed to result from acoustic waves in the solution. The acoustic waves experienced were conducted through the domain because US3D lacks a flow preconditioner that is needed for subsonic flow for this exact reason. Many commercial codes contain a flow preconditioner in order to increase the stability and damp out

the acoustic waves in subsonic flows, but since US3D is designed for supersonic and hypersonic flows, a preconditioner was never included.

In order to appropriately assess the mass balance, a running average of the mass balance was calculated. With enough iterations, the running average mass balance would collapse onto the overall average, indicating convergence of this parameter. The exact number of iterations needed to reach this point was determined by observing the solution and the running average as the solution evolved. The overall average in Figure 3.7 is slightly negative because the unsteady solution lacks the aid of the preconditioner. However, it still reaches a converged solution.

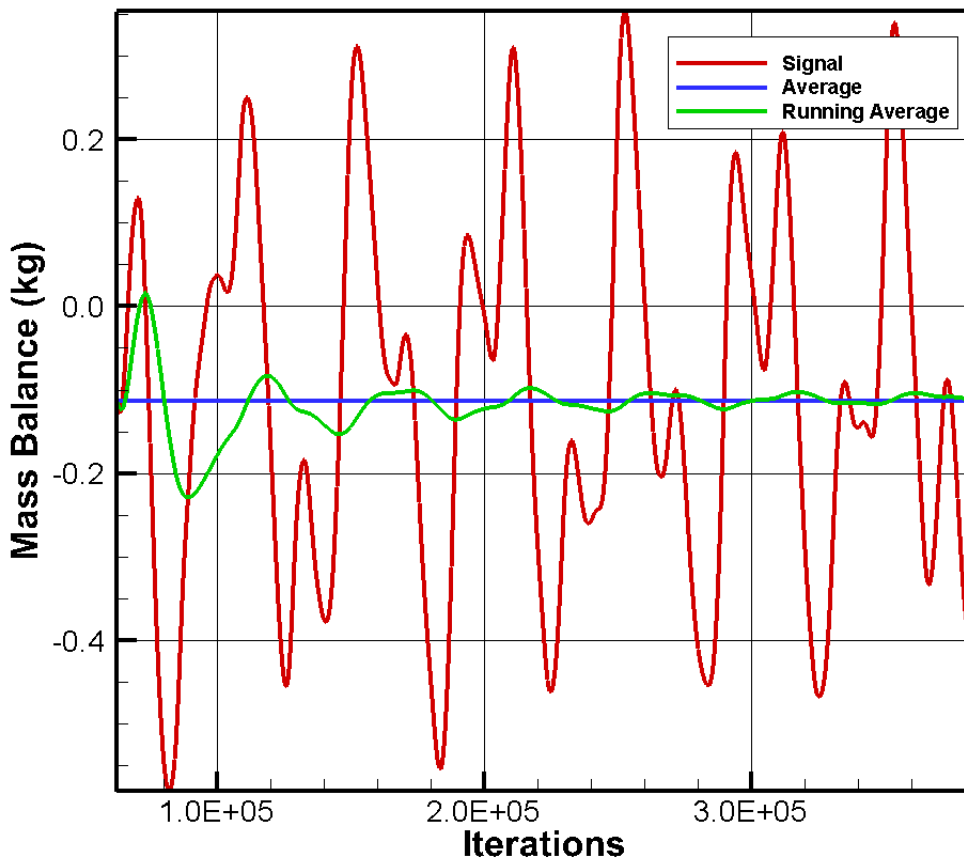


Figure 3.7: Example of the convergence of the running average of the mass balance for the unsteady solution.

The pressure of the AIP probes was also used to assess overall convergence of the solution as shown in Figure 3.8. The time history of the AIP probes show continuous fluctuation as they measure the eddies that roll past it, so the use of a running average, like described for the mass balance, was used for this parameter. The 100 Hz frequency was also noted as the lowest frequency in the pressure time histories. When both the mass balance and the pressure of the probes collapsed onto the mean, the solution was considered converged.

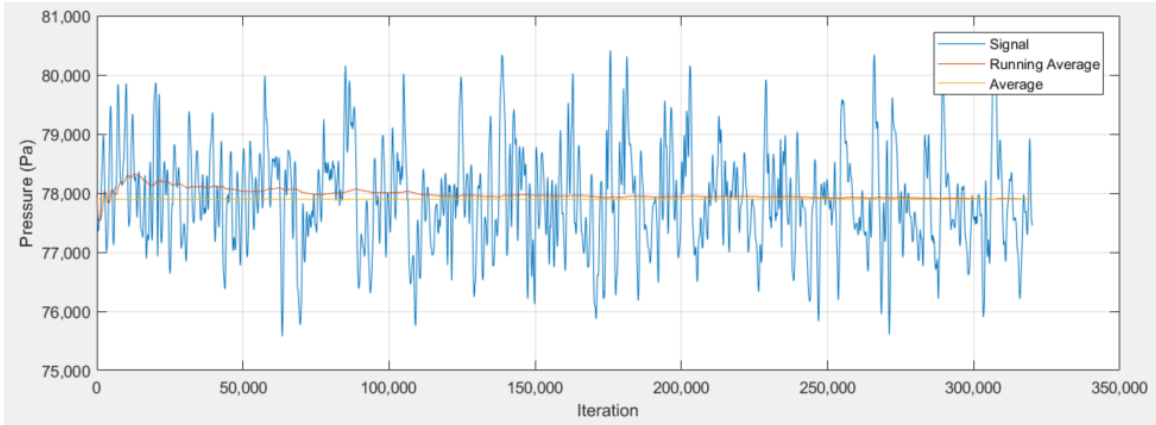


Figure 3.8: Example of the convergence of the running average of the pressure for the unsteady solution.

3.6.2 Mass Flow Rate. The pressures for the simulation determine the mass flow rate of the solution. Therefore, the mass flow rate can be used to compare different grid densities or compare modeled results to test data. US3D includes the routine to extract the mass flow rates directly from the solution at the inflow and outflow faces. During the tests, a mass flow plug, similar to the one shown in Figure 2.13, was adjusted at the outflow location to obtain the desired mass flow rate. The targeted mass flow rate from test data provided by Lakebrink and Mani was 2.22 kg/s [4]. While the inflow and outflow pressures could be altered to obtain a mass flow rate that matched the test conditions, for this study, the pressures were kept constant. One reason the pressures were not adjusted is that Winkler and Davis noted that the mass flow rate was very sensitive to small changes in the geometry such as the inclusion of the PIV windows and AIP rakes [3]. Further, Lakebrink and

Mani present a range of test data points between 2.00 kg/s and 2.40 kg/s [4], so as long as the mass balance falls within that range it can be compared without needing to alter the pressures.

The mass balance, the difference between mass flow into and out of the domain, is computed at every iteration. The mass balance can be used to indicate solution convergence. For a perfectly converged solution, the mass flow rate through the inflow would match the rate through the outflow. As indicated in Section 3.6.1, the solution does not reach a state when the mass flow into and out of the duct are equal. The outflow mass flow was selected as the value to be used in comparisons as the test data reported mass flow rate at the outflow of the duct.

3.6.3 Surface Statistics. The surface data is processed to generate coefficient of pressure plots along the upper and lower centerline of the S-duct and the shear stress on the wall can be assessed like an oil flow visualization. Both of these methods are used to identify the location of flow separation and reattachment.

3.6.3.1 Coefficient of Pressure. The coefficient of pressure was selected as a figure of merit because it can be used to indicate flow features on the surface such as flow separation. To obtain the coefficient of pressure along the S-duct, precise lines along the upper and lower centerlines of the S-duct extracted the time averaged pressure on the surface. The time averaged pressure was previously obtained using the internal US3D statistics as outlined in Section 3.5.1. The coefficient of pressure, C_p , was then calculated for each point along the extracted lines with:

$$C_p = \frac{p_0 - p}{0.5\rho_0 U_0^2} \quad (3.17)$$

using the pressure at the point, p , while freestream values were then used for pressure, p_0 , density, ρ_0 , and velocity magnitude U_0 . The coefficients of pressure calculated can then be plotted for assessment.

In this case, the geometry does not lend itself to easy identification of freestream conditions, so the values were obtained from the center of the D-shaped throat at the beginning of the double S-duct portion of the setup. This location was selected because if this S-duct was installed on an aircraft, the bell and adapter portion of the geometry would not exist, therefore the flow in the middle of the D-shaped throat would be the closest to the freestream values.

3.6.3.2 Oil Flow Visualizations. The other primary means of analyzing the surface statistics is by constructing simulated oil flow visualizations from the shear stress components on the wall. The three shear stress components make up the vector components used when plotting streamlines. These streamlines are the oil flow lines as detailed in Section 2.2.3. Within regions of separation, the oil flow visualization will display the patterns of the owl face of the first kind as discussed in Section 2.2.4 and displayed in Figure 2.6. Further the individual spiral nodes and locations where the oil flow lines turn back upstream allow for the identification of the reversed flow and counter-rotating vortices occurring just above the surface. Additionally, the axial shear stress can be displayed under the simulated oil flow visualizations. In regions that the axial shear stress is negative, the shear stress is in the opposite direction of the flow indicating the presence of reversed flow, which can further aid in the comprehension of the oil flow visualizations.

While the oil flow visualizations can be compared to each other and to test data from a qualitative assessment, quantitatively the location of the flow separation regions can be assessed. The start and end of the flow separated regions are the most important to determining the accuracy of the model to predict the flow observed in the test data. The locations are extracted from along the centerline at the point at which there is a change in sign of the axial shear stress. While the axial shear stress does not account for the whole wall shear stress, the predominant portion of the shear along the surface up to and following a flow separated region is the axial shear stress.

3.6.4 AIP Probes. The full time histories of the 40 AIP probes are used in determining the main frequencies observed in the eddies flowing over the probes in addition to the total pressure recovery and flow distortion at the AIP. The total pressure recovery and flow distortion are of primary concern in this study as correct prediction aids in the design of future S-ducts that would interface with a turbine engine.

3.6.4.1 Pressure Wave Frequency. Frequency analysis of the pressure time histories of the probes identifies the number of iterations needed to capture the main energy containing frequencies observed in the flow. Each of the 40 individual AIP probes stored the full time history within individual files. In order to reduce the amount of redundant effort in processing the data, two Fortran scripts were used. The scripts to process the frequency content came from scripts created by Ross Chaudhry at the University of Minnesota [38]. The first script read in the individual probe files, and processed the frequency content using the “Fastest Fourier Transform in the West” (FFTW). FFTW is a free collection of fast routines that are used to compute Discrete Fourier Transform developed at the Massachusetts Institute of Technology by Frigo and Johnson [39]. While FFTW is written in C, it contains the necessary hooks to be used in Fortran, and it serves as the base of FFT within MatLab [39].

When assessing a new probe history with a provided base frequency, FFTW first looks for a wisdom file from assessing a similar signal with the same base frequency. If the wisdom file does not exist, it completes an assessment of a wide range of different FFT methods that could be applied to determine the best one to use given the data set. While this initial case takes time to find the best method and write the wisdom file, subsequent runs are incredibly quick. The time needed is dependent on the number of samples being assessed within the data set determined by the base frequency provided, with more samples taking more time. Using the observation of 100 Hz from the mass balance in Section 3.6.1, the base frequency was set to be 25 Hz in order to ensure lower frequencies were not observed in the flow. Based on the

timestep used, this would require a minimum of 200,000 iterations, but 100 Hz would be used if enough data points were not obtained. Using a base frequency of 25 Hz would allow for the frequencies integer multiples of the base frequency to be resolved.

Following the completion of the FFTW routines, the power spectrum density is output for the probe in a new file. The second script then uses the output from the FFTW to create an improved data file for Tecplot to allow for quicker processing.

A few modifications were made to the scripts to improve their use for this specific study. First, the scripts were modified to allow for batch processing so that all 40 files would be completed simultaneously. Second, the format of the output files was improved for better compatibility between scripts and visualization tools. Third, while the hook for a Hanning window existed, modifications were needed to complete the inclusion and calculations using a Hanning window, and allow for easy selection without the need to recompile the script.

Once the frequency data has been processed, the power spectrum density (PSD) is plotted on a log scale verse frequency in Tecplot. Figure 3.9 was generated with probes defined in Figure 3.6 using the fine clustered grid with a 4th order spatial flux scheme and 1st order temporal scheme with DDES. Only half of each ring is presented as the flow was assumed to be nearly symmetric to prevent overcrowding the plots. Spikes in the PSD indicate a dominate energy containing frequency in the flow. The outer ring was selected as it was expected to show more features of the turbulent eddies in the flow, whereas the inner ring should show less eddy content and better represent the bulk flow.

Both plots in Figure 3.9 shows a spike at 100 Hz that aligns with the low frequency noted in the mass balance plot. While present, it was not nearly as pre-dominate as other frequencies, specifically at 275 Hz within both plots. The 275 Hz frequency is also noticeable in Figure 3.7, where approximately three waves are within 100 Hz wave. Further, this frequency shows strong harmonics in both plots, but especially within the inner half ring. The harmonics are more apparent in the inner

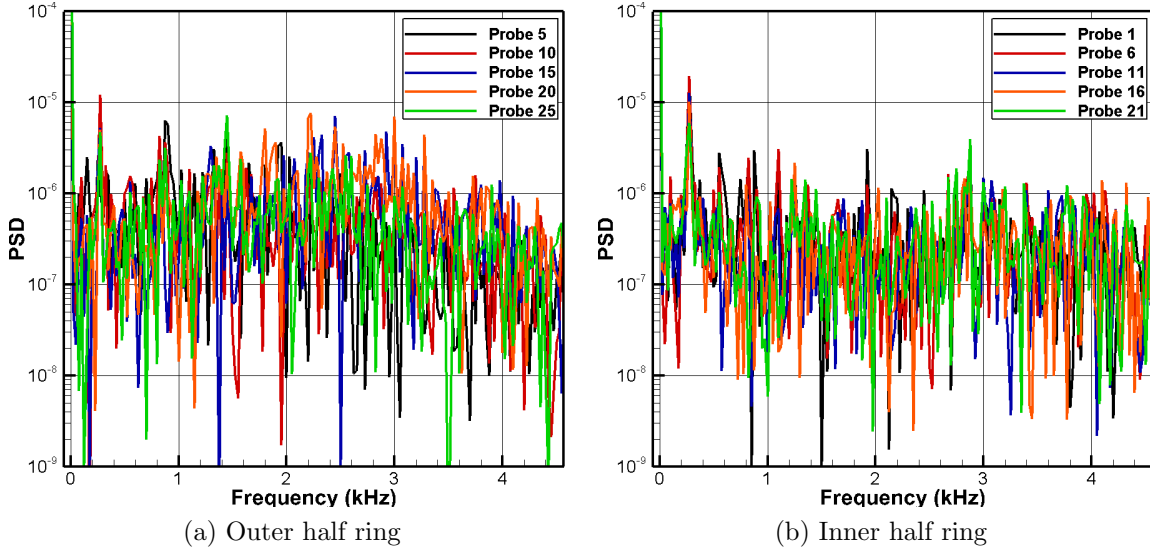


Figure 3.9: PSD of the half of the outer and inner rings of the AIP probes

half ring because there is less turbulent energy and the acoustic waves are stronger with less distortion. It can therefore be deduced that this frequency and harmonics are the acoustic waves in the S-duct resulting from the lack of a preconditioner.

Following the initial spikes and harmonics, the inner half ring remains relative flat across with no strong peaks shared across the frequency spectrum. Conversely, the outer half ring presents more predominant frequencies, especially within the 1.5 kHz to 3.2 kHz range, then the PSD drops linearly indicating the end of the major frequencies present. The difference between the inner and outer ring is largely the amount of turbulent kinetic energy contained in the flow. A larger range of frequency was also visualized but not presented because there were no identifiable features of interest. Therefore, it is concluded that the bulk of the turbulence observed within the S-duct falls within the 1.5 kHz to 3.2 kHz range.

These two conclusions ensure that the correct sampling rate and number of iterations are used to sufficiently capture the frequencies present in the flow. With a fixed timestep of 2×10^{-7} seconds, as determined necessary to be stable, integer multiples of 50,000 iterations are needed for each simulation to capture the 100 Hz without truncation. For the fixed timestep used, the sampling rate is 5000 kHz. When

considering the Nyquist frequency to prevent aliasing, the sampling rate is cut in half. The Nyquist frequency is then 2500 kHz, almost two orders of magnitude larger than what is anticipated in the flow, allowing for sufficient resolution. Further, the test data had a sample rate of 25 kHz resulting in a Nyquist frequency of 12.5 kHz. Based upon the frequency analysis, both the sampling rate of the simulations conducted and the test data was sufficient to resolve the frequencies present in the flow.

3.6.4.2 Total Pressure Recovery. Total pressure recovery is calculated at each AIP probe, which are then combined to create a contour plot of the entire AIP face. The first step is processing the probe data for visualization. To reduce the repetitive nature of this task, a Fortran script was written to calculate the total pressure at each AIP probe. This was accomplished by first finding the time averaged values of density, velocity magnitude, and static pressure from the probe time histories. The values were then combined with:

$$p_t = p_s + p_d = p_s + 0.5\rho U^2 \quad (3.18)$$

using the fact that total pressure is the summation of static and dynamic pressure and the definition of dynamic pressure. The total pressure at each probe was then divided by the maximum total pressure observed by one of the probes to calculate the total pressure recovery. This implies the assumption that at one of the probes on the AIP the total pressure recovery was exactly 1.0, which given results and predicted flow patterns from test data and previous studies such as Lakebrink and Mani [4], this is a reasonable assumption. Further, this assumption was made due to the previously discussed difficulties in defining freestream conditions in the S-duct that would have been used to gauge the total pressure recovery against. The script then continues by reading in the locations of the probes and combining it with the averaged values, total pressure, and total pressure recovery to output in a data file for visualization.

The 40 AIP probes can then be plotted in Tecplot. The output of the Fortran script run on the 40 AIP probes produces an unstructured data set. Tecplot prevents

the use of a color contour on an unstructured data set. To create the contour, a structured grid was overlaid on the unstructured data set of 40 probes and interpolated onto using the inverse-distance interpolation built within Tecplot. The contour plot of the total pressure recovery was then plotted for analysis.

3.6.4.3 Flow Distortion. The flow distortion is obtained using Boeing’s proprietary code that adheres to the standard SAE ARP 1420B [19]. The time history files for the 40 AIP probes were provided to Boeing for processing. The code operates by running the time history for the probes through a low pass filter at the same frequency as the test data, which is 4×10^{-5} seconds or 200 times greater than the timestep used. The code provided values for average circumferential distortion values for each filtered timestep. The circumferential distortion values for each filtered timestep were then averaged over the full range of iterations to obtain the overall average circumferential flow distortion across the AIP. The averaged values are then compared to previous studies and test data.

3.7 Grid Independence

In order to ensure grid independent results, three different grid densities of the structured grid generated were run using DDES with a 4th order flux scheme. While a 6th order flux scheme was planned, initial runs using 6th order indicated instabilities for the grids generated, so the flux scheme was decreased to a 4th order scheme that proved stable. The three different grids are defined in Table 3.6 as coarse, medium, and fine corresponding to an increasing number of cells with the inclusion of clustering.

Table 3.6: Grid densities of clustered grids used for independence study.

Grid	Number of Cells
Coarse	41,475,616
Medium	102,005,964
Fine	148,304,192

The three different grids were compared and assessed in Section 4.2 using the same figures of merit previously discussed that include: both flow distortion and total pressure recovery at the AIP, total pressure mappings of the AIP, and the locations of upper and lower separated regions. The solutions generated from the grids were then compared to each other to determine the point at which increasing the grid density did not significantly impact the solution. Since DDES is a variation of LES, changing the grid density will always change the solution as a result of more energy in the flow being resolved opposed to modeled by the subgrid model. For all solutions, a fixed timestep of 2.0×10^{-7} seconds was used for all iterations.

In addition to assessing the difference in the grid densities, the grid independence study was completed using both a 1st order and 2nd order temporal scheme. First, the 1st order temporal solutions from the three grids were compared to each other in Section 4.2.1 to assess the differences caused by the grid resolution. In a similar fashion the 2nd order solutions using three grid densities were compared to each other in Section 4.2.3. Finally, the solutions from the two different temporal schemes were compared against each other in Section 4.2.4. The analysis conducted allows for a determination in Section 4.2.5 of the grid density required to capture the solution without increased error caused by an unresolved grid.

3.8 Chapter Summary

The methodology detailed in this chapter allows for the collection and assessment of the results presented in Chapter IV. The fully structured grids generated in Section 3.3 completed the first task of the primary objective. With a structured grid, higher order methods defined in Section 3.2 can be applied to the simulations. The grid independence study outlined in Section 3.7 is completed in Section 4.2, and was conducted to determine the grid density needed for the remaining simulations listed in the test matrix from Section 3.4. The results in Chapter IV were obtained following the the data collection methods of Section 3.5 and data reduction tools of Section 3.6. Application of these methods allowed for a systematic approach to assessing the

use of structured grids, higher order methods, WM-LES, and DDES on a diffusing serpentine inlet.

IV. Results and Analysis

4.1 Introduction

The methods defined in Chapter III are used to complete the test matrix and make comparisons between the different modeling configurations and test data. Section 4.2 completes the grid independence studies. The grid and temporal integration scheme identified by the study were used throughout the remaining assessments conducted. Once solutions were obtained on the selected grid, the models were compared to previous test data and previous modeling results in Section 4.3. Prior to comparing the simulations, the mass flow rates obtained were used to identify the closest test data point for reference. Total pressure recovery, center plane instantaneous solutions, oil flow visualizations, and flow distortion were all used as figures of merit to compare the solutions fulfilling the primary objective in Section 1.3. Two additional studies were conducted to further the understanding of the flow and drawbacks of using a 40 probe AIP. These studies are provided in Sections 4.4 and 4.5 that use full average AIP plane solutions and instantaneous images from an AIP video, respectively.

4.2 Grid Independence Results

Solutions for the three different clustered grid densities were obtained using DDES with 4th order fluxes. The grid independence study was conducted using two different time integration schemes. The first grid independence study was conducted using 1st order implicit Euler time integration with line relaxation. The grid independence was repeated using a 2nd order implicit Crank-Nicolson time integration with point relaxation as a means to further obtain a higher order solution to reduce solution dissipation. Lastly, the results from the grid independence study determined the grid to use for further study, the WM-LES grid to use, and for comparison to test data.

4.2.1 First Order Temporal Grid Independence. The first step was confirming the mass flow obtained through the outlet of the three grids aligned with test data.

As specified in Section 3.6.2, the targeted mass flow rate was 2.22 kg/s, but within the range of 2.00 kg/s to 2.40 kg/s was acceptable for comparison to test data. Table 4.1 shows the mass flows achieved for the three grids all using the same boundary and initial conditions. A constant timestep of 2.0×10^{-7} seconds was used for each grid. While the coarse and medium grid densities are close in value, there is a slight decrease in mass flow rate for the fine grid, it accounts for just a 1.4% difference in mass flow. The mass flow rate is not enough to prove grid independence by itself, but if it was, the small percent difference between the medium and fine grid would indicate the use of the fine grid.

Table 4.1: Outflow mass flow for the three grids using a 1st order temporal scheme.

Grid	Mass Flow Out
Coarse	2.17 kg/s
Medium	2.18 kg/s
Fine	2.15 kg/s

Following the assessment of the mass flow, the test solution for the appropriate mass flow could be used to compare to the DDES solutions. Figure 4.1 shows the total pressure recovery across the AIP for the three grid densities using a 1st order temporal scheme. The total pressure recovery was averaged over the full time duration that statistics were obtained. All plots use the same color mapping and range to provide for direct comparison between the plots. The maximum total pressure recovery is 1.0 and noted with the dark blue color. Decreases in the total pressure recovery occur on the upper and lower surface. This loss in total pressure recovery comes from the lower momentum fluid from the boundary layer being entrained into the bulk of the flow through the counter-rotating vortices created with flow separation. As this flow separation occurs following the bends in the duct, the losses in total pressure recovery occur on the upper and lower surface.

The lower surface in Figure 4.1 exhibits two major trends when increasing grid density from coarse to fine. First, the total pressure recovery increases, as denoted by the decreasing green region on the lower surface. Second, the wide distribution of the total pressure loss on the lower surface tightens up and narrows around the midplane of the duct forming more of the heart or bean shaped loss of total pressure recovery. This trend is preferred as it matches the expected profile from previous experiments [4], but this will be further discussed when compared to test data in Section 4.3. The upper surface for the three grid densities are all in close agreement, but the fine grid demonstrates the small blue dips in the sides of the upper total pressure loss region. The increase in total pressure recovery on the sides is good and expected as the flow in that region is largely unaffected by the two sets of counter rotating vortices. These trends within the solution will be further analyzed when compared to test data in Section 4.3.

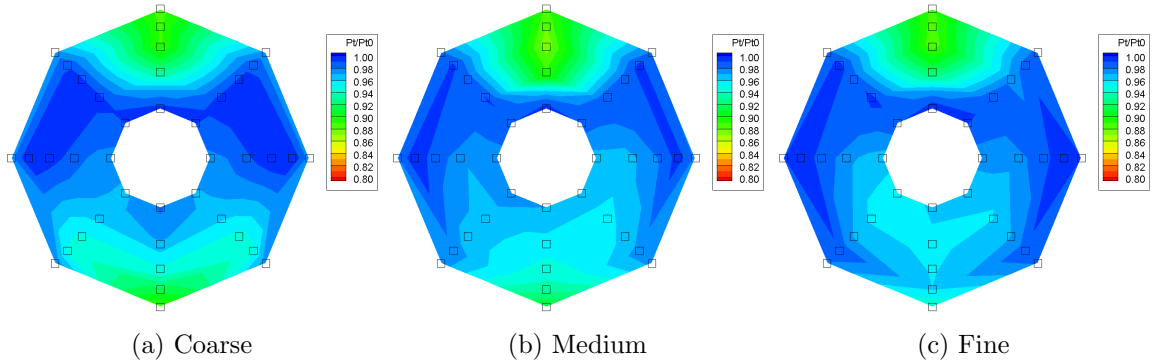


Figure 4.1: Comparison of total pressure recovery at AIP of three different grid densities using 4th order DDES using the full collected time history.

To put the total pressure recovery in a more quantitative value, the total pressure recovery of each of the 40 AIP probes can then be averaged together to obtain the overall total pressure recovery. Table 4.2 presents the total pressure recovery of the AIP in addition to the flow distortion values obtained from the full time histories of the 40 AIP probes. The coarse and medium grid densities are in close agreement with each other, and the fine grid is slightly higher. Between the medium and fine grid a 0.4% difference is observed, which is an increase from 0.0% between the coarse and

medium grid, but as it is still less than 1% it can still be considered valid for a grid independence.

Table 4.2: Grid independence of total pressure recovery and circumferential flow distortion from full time history.

Grid	Total Pressure Recovery	Circumferential Flow Distortion
Coarse	0.9660	0.0320
Medium	0.9652	0.0357
Fine	0.9694	0.0349

The 40 AIP probe time histories were also used to calculate the circumferential flow distortion presented in Table 4.2. The medium and fine grid show close agreement with each other with a 2.2% difference. The fine and medium grid have a larger 10.4% difference. Based on the results of the total pressure recovery and the circumferential flow distortion, the changes between all three grid solutions provide an early indication that the fine grid should be used, but more assessments with other figures of merit are needed.

The different solutions by the three different grid densities can further be assessed by comparing the oil flow visualizations as in Figures 4.2 and 4.3. In the figures, the streamlines show the direction of the flow from the time averaged shear stress components on the surface. The coloring denotes the average shear stress in the axial direction, where blue identifies negative shear stress denoting reversed flow on the surface. Although not compared to the test data at this point, the solutions can be expected to have regions of reversed flow and predominantly symmetric flow on each side of the centerline. The mappings show some of the general flow features expected, but they are poorly resolved and show features not anticipated for a time averaged solution. During the grid independence studies, the solutions are only compared to each other to identify a point when increasing the grid density further does not change the solution, so that the solution is only a result of the numerical methods and models implemented.

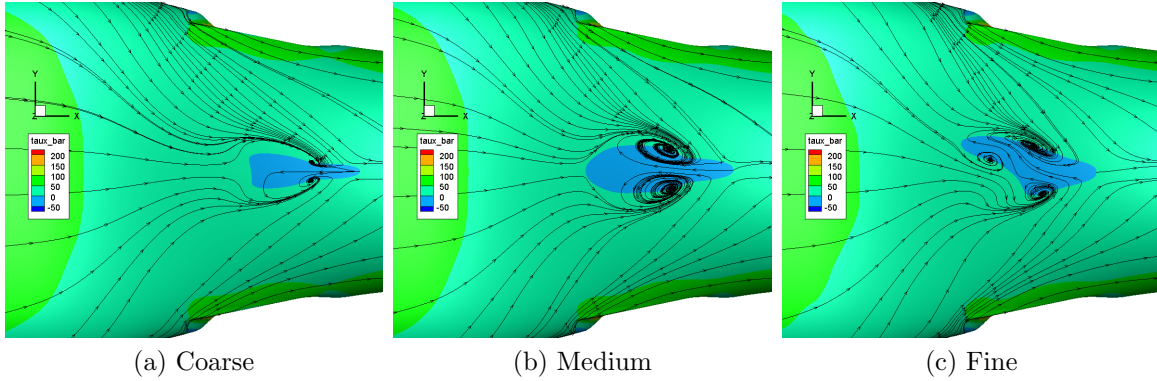


Figure 4.2: Comparison of upper flow separation region of three different grid densities using 4th order DDES.

On the upper surface in Figure 4.2, the medium grid shows the closest resemblance to the expected owl face of the first kind. The coarse grid did not fully show the formation of the spiral vorticies needed to complete the owl face of the first kind. The fine grid had an additional vorticity occurring just prior to the separation region in addition to a skew in the first portion of the separated flow region. All three had reverse flow, as indicated by the blue region on the surface, but the location at which they started differed between the solutions. Further, the shape of the reversed flow differed between the three grid densities, with the medium grid showing the most symmetric pattern.

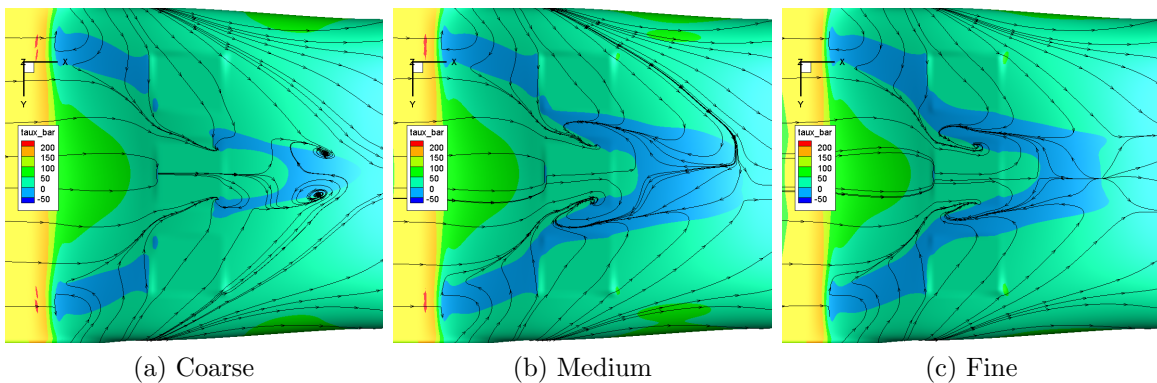


Figure 4.3: Comparison of lower flow separation region of three different grid densities using 4th order DDES.

The lower surfaces presented in Figure 4.3 showed more inconsistencies than the upper surfaces. First, the location of the spiral node on the surface and the subsequent downstream oil flow visualization differs greatly between the three densities. The coarse grid does not have fully developed spiral node vortices occurring within the windows, but it has an extra set of developed spiral nodes that occur further downstream as shown in the oil flow visualization. The medium grid has only one of the two anticipated counter-rotating spiral nodes developed creating nonsymmetric flow downstream. The fine grid also has only one of the two anticipated spiral nodes developed, but it is on the opposite side of the medium grid. Additionally, the oil flow stream lines on the fine grid indicate more symmetric downstream flow than the medium grid. Second, the regions of reversed flow indicated by the presence of negative axial shear stress colored blue differs among the solutions. The coarse grid has separation between the upstream regions and downstream regions that are connected in both the medium and fine grid densities. The overall shape and magnitude of medium and fine grid are in general agreement, and reflect differences that result from the previously noted differences in simulated oil flow visualizations.

Both Figures 4.2 and 4.3 were produced from the averaged full time histories. One potential reason for the discrepancies in the surface time averaged plots is that the time averaged data was initialized before a converged solution was reached. This could account for the surface streamlines that do not appear to fully develop the expected features from prior testing and research, stemming back to Wellborn in 1991. While recollecting the surface statistics was considered, it cannot be accomplished within the current version of US3D. Specifically, once the surface statistics have been initialized, they cannot be turned off or reset. Additionally, since the solution is averaged iteration to iteration, there is only the final solution available at any point in time. In order to collect statistics from a converged solution, the solution from before the statistics were initialized would need to be run out longer to a converged solution prior to initializing the surface statistics. As this would result in a repeat of nearly a million iterations across the three grids plus the iterations needed for collecting the statistics,

it was considered too computationally expensive to conduct the rework for the surface statistics.

An alternate method of collecting more statistics in order to provide a larger number of iterations from a converged solution was also considered. The disadvantages of this method is that the solution would always contain some contamination from the nonconverged solution and there is no way of knowing how many more iterations are needed to limit the impact of the samples collected before convergence was reached as determined by mass balance and AIP pressure convergence analysis specified in Section 3.6.1. For these reasons, the alternate method would also prove to be too computationally expensive for the amount of computational hours allocated for the project. Therefore the surface statistics presented in Figures 4.2 and 4.3 are for reference only and are not considered as true results of the simulations or as indicators of grid independent results.

The coefficient of pressure along the upper and lower centerlines was completed to assess differences in solutions resulting from differing grid densities. Figure 4.4 was generated showing the pressure coefficients for the three different solutions. The time averaged pressure along the surface of the upper and lower centerlines was extracted from the data used in Figures 4.2 and 4.3. Therefore, like above, this solution includes values obtained prior to a converged solution being obtained. While it was intended for use in determining grid independent solution, it can only be used for reference. The three grids closely compare with each other on both surfaces, but there are some differences and features to note.

In Figure 4.4, the lower surface lines show the shock region around $x = -0.43\text{m}$. The bumps in the coefficient in pressure for the lower surface around $x = -0.36\text{m}$ and $x = -0.32\text{m}$ correspond to the windows shown in Figure 4.3. The separated flow on the lower surface corresponds to the constant negative sloped section from $x = -0.30\text{m}$ to $x = -0.25\text{m}$. This range also corresponds to the largest difference between the lower surface pressure coefficients, which aligns with the differences noted in Figure

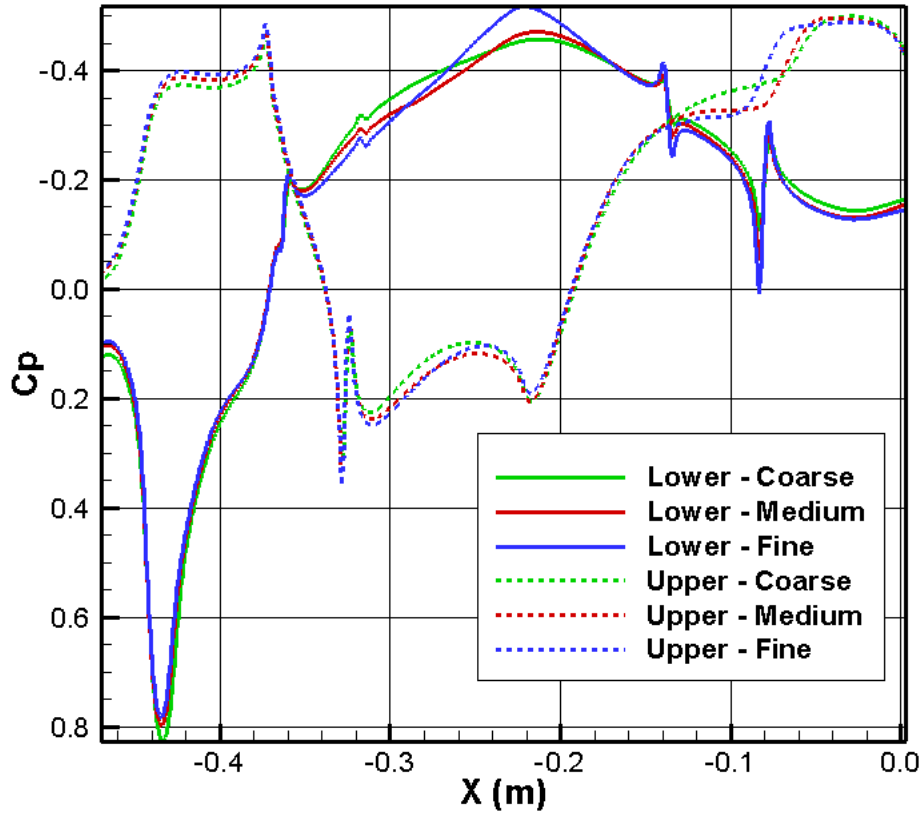


Figure 4.4: Comparison of coefficient of pressure along the upper and lower centerlines of three different grid densities to test data using 4th order DDES.

4.3. The last feature on the lower surface is the second set of windows starting at $x = -0.15\text{m}$.

The upper surface in Figure 4.4 clearly shows windows around $x = -0.36\text{m}$ to $x = -0.32\text{m}$ that align with windows on the lower surface as indicated by the spikes occurring at the lip of the window. Like the lower surface, the flow separated region on the upper surface is noted with lines of constant decrease in coefficient of pressure. The separation on the upper surface differs between solutions but is observed around $x = -0.08\text{m}$. In comparison to Figure 4.2, the differences between coefficient of pressure and the oil flow visualizations align with each other.

While visualizations of the instantaneous solution may not correctly represent the time averaged solution for unsteady solution, it provides insight of the features of the core flow through the S-duct. In this case, a slice along the center plane through the duct was analyzed. Figure 4.5 was generated using an instantaneous slice from the last iteration used in the 50,000 iteration average. Both the Mach color contours and the streamlines are used to represent the flow.

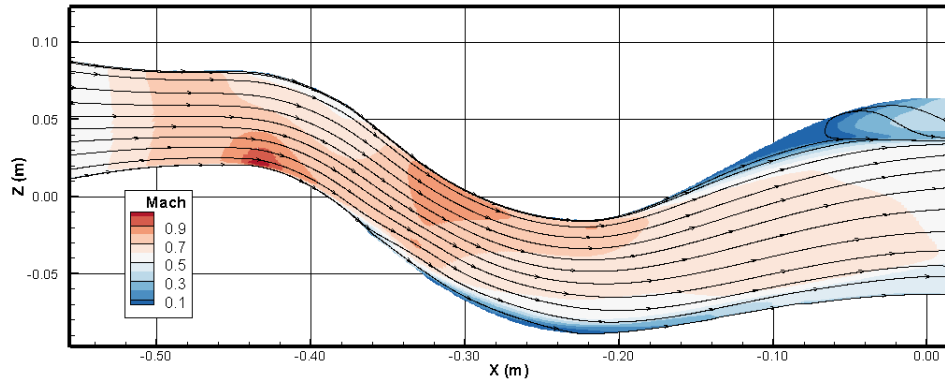
There are several commonalities between the solutions in Figure 4.5. First, all three plots exhibit the anticipated behavior of a shock forming in the throat of the duct exhibited by the red region on the lower surface around $x = -0.43$ m. Second, the low Mach regions exist in both the second bends of each turn, indicating the potential for flow separation. The core flow through the three different solutions also remain substantially higher than the low Mach regions on the upper and lower surface.

The largest difference between the grids is the increase in complexity of vortex shedding from the separated flow regions that occurs with increasing grid density. This trend is expected as DDES is a Hybrid/RANS LES model, applying an LES model in the core of the flow. With increasing the grid density, the cell size decreases and subsequently smaller scales of the turbulent vortices are resolved by LES. This change noted in the instantaneous slice of Figure 4.5 can help explain the changes between the solutions in Figure 4.7.

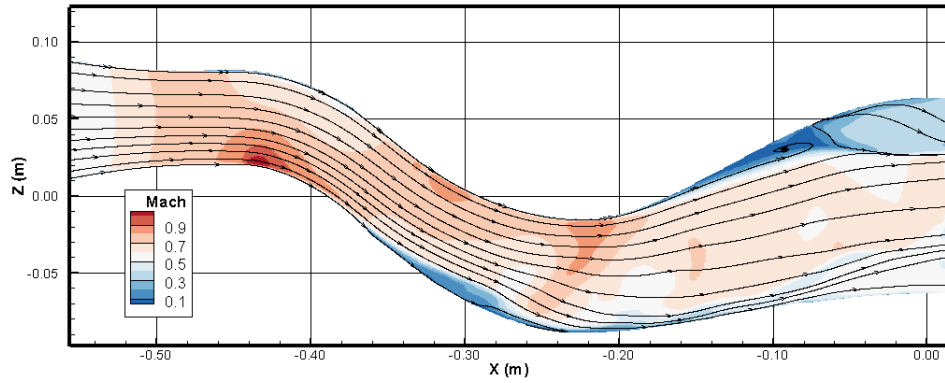
Overall, the assessment using the averages of the full time histories to generate the total pressure recovery, circumferential flow distortion, oil flow visualizations, and coefficient of pressure plots is not valid due to the inclusion of transients within the solution. While this was intended to prove grid independence, further evaluation was necessary to account for the corrupted time averaged solutions.

4.2.2 Modified Assessment of the First Order Temporal Grid Independence.

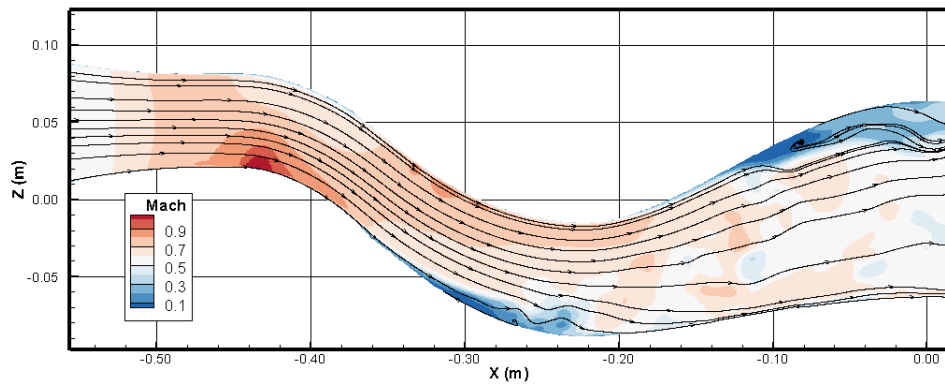
Since the mass flow rate were obtained from the end of the simulation it remains the same for the modified assessment of the 1st order temporal grid independence study, but the remaining metrics need to be appropriately account for the transients.



(a) Coarse



(b) Medium



(c) Fine

Figure 4.5: Comparison of instantaneous center plane slices of the three grids using 4th order DDES with a 1st order temporal scheme.

This was accomplished by truncating the full time histories of the AIP probes using a determined number of samples beginning at the end of the time history. As long as the end of the time history was a converged solution and it contained a sufficient number of iterations within the converged solution to be considered a statistically significant sample, this method of truncation could use the existing data collected. Since the mass balance cycled once every 50,000 iterations with a timestep of 2.0×10^{-7} seconds accounting for the 100 Hz frequency present in Section 3.6.4.1, this was used as the minimum number of samples that would need to be averaged to capture a cycle.

Figure 4.6 was then generated using only the fine grid using multiples of 50,000 iterations taken from the end of the same data set. The sample size follows the guidance obtained through the frequency assessment in Section 3.6.4.1. The 50,000 and 100,000 iteration samples from the end of the data set closely matched each other indicating that the end of the data set was collected from a converged solution. The 150,000 case also was close to the previous two discussed, but there are slightly more noticeable changes was the shape of the lower total pressure loss region. Further, Table 4.3 presents the quantitative argument constructed by averaging the total pressure recovery for the 40 AIP probes together. The circumferential flow distortion values were additionally averaged over the specified number of iterations and included in Table 4.3. The three data sets that used the smallest sample size were very close in terms of value for the average of the 40 AIP probes. While the circumferential flow distortion slowly increases, the change is not nearly as prominent as the increase in the total pressure recovery. The smallest sample size is the most conservative as it allows for the least contamination of a nonconverged solution within the collected data. Therefore, it was determined that 50,000 iterations should be used to assess the total pressure recovery mapping.

The results of Figure 4.1 was then repeated using the last 50,000 iterations from the full time histories to average for the three grids to produce Figure 4.7. In addition, Table 4.2 was recomputed in Table 4.4 for the overall quantitative total pressure recovery and circumferential flow distortion of the AIP. The total pressure maps in

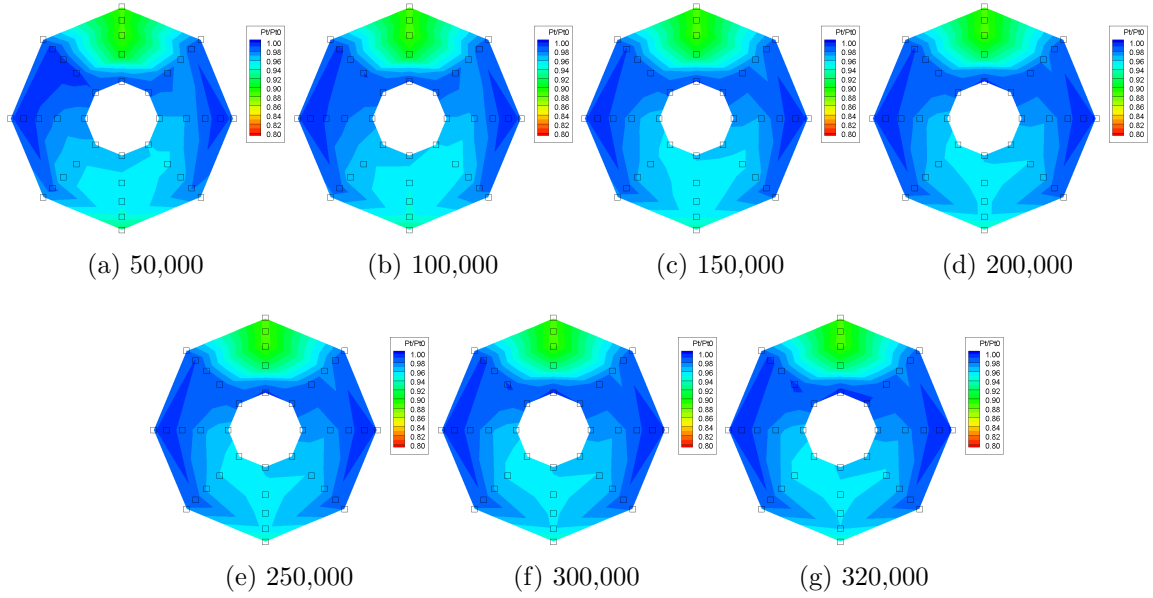


Figure 4.6: Comparison of total pressure recovery at AIP of fine grid by averaging last data points from history using 4th order DDES.

Figure 4.7 still show differences between the grid densities, but the medium and fine solutions are now closer in comparison. They both exhibit similar sized upper surface regions with reduced pressure recovery. Also, the lower surface for the medium and fine grid are more similar in magnitude and more consolidated towards the midplane of the duct than the coarse grid. This results in larger dark blue structures on the right and left side of the S-duct that have very high regions of total pressure recovery approaching perfect recovery in the medium and fine grid. In the assessment of the

Table 4.3: Total pressure recovery and circumferential flow distortion of the fine grid based on different sample sizes.

Sample Size	Total Pressure Recovery	Circumferential Flow Distortion
50,000	0.9673	0.0339
100,000	0.9671	0.0344
150,000	0.9673	0.0344
200,000	0.9685	0.0347
250,000	0.9682	0.0347
300,000	0.9690	0.0348
320,000	0.9694	0.0349

Table 4.4: Grid independence of total pressure recovery and circumferential flow distortion from last 50,000 iterations for the 1st order temporal scheme.

Grid	Total Pressure Recovery	Circumferential Flow Distortion
Coarse	0.9643	0.0323
Medium	0.9683	0.0346
Fine	0.9673	0.0339

total pressure recovery of the AIP, the difference between the coarse and medium grid are 0.4% and between the medium and fine grid is 0.1%. When using the full time history the same difference were 0.0% and 0.4% respectively, indicating stronger agreement between the medium and fine grid. Further, with the circumferential flow distortion the difference has been reduced to 2.1% error between the medium and fine grid and 4.7% between the coarse and fine grid. This decrease in the percent error is solely tied to the removal of the transients from the averaged values.

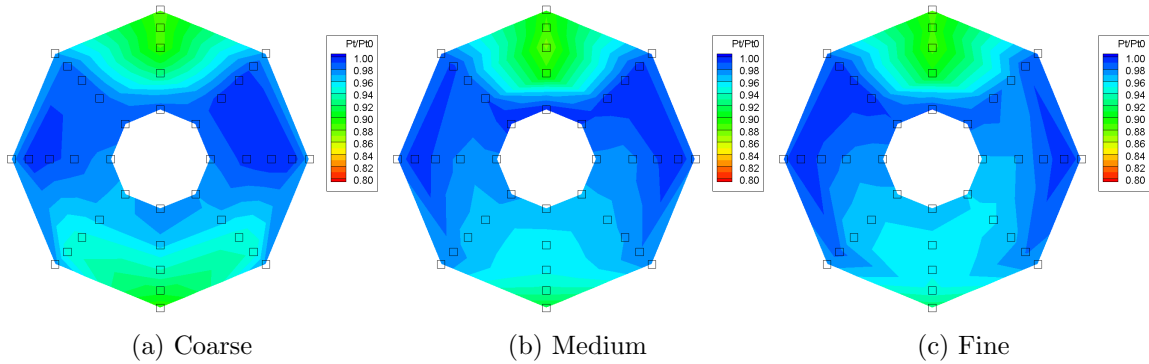


Figure 4.7: Comparison of total pressure recovery at AIP of three different grid densities using 4th order DDES using the last 50,000 samples from the time history.

In the grid independence assessment, the instantaneous values from Section 4.2.1 were still valid, but the the time averaged values needed to be reconsidered in order to remove the transients captured in the full time history, which was the intent of this section. Since the total pressure average of the AIP probes and the circumferential flow distortion were the two primary figures of merit, they were used as the main indication of grid independence. Although the solution was still changing between the medium and fine grids, with a 2% or less difference for the total pressure recovery

Table 4.5: Outflow mass flow for the three grids using a 2nd order temporal scheme.

Grid	Mass Flow Out
Coarse	2.17 kg/s
Medium	2.18 kg/s
Fine	2.17 kg/s

and circumferential flow distortion as well as the mass flow rate, it was considered sufficiently grid independent when using a 1st order temporal scheme.

4.2.3 Second Order Temporal Grid Independence. The scheme for the temporal accuracy was changed from a 1st order scheme, as used in the previous section, to a 2nd order scheme. The solutions were then continued with the 2nd order temporal scheme for two flow times to allow for transients to wash out from the change in temporal scheme prior to the collection of the flow statistics. As previously discussed in the previous section, due to the current implementation of surface statistic routines, the surface averaging statistics could not be turned off or reset. Therefore, the statistics were a collection of 1st order temporal solution, transient solution, and 2nd order temporal solution, so the results are not valid for comparison.

The mass flows are collected from the simulations using a 2nd order temporal scheme and compiled in Table 4.5. As with the 1st order temporal scheme grid independence study, the expect mass flow rate was 2.22 kg/s. The values are all close together, with the medium grid being the farthest away with a 0.8% difference. Both the coarse and fine grid are in close agreement with each other, which is counter intuitive, but the difference is so small it can be considered negligible.

Since the surface statistics, including the surface shear values, in the 2nd order temporal scheme continued off of the 1st order temporal solution, it contains all of the same surface statistics from the 1st order temporal cases. This is due to a limitation in US3D that once the surface statistics are turned on they cannot be turned off or reset. Furthermore, the number of iterations conducted with a 2nd order scheme was less than the number of iterations used for the 1st order scheme, so the resulting

figure does not represent any solution but a combination of two solutions and the transients washing out. For all these reasons, the the oil flow visualizations and coefficient of pressure plots derived from the surface statistics were not presented in this independence study.

Figure 4.8 displays the AIP total pressure recovery mappings for the 2nd order temporal scheme. The three AIP total pressure recovery mappings are plotted on the same scale to be compared with each other as well as the first independence study. The overall trend of the solution matches the first independence study as both cases have losses in the total pressure recovery caused by the lower momentum fluid from the boundary layer being convected into bulk flow through the counter-rotating vortices.

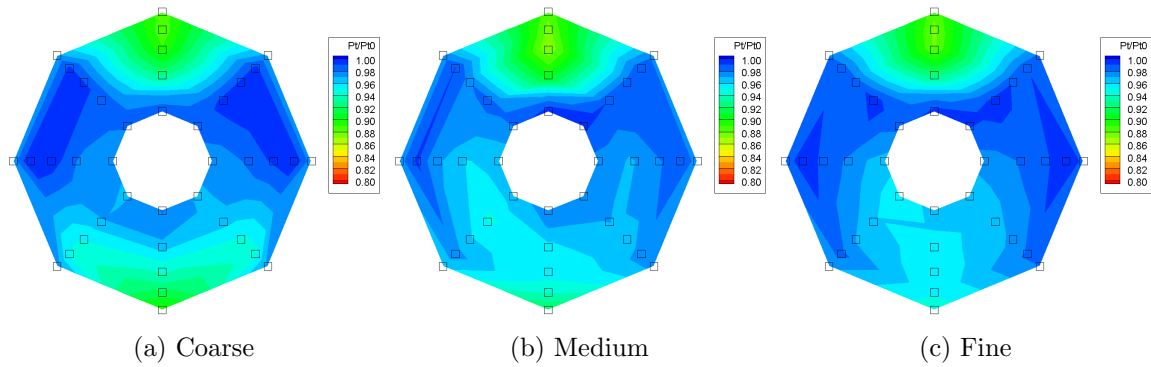


Figure 4.8: Comparison of total pressure recovery at AIP of three different grid densities using 4th order DDES using the last 50,000 samples from the time history for a 2nd order temporal scheme.

The upper surface for the three grid densities in Figure 4.8 show general agreement with both shape and magnitude. On the lower surface, there is a larger discrepancy between the three grid densities. First, the width of the loss in total pressure recovery along the lower surface decreases from coarse to fine. Second, the magnitude of the loss in total pressure recovery decreases slightly in the lower region, but it also becomes more consolidated along the midplane of the duct. This subsequently results in higher total pressure recovery on the left and right sides of the duct.

Table 4.6: Grid independence of total pressure recovery and circumferential flow distortion from last 50,000 iterations for the 2nd order temporal scheme.

Grid	Total Pressure Recovery	Circumferential Flow Distortion
Coarse	0.9648	0.0320
Medium	0.9638	0.0353
Fine	0.9688	0.0351

For a more quantitative argument, the total pressure recovery values for the 40 AIP probes are averaged together to produce the overall total pressure recovery at the AIP. The total pressure recovery and circumferential flow distortion for the three different grids used in the second independence study are compiled in Table 4.6. All three grids are close in overall total pressure recovery. The fine grid shows the largest total pressure recovery, which could have been qualitatively assumed from Figure 4.8 as it has the largest regions of darker blue. The largest percent difference comes from the comparison from the medium to the fine grid, which is 0.5%. One justification for this difference is that it matches the difference in the mass flow in Table 4.5. It is known from studies presented in Section 2.6 that higher mass flow rates cause reductions in total pressure recovery. The circumferential flow distortion shows that the medium and fine grid are much closer together than the coarse to medium grid with a 0.6% and 9.3% difference respectively. Overall, the quantitative argument paints a picture that the three grids are much closer together with the use of a 2nd order temporal solution, especially the medium and fine grid, than the mapping of the total pressure recovery presents.

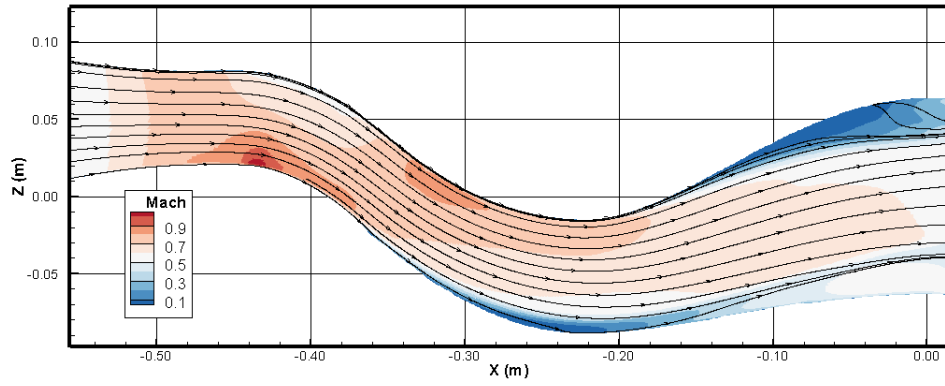
Similarly to the 1st order temporal independence study, instantaneous slices along the centerplane can be assessed to help explain differences in the solutions. Figure 4.9 was generated using the solution of the three grids with the last iteration from the 50,000 iterations used to average in Figure 4.8. All three grid densities present the shock in the throat. The shock region for the three solutions all have comparable magnitude and shape. Further, the second bend of both turns contain a region of low Mach flow. These regions contain reverse flow indicated in the streamlines indicating the presence of separated flow.

The core flows in Figure 4.9 all have similar magnitude, but there is a noticeable difference in the uniformity of the core flow. This difference extends into the low Mach regions in the separated flow. With increasing grid density, the amount of low Mach flow presenting in the core flow increases, resulting from the smaller cells allowing for resolution of smaller vortices in the LES applied away from the wall in DDES. Therefore, this change based on the grid density matches expectations. While these solutions are instantaneous and only along the centerline, the increased complexity of the flow solutions presented with increasing grid density aids in the understanding of the effect of grid density. This helps explain the differences that develop in the time averaged solution at the AIP in Figure 4.8.

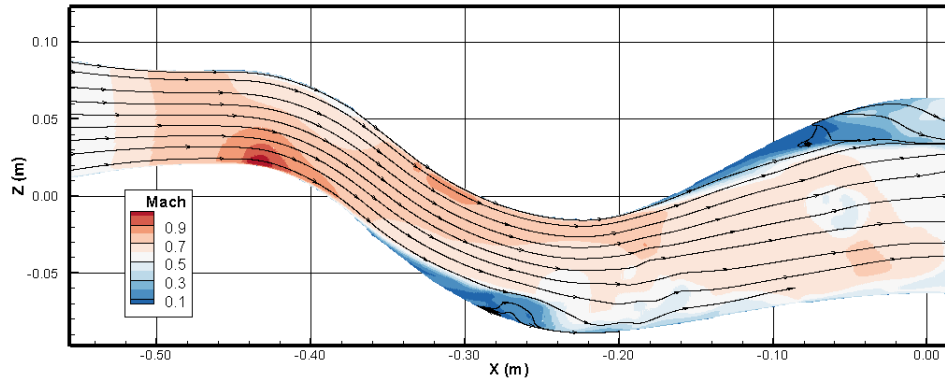
Like the 1st order temporal scheme results presented in Section 4.2.2, the AIP derived quantities using the last 50,000 iterations of the time histories provided the best justification for the grid independence. With the use of the 2nd order temporal scheme, the differences in between the medium and fine grid was less than 1% difference for total pressure recovery, circumferential flow distortion, and mass flow rate. This small percent difference satisfied grid independence with the use of the fine grid.

4.2.4 Grid Independence Comparison. The two independence studies can be compared to each other in order to distinguish differences stemming from the different temporal accuracy and from the different grid densities. The use of a 4th order spatial flux and DDES turbulence model with a fixed timestep of 2.0^{-7} seconds were held constant for both the cases. Since both studies concluded that the fine grid was sufficient for grid independence, it will be used in all future comparisons.

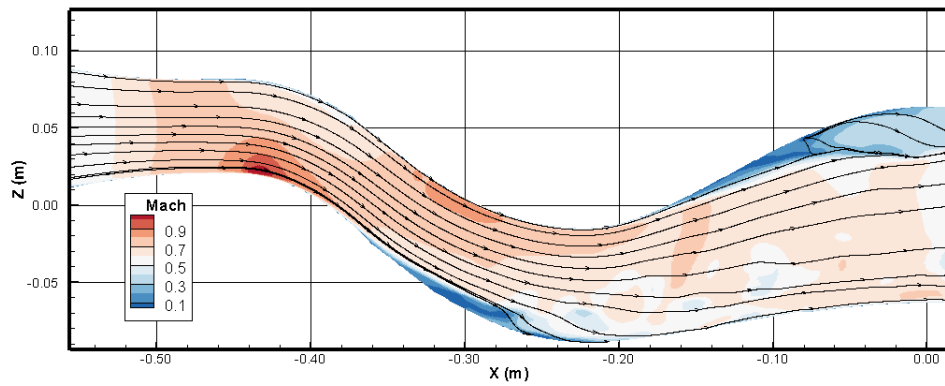
When Table 4.1 is compared to Table 4.5 both using only the last 50,000 iterations from the end of the time histories, it is noted that the range of the maximum percent difference decreased slightly from a 1.4% difference to a 0.8% difference. The decrease in the maximum percent difference may indicate that the increased accuracy of the model helped the three grids more closely align with the total pressure recovery. Additionally, the medium grid produced the highest mass flow rate in both studies,



(a) Coarse



(b) Medium



(c) Fine

Figure 4.9: Comparison of instantaneous center plane slices of the three grids using 4th order DDES with a 2nd order temporal scheme.

but it was still lower than the expected 2.22 kg/s. Logarithmic curve fits are commonly used for grid independence of steady simulations, and they were conducted on the mass flow rate of the grids, using mass flow as the dependent variable and number of cells as the independent variable. The curve fit applied should follow the shape created by the points and exponentially approach the mass flow value that would be achieved with an infinite number of points. Due to the kink created in the curves from the medium grid having the largest value, this analysis produced poor results and was not presented. While the fine grid that in the 1st order scheme produced the lowest value, in the 2nd order scheme the fine grid closely matched the coarse grid.

The mappings in Figure 4.7 and 4.8 can be compared to each other. Both cases are driven by the same flow phenomena, with lower momentum fluid from the boundary layer being convected into the bulk flow through counter-rotating vortices. As a result, both solutions display losses in the total pressure recovery occurring on the upper and lower surfaces. The shape and magnitude of these losses are in general agreement with each other. The coarse grid in both figures are very similar, with a 0.05% difference, the 2nd order had a slightly greater total pressure recovery. The medium and fine grids between the two temporal schemes showed greater differences in the total pressure recovery mapping, specifically on the lower surface. The 2nd order temporal solutions for the medium and fine grid appear less converged on the lower surface with slightly greater favoring one side or the other as opposed to the 1st order temporal solutions. This is also reflected in a 0.47% and 0.16% difference between the temporal schemes of the medium and fine grids respectively. Overall, the values for the 40 probe average across the AIP are similar between the temporal schemes.

The instantaneous slices for the three grids for both 1st and 2nd order temporal schemes in Figures 4.5 and 4.9 can be compared. The grids at both temporal schemes show the same general features of the shock region and low Mach regions. These features all present themselves in the same general locations between the grids and temporal schemes. Both sets of grids display the same trend of increased number of

pockets of low Mach flow being convected into the core of the flow with increased grid density. The smaller cells better capture the vortex shedding of the separated flow region by resolving smaller vortices. While the instantaneous slice poorly portrays the overall unsteady flow solution across the entire area of the S-duct, it helps understand the key features within the flow and the effect of increased grid density on the resolution of the solution.

4.2.5 Grid Independence Conclusion. Grid independence studies were conducted with three grids at two temporal schemes. The coarse, medium, and fine grids between both grid studies were the same and included wall clustering with $y^+ = 0.5$ or less within the S-duct. The fixed timestep was 2.0×10^{-7} seconds for both the 1st and 2nd order temporal schemes. Additionally, a 4th order spatial DDES model was used for each solution. These constants between solutions allowed for the direct comparisons between grid densities within each temporal scheme separately assessing the impact of the grid density. The results of the two temporal schemes were then compared to assess differences in the solution resulting from the temporal accuracy.

Grid independence was achieved with the use of the fine grid in both the two temporal schemes when assessing the total pressure recovery, circumferential flow distortion, and mass flow rate. When assessing the total pressure recovery mapping or the instantaneous centerline slice, there are noticeable differences between the solutions, but the medium and fine grids agree with each other more than with the coarse grid. The fine grid, without wall clustering, is also recommended for use with the WM-LES simulations.

The 1st and 2nd order temporal scheme comparison yielded the recommendation of using a 2nd order temporal scheme. While the comparison between schemes did not show a large difference, the use of a higher order reduces the amount of truncation error in the solution. As the fine grid was stable using a 2nd order temporal scheme, it should be used to better resolve the unsteady turbulent flow within the S-duct.

4.3 Comparisons to Test Data

The three simulation cases conducted on the structured grids using 4th order spatial flux scheme are compared to each other as well as to test data and previous modeling results. All three cases used the same inflow and outflow boundary conditions, as defined in Section 3.3, so the differences in mass flow rate is solely due to the numerical methods applied. The DDES solutions completed with both 1st and 2nd order temporal schemes are presented using the fine clustered grid as deemed necessary from the grid independence studies. The WM-LES solution is presented on the medium unclustered grid. While it was planned to complete the WM-LES simulation using the unclustered fine grid as indicated in Section 4.2.5, it was completed using the medium unclustered grid to reduce the computational expense and run time required. Although this may result in an unrefined solution that is not truly grid independent for the WM-LES solution, it is an area for further study.

Previous simulations and test results have been completed at a range of mass flow rates from 2.00 kg/s to 2.40 kg/s. To determine which mass flow rate the simulations conducted in this study match, the mass flow rates obtained for the three simulation cases are compared to the test cases in Section 4.3.1. Once the test case closest to the simulation cases completed is identified, the solutions of the are compared to the test data throughout Sections 4.3.2 to 4.3.5. The comparisons align with the primary objective and compare the results of using different orders of numerical methods, different grid types, and different turbulence models. The solutions used total pressure recovery, instantaneous slices through the S-duct, oil flow visualizations, and flow distortion to identify similarities and differences between the methods applied.

4.3.1 Mass Flow. The DDES and WM-LES simulation mass flows are compiled in Table 4.7 for comparison to each other and test data. The DDES solutions have a 0.7% difference between the different temporal schemes indicating there is close agreement with outflow mass flow rates. In comparing the WM-LES solution

Table 4.7: Outflow mass flow for the three cases all using a 4th order flux scheme.

Grid	Model	Temporal Scheme	Mass Flow Out
Fine-clustered	DDES	1st	2.15 kg/s
Fine-clustered	DDES	2nd	2.17 kg/s
Medium-unclustered	WM-LES	2nd	2.10 kg/s

and 2nd order temporal scheme DDES solution, a 2.9% difference is observed. This is the largest percent difference observed in any of the mass flow rate assessments. For the WM-LES simulation two different variables were changed simultaneously, the grid refinement and the turbulence model used. Further, the use of the medium grid could be too unrefined to accurately model the flow. To make a better comparison by only changing one variable, the DDES solution using the medium grid with the 2nd order temporal scheme was compared to the WM-LES solution. This comparison yielded a 3.7% difference, which is greater than the previously noted 2.9%, further indicating that the medium grid used in the DDES simulations does not predict the correct value. Even though the 2.9% difference is larger than previously encountered it remains a relatively small difference.

The simulation data presented by Lakebrink and Mani were collected at 2.00 kg/s, 2.22 kg/s and 2.40 kg/s and are shown in Figure 4.10 [4]. The RANS and DDES align with the mass flow of the simulation data points, but the test data was collected in smaller increments. The target mass flow rate for this study was the 2.22 kg/s case. The mass flow rates from the current study fall in between the 2.00 kg/s and 2.22 kg/s mass flow rates from the simulations conducted by Lakebrink and Mani, but most closely agree with the 2.22 kg/s mass flow rate, specifically with the grid independent DDES results. To select the closest mass flow rate from the simulation data, the percent difference from each of the values in Table 4.7 to the values from Lakebrink and Mani were calculated and averaged together. Using the averaged percent difference in mass flow rate, the 2.22 kg/s mass flow was determined to be the closest with the smallest average difference of 3.7%. Therefore, the 2.22 kg/s

(4.9 pps in the figure) mass flow rate will be used for comparisons of the simulation results.

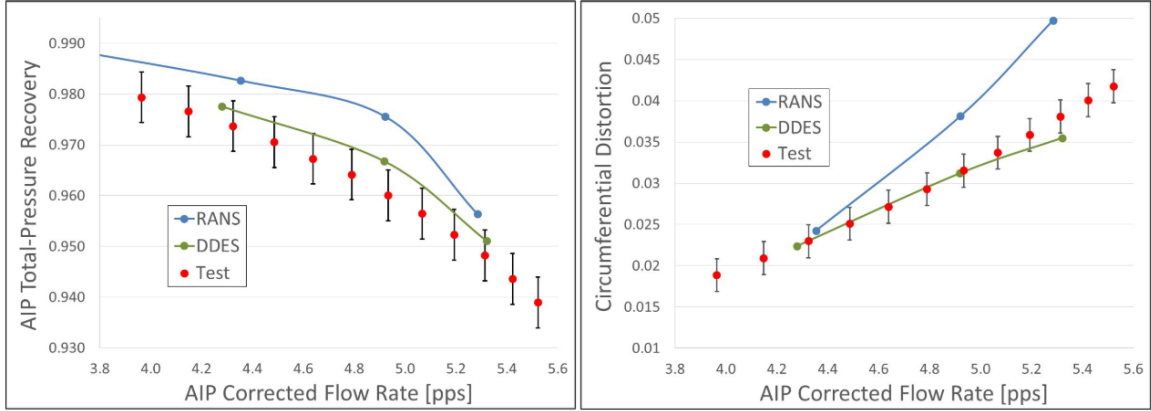


Figure 4.10: Total pressure recovery and circumferential flow distortion trends over a range of mass flow rates (Figure from Lakebrink and Mani [4])

While the solutions do not match the mass flow directly, it is not necessary as comparisons can still be made with the knowledge of the trends observed in Figure 4.10. Further, Lakebrink and Mani noted that the mass balance is very sensitive to small changes in the the geometry and flow parameters, so it is unlikely to be able to exactly match the mass flows of the simulations previously presented [4]. Additionally, the mass flow rate of the solutions in Table 4.7 fall near the 4.6 pps for the WM-LES solution and halfway between the 4.6 pps and 4.8 pps for the DDES solutions in Figure 4.10. This allows for the results from this study to be compared to test data that is closer in mass flow rate than the previous simulations, further adding to the assessment of the accuracy of the models used when comparing the total pressure recovery and circumferential flow distortion in the following sections.

4.3.2 Total Pressure Recovery. Since these three mass flow rates in Figure 4.7 are all slightly below the simulation mass flow of 2.22 kg/s, the total pressure recovery obtained in this study should be slightly higher. This aligns with the mass flow rate study Lakebrink and Mani conducted, shown in Figure 4.10 [4]. It concluded

that decreasing the mass flow rate increases the total pressure recovery when averaged across the AIP [4].

Figure 4.11 was generated comparing the three solutions from this study to the 2.00 kg/s and 2.22 kg/s test data points. The DDES solutions on the fine grid most closely match the 2.22 kg/s test data with a slightly higher total pressure recovery within the upper and lower surface regions. This matches the expectation based upon the mass flow rate achieved from the test data. Therefore, the test data from 2.22 kg/s will be used in all future comparisons to simulation in the remainder of this chapter, confirming the mass flow rate assessment from the previous section.

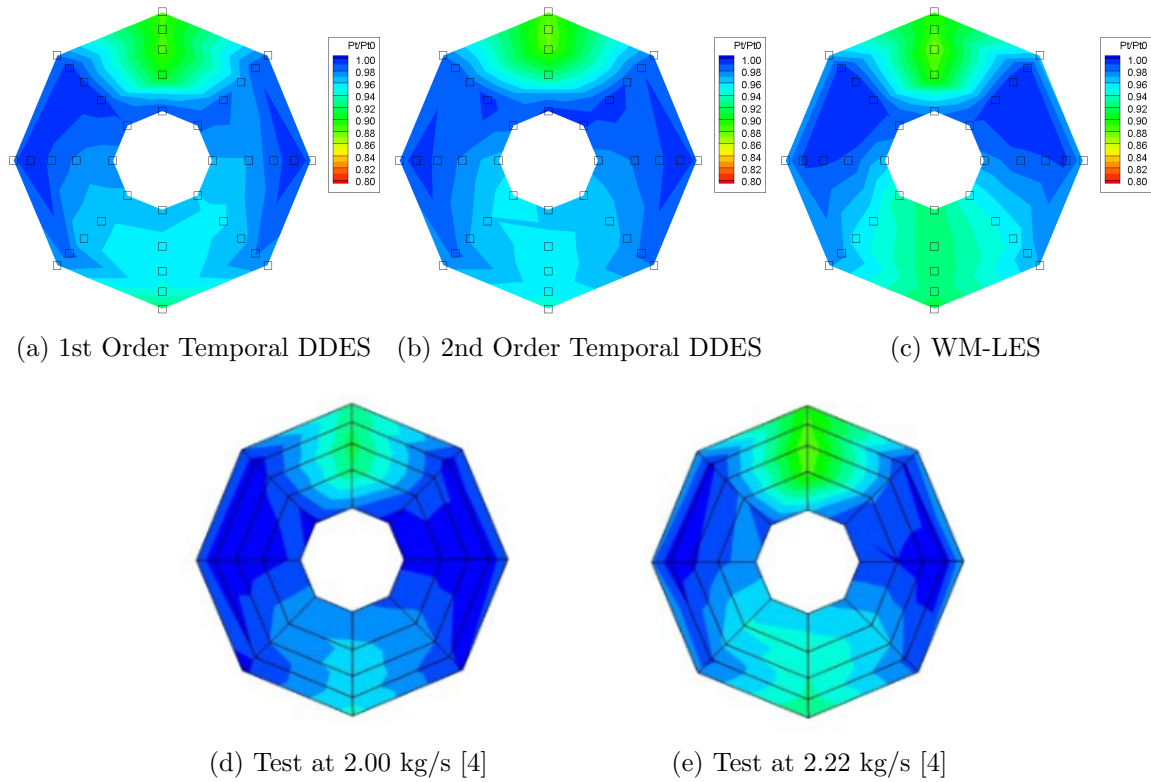


Figure 4.11: Comparison of total pressure recovery to different flow rates of test data.

The WM-LES solution was also compared to test data in Figure 4.11. The upper surface showed close agreement with test data for matching shape and magnitude. Alternately, the lower showed poor agreement, by over approximating the loss of total pressure, especially when considering the mass flow rate is less in the WM-

Table 4.8: Total pressure recovery for the three cases all using a 4th order flux scheme.

Grid	Model	Temporal Scheme	Total Pressure Recovery
Fine-clustered	DDES	1st	0.9673
Fine-clustered	DDES	2nd	0.9688
Medium-unclustered	WM-LES	2nd	0.9608

LES simulation then the test data. There are two potential solutions for the cause of the mismatch with the WM-LES solution. First, the medium grid was used as opposed to the fine grid that was determined to be needed from the grid independence study. Second, while the solution was averaged over the last 50,000 iterations, there was 1/3 less iterations collected with statistics for the WM-LES than the DDES cases. Although the same number of iterations is not required, as detailed in Section 4.2, but it may not have enough iterations to wash out transients introduced from initiating the wall model after a converged state was reached. Both of these reasons were not intended for the study, but were born out of necessity due to limitations in computational resources.

Table 4.8 shows the 40 AIP probe average of the total pressure recovery for comparison to the test data in Figure 4.10. The figure was adapted to produce Figure 4.12 including the WM-LES solution added in light blue, the 1st order DDES added in pink, and the 2nd order DDES added in purple for the total pressure recovery. This figure best shows the differences between the simulations and test data.

Both the DDES solutions from Table 4.7 fall above the trend line of the test data, but within the upper error bounds, indicating close agreement with test data. Further, these two DDES solutions fall closer to the test data trend line than the DDES trend line presented in green at a corresponding corrected flow rate of 4.7 pps. The WM-LES solution falls below then error bounds of the test data with a corrected flow rate of 4.6 pps, indicating more total pressure loss. Further comparisons of the total pressure recovery between the DDES solutions using different numerical methods and comparison to WM-LES are included in Sections 4.3.2.1 and 4.3.2.2.

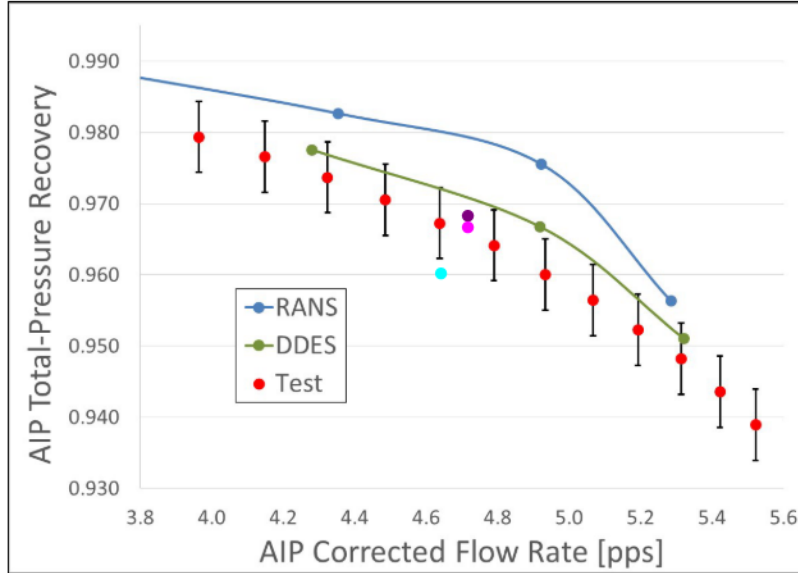


Figure 4.12: Total pressure recovery comparison with 4th order flux scheme solutions of 1st order temporal DDES (pink), 2nd order temporal DDES (purple), and WM-LES (light blue) added (Figure adapted from Lakebrink and Mani [4])

4.3.2.1 2nd and 4th Order Spatial Accurate DDES. The DDES solutions conducted in this study are compared to a previous DDES solution and the test data. The previous solution conducted by Lakebrink and Mani used a Bounded Central Differencing Scheme that is 2nd order accurate in time with 2nd order accurate in space DDES simulation using the same geometry [4]. The grid used by Lakebrink and Mani was a mixed grid with structured cells used on the S-duct and rakes for appropriate boundary layer resolution whereas unclustered cells were used to fill the remaining domain. The mixed grid has 186 million cells as opposed to the 148.3 million cells in the fully structured fine clustered grid generated in this study. The DDES solution from Lakebrink and Mani matches the mass flow rate of the test data [4]. Figure 4.13 shows the comparison of the different DDES solutions to test data. All four AIP total pressure recovery mappings use the same color mapping for direct qualitative comparison to assess the similarities and differences.

The same general features can be noted between the four images of Figure 4.13. First, the upper surface presents a large region with the highest total pressure

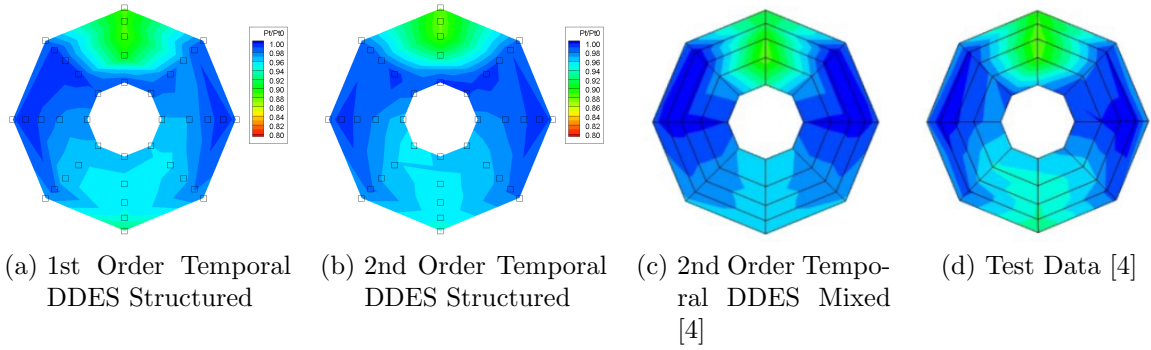


Figure 4.13: Comparison of total pressure recovery at AIP of DDES using 4th order spatial fluxes in a) and b) against 2nd order spatial fluxes in c) and test data in d).

recovery loss across the AIP. This feature results from the separated within the second turn of the S-duct. The separated flow generates an owl-face of the first kind, which in turn produces two counter-rotating vortices growing into the flow mirrored over the centerline of the S-duct. These counter-rotating vortices entrain low momentum fluid from the boundary layer into the flow. As the lower momentum fluid carries a lower total pressure in relation to the rest of the core flow, it results in the loss of total pressure recovery. A similar feature develops on the lower surface resulting from the separated flow in the first turn convecting down the S-duct. Since the distance from the first turn separation on the lower surface to the AIP is greater than that of the second turn separation, there is more mixing time between the lower momentum fluid and higher momentum core fluid. With more mixing time, the magnitude of total pressure recovery loss is less than the upper surface. The sides of the S-duct remain relatively unimpacted by the counter-rotating vortices forming in the separated regions and retain high total pressure recovery.

There are a number of differences in the loss in total pressure recovery on the upper surface in the images in Figure 4.13 when comparing the different DDES solutions to the test data. The loss in total pressure recovery of the 2nd order spatial DDES solution with a mixed grid protrudes farther into the core flow than test data shows. Conversely, the 4th order spatial DDES on the structured fine grid does not

have the loss in total pressure recovery on the upper surface protrude as far into the flow as the test data. As the mass flow rate for the 4th order DDES solutions are slightly lower than the test data, the reduced loss in total pressure recovery in size and magnitude is expected. The overall width of the feature on the upper surface also differs between the solutions. The mixed grid captures the pinching in of the loss in total pressure recovery region just above the solution as noticed in the test data better than the structured grid cases. The 1st order accurate temporal structured solution does have some pinching in, but not nearly to the extent of the mixed grid or the test data. The 2nd order accurate temporal structured solution poorly captures the pinching in of the region, which could be attributed to the 2nd order temporal solution not being run for as long as the 1st order temporal solution to allow for transients to fully wash out from the solution.

Differences between the images in Figure 4.13 also exist for the loss in total pressure recovery on the lower surface. Both structured grid solutions better capture the magnitude of the loss in total pressure recovery better than the mixed grid for the feature on the lower surface. While the structured grids are closer in magnitude to the test data, they do not match exactly, but this was expected because of the lower mass flow rate used in the DDES solution. The width of the region on the lower surface is also better predicted by the structured grids than the mixed grid. It is important to remember that the difference in grid type is also attributed to a different spatial accuracy. Since the structured grid uses a 4th order spatial accuracy as opposed to a 2nd order spatial accuracy, it contains less truncation error and its subsequent numerical dissipation. The reduced truncation error was the reason structured grids were used in this study. This difference in dissipation accounts for the difference between the width of the loss of total pressure recovery on the lower surface. The structured grids also have a bean shape more representative of the shape in the test data than the mixed grid. With this comparison, it is also noted that the mixed grid is very symmetrical unlike the structured grids and test data. The 2nd order accurate temporal scheme with a 4th order spatial accuracy on a structured grid generated

in this study most closely matches the test data out of the three different DDES solutions.

4.3.2.2 DDES and WM-LES. The structured grid solutions for DDES and WM-LES are compared to test data in a similar fashion to the three DDES solutions. Figure 4.14 presents the DDES and WM-LES solutions using a 4th order accurate spatial and 2nd order accurate schemes on a structured grid to test data. This comparison highlights the differences between the two different turbulence models. Much like the DDES comparison completed in the previous section, the same flow phenomena exists in both solutions and generates similar features in the total pressure recovery at the AIP. Specifically, there are two pairs of counter-rotating vortices, one on each the upper and lower surface, that are responsible for the two regions indicating a loss in total pressure recovery.

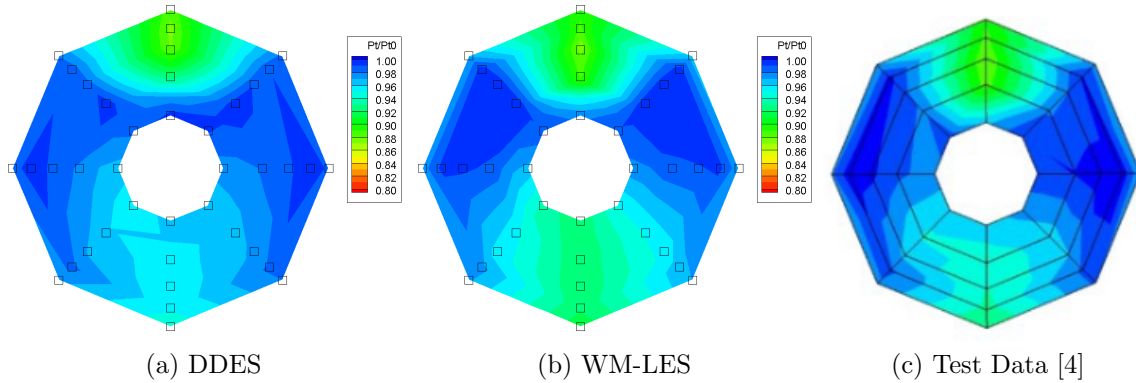


Figure 4.14: Comparison of total pressure recovery at AIP of DDES and WM-LES on structured grids to test data.

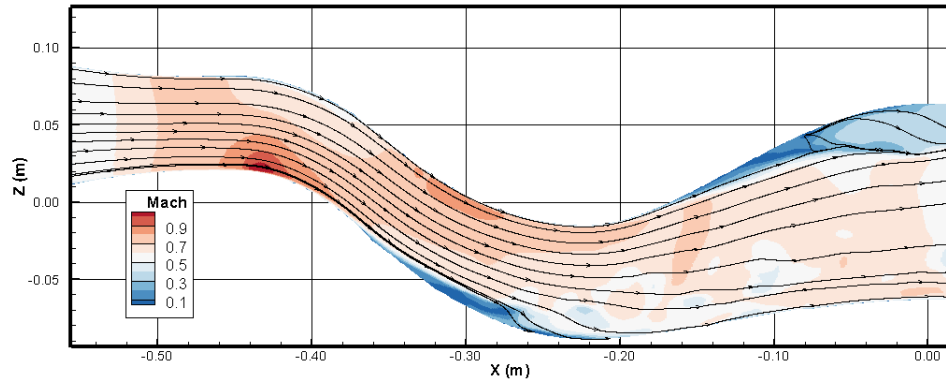
While the magnitude of the region on the upper surface for the simulations in Figure 4.14 compare closely to test data, the shapes show differences in the solutions. First, the width of the WM-LES more closely matches the test data than the DDES solution. This includes the pinching in that occurs just above the surface on the sides of this region on the upper surface. Even though the WM-LES better captures these features, it does not pinch in nearly as far as the solution from the test data. Second, the distance the loss in total pressure recovery protrudes into the core of the flow is

compared. Once again, the WM-LES solution most closely matches the test data. In comparison, the DDES solution does not protrude as far into the flow and flattens out more as it protrudes down into the core flow.

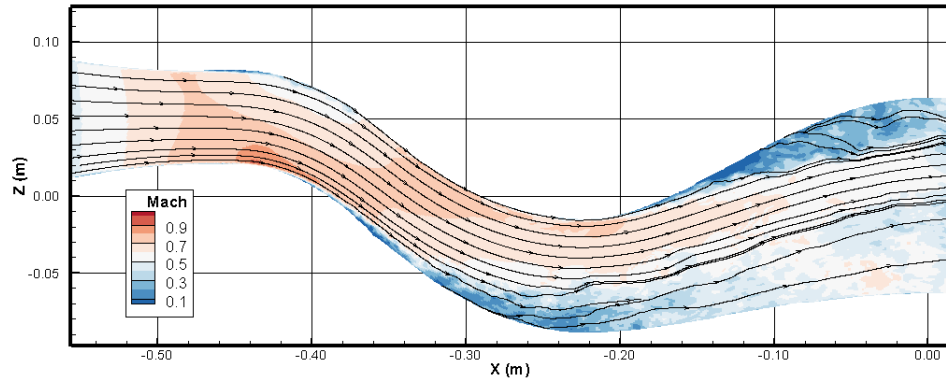
The solution in the lower half of the DDES and WM-LES also show differences between each other and between the test data in Figure 4.14. Both solutions capture the pinching in near the surface in the lower region as noted on the upper surface. The pinching in feature occurs from the counter-rotating eddies moving into the core of the flow, and they are wider than region along the centerline that convects low momentum fluid into the vortices in the core of the flow. Further, the counter-rotating vortices are sweeping the high momentum fluid from the core of the flow towards the base where the pinching occurs. While the DDES solution underpredicted the magnitude of the loss in total pressure recovery compared to the test data, the WM-LES solution overpredicts the loss. Additionally, the shape in the lower region is more dispersed than the DDES or test data. This includes the protrusion of the region extending higher into the flow for the WM-LES solution. Since the medium grid was used for the WM-LES solution, it was too coarse to appropriately resolve the flow, and as a result the loss in the lower region bleeds outward. Further, as a result of underresolving the flow, it underpredicts the amount of energy in the flow further increasing the loss in total pressure.

4.3.3 Instantaneous Center Plane Slice. As with the grid independence studies, the instantaneous center plane slice can be visualized to assess the flow. Figure 4.15 shows the comparison of the DDES and WM-LES simulations conducted with 4th order spatial and 2nd order temporal to the DDES solution from Lakebrink and Mani [4]. No visualizations of this type exist from test data, so only the different models can be compared for similarities and differences.

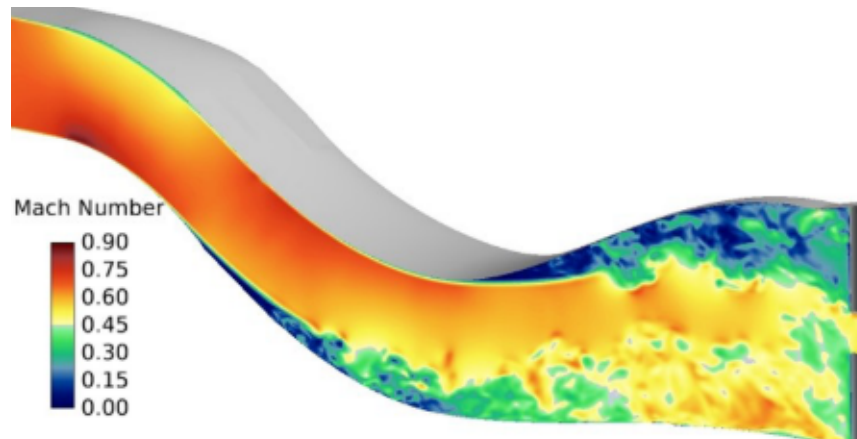
Figure 4.15 shows similar features within the high Mach region in the throat for the three solutions. The general shape is consistent, but the overall magnitude varies the most between the WM-LES and DDES solutions. The use of too coarse of a grid



(a) Structured DDES



(b) Structured WM-LES



(c) Mixed DDES [4]

Figure 4.15: Comparison of instantaneous center plane slices of 4th order structured DDES and WM-LES solutions to 2nd order mixed grid DDES solution.

for the WM-LES solution would contribute to this degradation in overall strength of the shock region within the throat. On the upper surface beginning at the throat, all solutions present a slight thickening of the boundary layer. With the flow being forced to turn, the flow near the upper surface impacts the first bend on the upper surface and slows down. This behavior was anticipated as Wellborn *et al.* previously documented the feature [11].

Moving down the S-duct in Figure 4.15, the low Mach region develops on the lower surface of the solutions. While difficult to pinpoint the exact location on the isometric representation, the DDES solutions have a small gap in between the high and low Mach regions that is missing within the WM-LES solution. The general shape of the three pockets of separated flow are similar with the two DDES results being the most similar. The WM-LES solution has more eddies that roll off the separated region into the core of the flow. Both DDES solutions show medium velocity in the region following the separated flow on the lower surface that accelerated downstream. The WM-LES solution also accelerates downstream.

Further downstream within the second bend of the second turn, the lower surface for the WM-LES solution in Figure 4.15 is still at a lower velocity than both of the DDES solutions. This results from more eddies shedding into the flow from the separation on the lower surface. Additionally, this reflects in Figure 4.14 with the larger region on loss in total pressure along the centerline in the lower half of the duct. The upper surface low Mach and separated flow are very similar between the three solutions. The DDES solution conducted in this study shows the least number of eddies rolling off of the separated flow regions. Conversely, the WM-LES results show the greatest amount of eddies rolling off the upper surface separation, but this was expected. All three show a clear distinction between the eddies shedding from the upper separation to the core flow in the same location. Further, this region has good agreement between the DDES solution from Lakebrink and Mani to the WM-LES solution in terms of thickness and general shape of the higher velocity core flow.

Although this comparison was made, and differences were identified, these differences are valid only for the instantaneous slices that were compared. These comparisons may not appropriately represent the overall solution as they are not the time averaged flow solution.

4.3.4 Oil Flow Visualizations. The time averaged shear stress on the surface of the S-duct was used to make oil flow visualizations. Oil flow visualizations were generated for the separated flow regions on both the upper and lower surface. Figures 4.16 and 4.18 show the 1st order temporal DDES and 2nd order temporal WM-LES solutions to the DDES solution and test data from Lakebrink and Mani for the upper surface and lower surface. The oil flow visualizations are combinations of the three components of the wall shear stress that are time averaged and arrows are added to aid in the identifying the directionality of the flow. The color contour presented is the axial shear stress, which is blue when negative to highlight reversed flow. As specified in Section 4.2, 2nd order temporal DDES solution for surface averaged values was not available as it was a combination of 1st and 2nd order temporal solutions. Additionally, it was noted that the 1st order temporal DDES results were contaminated with the transients of a nonconverged flow accounting for their poor representation of expected flow characteristics. Even though there were limitations in the statistic data collected, comparisons can still be made among the solution and test data.

The upper surface oil flow visualizations in Figure 4.16 show great differences between the solutions obtained in this study to the test data. While the validity of the 1st order temporal DDES solution was discussed, it still shows the negative axial shear stress and the two primary spiral nodes. The negative axial shear correlates to a condition of reversed flow as further indicated by the arrows on the oil flow lines. The location of this also generally agrees with the test data. It is important to remember that this DDES image does not appropriately represent the solution obtained, and recapturing the statistics would have provided a better comparison.

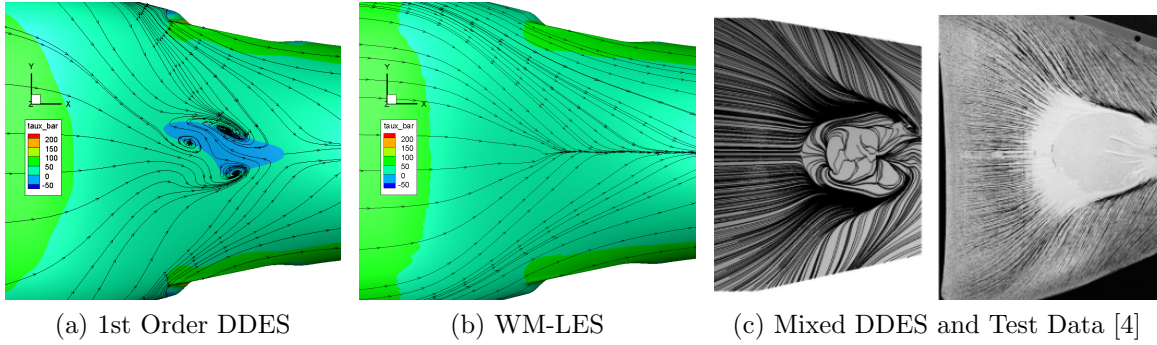


Figure 4.16: Comparison of upper flow separation region of the 1st order temporal DDES and WM-LES solutions compared to mixed grid DDES and test data.

The WM-LES solution for the upper surface in Figure 4.16 does not show any negative shear stress, nor does it have any spiral nodes. All the arrows on the WM-LES oil flow lines point downstream. Based on this image alone it could be concluded that the reversed and separated flow on the upper surface did not occur. This conclusion contradicts the results presented in both the total pressure recovery in Figure 4.14 and the instantaneous Mach contour of 4.15. The loss in total pressure recovery on the upper surface of the AIP map matches prior test data that is known to be caused by counter-rotating vortices that are generated from spiral nodes within the owl-face of the first kind. Further, reversed flow is clearly identified on the Mach slice along the upper surface following the second bend. Additionally, the wall model is an equilibrium wall model with the assumption of no pressure gradients, but the separation occurs within a region of strong pressure gradients. Therefore, the conclusion was corrected to the wall model applied was not the best suited for the flow.

Since the wall model provides the shear on the surface, the wall model used could cause the lack of owl-face development. But, with the AIP and Mach slice presenting appropriate features, the more likely culprit is the wall model used combined with the resolution of the grid. Figure 4.17 was generated to test this theory. Both images use the same color contour scales and streamline generation to provide a direct comparison. As expected, the instantaneous solution shows more complexity

of the flow than the averaged solution. The regions of negative axial shear stress align with individual eddies rolling over the surface. While spiral nodes are not shown, the unsteady solution shows individual locations with oil flow lines pointing upstream. As a result of the large scale spiral nodes from being present, there is not a region of constant negative shear stress. This then allows the mixture of negative and positive axial shear stress within the instantaneous solution to exist. Therefore, when averaged the negative axial shear is absent from the upper surface of the WM-LES solution. It was previously noted that the WM-LES grid was too coarse for the flow, which could help the development of the spiral nodes that are currently missing in the solution.

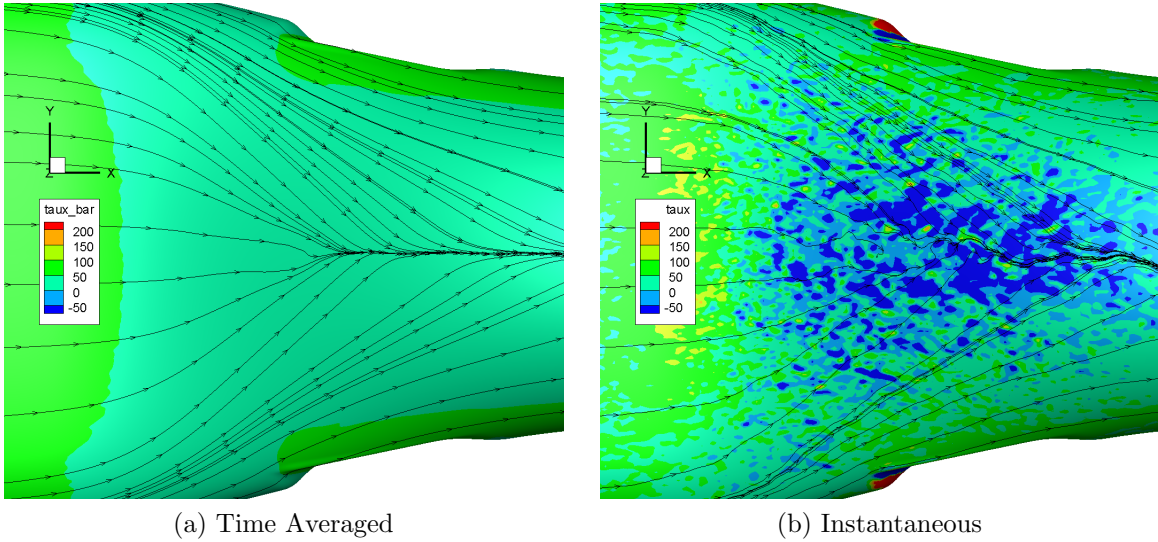


Figure 4.17: Comparison of upper flow separation region of the time averaged WM-LES to the instantaneous WM-LES.

The DDES solution obtained in this study for the lower surface compares with the DDES solution from Lakebrink and Mani [4] and test data as shown in Figure 4.18. The three rectangular windows in the images make reference points between the solutions. The spiral nodes in the structured DDES has spiral nodes in the general location that are observed in the mixed grid DDES. Further, the oil flow lines between the DDES solution are in agreement with each other. The structured DDES solution does suffer from having both spiral nodes being fully developed, but this resulted from

the surface statistics being initiated too soon. The locations of the flow separation also align with with the test data.

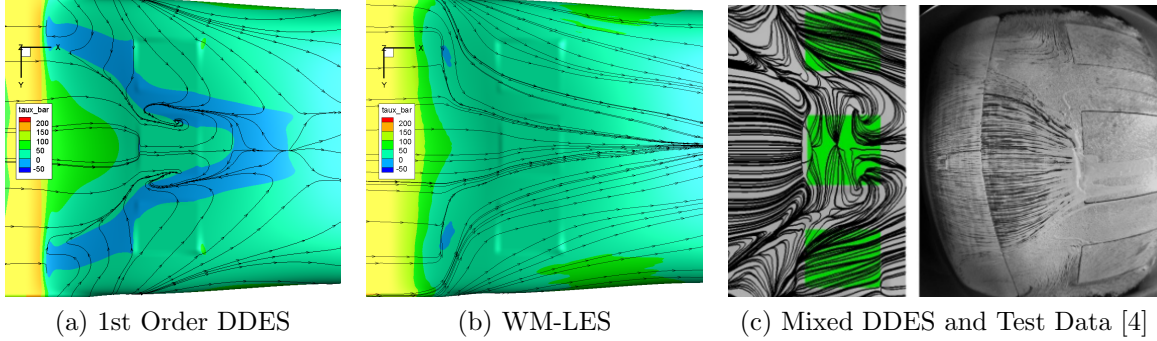


Figure 4.18: Comparison of lower flow separation region of the 1st order temporal DDES and WM-LES solutions compared to mixed grid DDES and test data.

Similar to the upper surface, the WM-LES results on the lower surface also shows a lack of reverse and separated flow in Figure 4.18. While this was not expected, the same hypothesis made for the upper surface regarding the lack of spiral nodes to hold continuous regions of negative axial shear was proposed for the lower surface. Figure 4.19 shows the time averaged solution on the lower surface compared to the instantaneous solution. As noticed with the upper surface, the lower surface shows a large amount of negative axial shear stress that does not appear on the time averaged solution. Again, this region has mixed positive and negative axial shear providing an average that does not fully show the negative axial shear. Further, inspection of the oil flow lines indicates small localized spirals within the flow, but no large scale spiral nodes expected for S-duct flow.

4.3.5 Circumferential Flow Distortion. Following the post processing of the AIP probe time histories, the circumferential flow distortion value could be obtained. Following the lessons learned in the first grid independence study, the circumferential flow distortion values over the last 50,000 iterations were averaged to provide the steady state distortion. Since the probe histories were filtered to match the data collection rate from testing of 4×10^{-5} seconds, the 50,000 iterations at 2×10^{-7} seconds

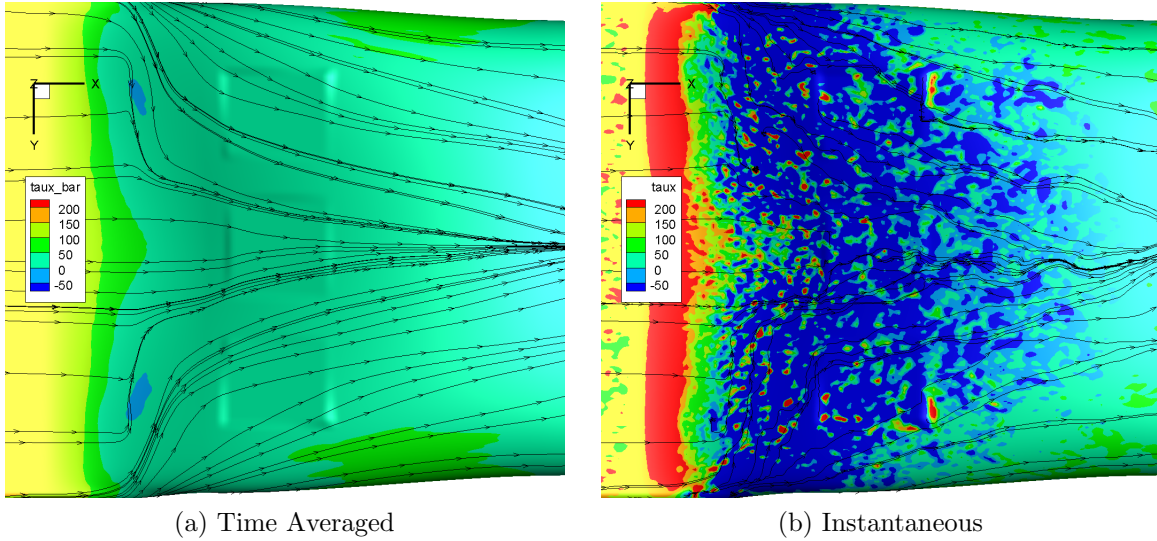


Figure 4.19: Comparison of lower flow separation region of the time averaged WM-LES to the instantaneous WM-LES.

Table 4.9: Circumferential flow distortion for the three cases all using a 4th order flux scheme.

Grid	Model	Temporal Scheme	Circumferential Flow Distortion
Fine-clustered	DDES	1st	0.0339
Fine-clustered	DDES	2nd	0.0351
Medium-unclustered	WM-LES	2nd	0.0307

corresponded to only 250 samples. The averaged circumferential flow distortion for the three cases are compiled in Table 4.9. The WM-LES solution and 2nd order temporal DDES solutions present the smallest and the largest circumferential flow distortions, respectively. The 1st order temporal DDES solution falls between the other two, but is closer to the other DDES solution.

Following the same methods applied to the total pressure recovery, the circumferential flow distortions values are overplotted on Figure 4.10 to produce Figure 4.20. Once again, the 4th order flux schemes were included with the WM-LES solution added in light blue, the 1st order DDES added in pink, and the 2nd order DDES added in purple for the circumferential flow distortion in Figure 4.20.

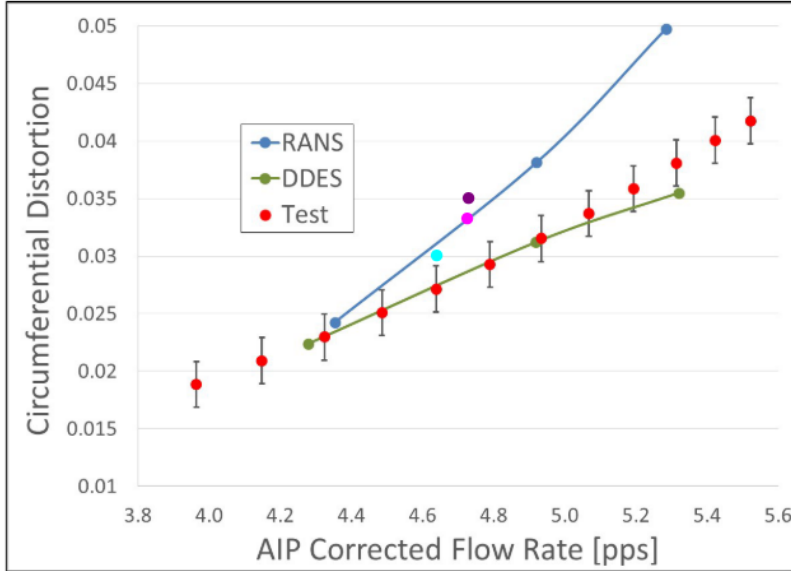


Figure 4.20: Circumferential flow distortion comparison with 4th order flux scheme solutions of 1st order temporal DDES (pink), 2nd order temporal DDES (purple), and WM-LES (light blue) added (Figure adapted from Lakebrink and Mani [4])

All three solutions completed using the fully structured grid with a 4th order flux scheme in Figure 4.20 over predicted the circumferential flow distortion. The WM-LES solution was closer to the test data than the DDES solutions, but they were all above the error bars of the test data. This is the opposite result of the total pressure recovery when the WM-LES solution was farther away from the test data than the DDES solutions. Based upon extrapolations of the test data in the figure, approximations of the difference from the solutions to the test data could be made. The WM-LES had a 13% error while the 1st order and 2nd order temporal DDES solutions had a 16% and 21% error respectively. While these errors were approximated, they still are larger than acceptable.

4.3.6 Comparison to Test Data Conclusion. The DDES and WM-LES solutions using 4th order spatial fluxes were obtained and compared to test data and DDES solutions from Lakebrink and Mani [4]. This successfully completed the primary objective of assessing the increase of accuracy through the use of higher

order numerical methods enabled by a structured grid as well as assess the validity of the WM-LES model for this flow. The generation of the fully structured grid on this complex geometry was the most important step as it enabled the further completion of simulations to address the primary objective. Although a 6th order numerical scheme was desired, the skew of the grid was too great to be supported with this scheme. The reduction from a 6th order scheme to a 4th order scheme still provided an increase from previous studies conducted with a 2nd order flux scheme on grids that were not fully structured. The two aspects of the primary objective in the current study were individually addressed to declare the overall success of the primary objective.

First, the 2nd order temporal scheme and 4th order flux scheme combination on the fine clustered grid generated in this study displayed higher accuracy than the mixed grid solution with regards to total pressure recovery at the AIP. The plane averaged value for total pressure recovery closely agreed with test data and the total pressure recovery mapping more closely matched the expected shape from test data. Additionally, the total pressure recovery mapping matched expectations by having a slightly higher magnitude than the test data due to the effect that the mass flow rate was lower than the test data. Conversely the circumferential flow distortion values from this structured approach was farther from the test data and fell outside the error bounds, which was worse than the mixed grid for this metric. The remaining time averaged metrics could not be compared with transients within the average and limitations of US3D. While the AIP metrics indicate an increased accuracy through the use of higher order numerical methods, the instantaneous slices showed less resolved eddy content than the mixed grid solution prompting further questions regarding the validity of the DDES model within US3D.

Second, the WM-LES model was successfully applied to the unclustered structured grid with a 4th order flux scheme and 2nd order temporal scheme. This was a major achievement as the WM-LES model within US3D had previously only been applied to relatively simple flat plate, wedge, and conic geometries. While the grid used was too coarse to fully resolve the flow as indicated on the AIP mapping, it did

better capture the overall shape of the test data better than the DDES solutions. It also resolved more eddies within the flow than both the mixed grid DDES solution and structured DDES solutions. Most importantly, this was accomplished with 1/3 of the cells, drastically reducing the computational cost of the simulation. Further, the oil flow visualizations identified the importance of not including the zero pressure gradient assumption within the wall model. Even with a more refined grid, this assumption may have prevented an accurate solution. While the current WM-LES solution does not fully increase the accuracy of the model, the efforts completed identified the path of modifications necessary for the WM-LES model in US3D to be an accurate S-duct flow prediction tool.

4.4 Comparison of Pressure Recovery Mapping Methods

The number of probes and their locations on the rake are determined by standards, but questions are being raised regarding the justification for those points. Using 40 probes in the AIP discretizes the cross sectional solution when computing the total pressure recovery as well as the mapping of the total pressure recovery. In the CFD community it is well understood that an overly discretized solution may be too unrefined to fully capture the solution, leading to the requirement of grid convergence studies. The number of probes and their locations come from standards that date back to 1978, with primary applications on straight inlets with very little complex geometry [19]. Today, increased understanding of duct flows and the ever expanding complexity of inlet designs prompts the inlet designers, experimentalists, modeling community, and engine designers to question the existing standards. In order to assess these growing concerns, the 40 probe AIP solution can be compared to a temporally averaged solution at a plane across the flow at the AIP.

Figure 4.21 shows the comparison of the 40 probe AIP to the 86,166 point plane averaged solution from the fine grid interpolated onto a 72,000 point structured grid. While the assessment has already been made that the flow statistics was initiated prior to reaching a converged solution, the two plots in the figure were collected over

the same iterations and can be used to make a direct comparison. For this reason, the results from testing are not shown. The total pressure recovery for both are plotted on a color contour with the same range and color scheme. Overall, some of the general features of the lower total pressure recovery pocket on the upper surface and the shape of the pocket on the lower surface into the core of the flow are shared between the plots. The exact shape of the solutions differ, with the plane averaged solution showing greater detail into the shape of the total pressure recovery. Additionally, the plane averaged solution provides a plot that includes the middle of the duct and extends all the way to the wall. The cross sectional velocity streamlines are plotted over the total pressure recovery contour. The streamlines show the greatest differences between the two solutions. The 40 probe AIP solution only resolves two vorticies, one in the upper left of the duct and one in the lower right of the duct. Neither of these to vorticies are strong, but both were expected. The plane averaged solution clearly resolves the four large expected vorticies consisting of two sets of counter-rotating vorticies on the upper and lower surface. In addition, two smaller vorticies occur at the 4 and 8 o'clock locations near the surface of the S-duct. These smaller vorticies extend from the vorticies formed in the rounded corners of the D-shaped duct.

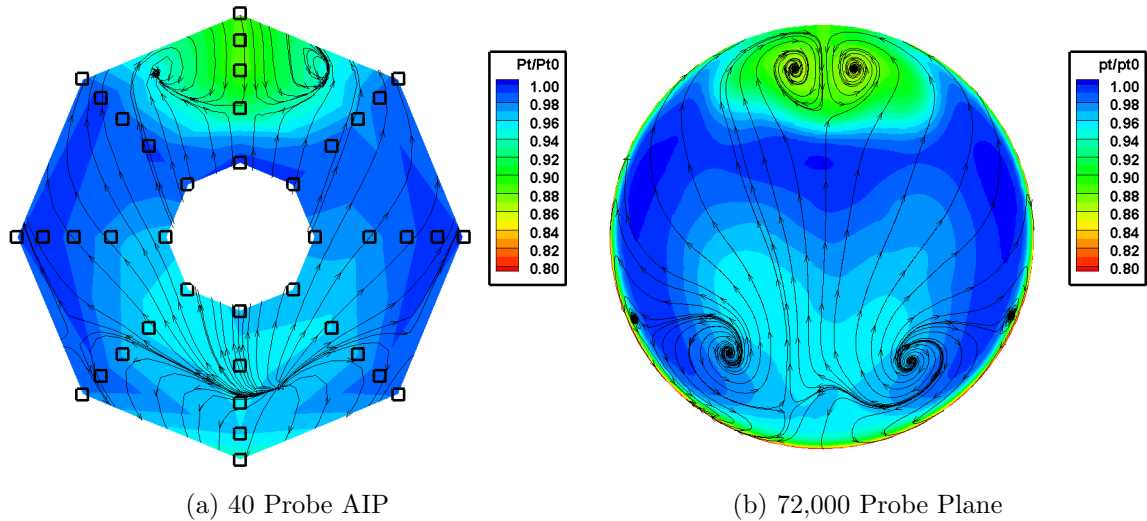


Figure 4.21: Comparison of 40 probe AIP solution to the 72,000 point plane averaged solution from the full 320,000 sample time history of the fine grid.

The 40 probe AIP and plane averaged solution can further be assessed by comparing the quantitative average of the points used to generate the solution. Using the full solution for the 40 probe AIP, Table 4.2 indicated the total pressure recovery for the fine grid to be 0.9694. The full solution using the 72,000 point interpolation of the full time averaged plane across the AIP yielded a total pressure recovery of 0.9691. The 72,000 point average was lower than the 40 probe average, which could be attributed to the increased total pressure loss from boundary layer on the wall. The difference between the two total pressure recoveries was 0.02%. This small difference was a coincidence resulting from the 72,000 probe plane average balancing out the more low total pressure recovery it displays with more high total pressure recovery regions to match the 40 probe AIP average. While the quantitative total pressure recovery was almost identical, Figure 4.21 showed that the solution is extremely different as far as understanding the features of the flow and the mapping of the flow distortion, especially in regions in between the rakes of the AIP. In order to better map the flow characteristics and capture the peak total pressure loss, the use of more probes or rotating the AIP within the duct to capture more locations should be considered.

4.5 Slices from Video

The AIP total pressure recovery mappings presented throughout this chapter from both the 40 AIP probes and from the complete plane as in Section 4.4 provide information on the average total pressure recovery profile of the flow, but it does not have information on how the instantaneous total pressure recovery profile changes from one iteration to the next. With unsteady flow it is expected that the solution differs throughout the solution. To expand the understanding of how the instantaneous solution progresses, a video was made for both the 2nd order temporal DDES and WM-LES solutions using structured grids. While videos do not display well on paper, a collection of frames from the video can be presented to highlight the important features.

The images in Figure 4.22 and 4.23 were taken from an animation generated by capturing instantaneous solutions at the AIP at a specified interval. For the figure, an interval of 0.1 milliseconds between frames was selected as it best highlighted key features observed within the videos. The color scheme matches the color scheme throughout this chapter to allow for further comparisons with the same basis. The ordering of the nine figures flows from top left to bottom right, reading across like lines in a book. In the frames, the two sets of counter-rotating vortices are observed. It is important to remember that these vortices extend from the generation on the surface from the spiral nodes within the separated flow.

Figure 4.22 for the DDES solution shows the set of counter-rotating vortices on the upper set grows in strength, noted with an decrease in the total pressure recovery. With stronger vortices, more low momentum fluid air from the boundary layer on the surface of the duct is convected into the vortices and into the core flow. The center bifurcation line separating the two counter-rotating vortices for the upper surface has a small peak that occurs in the loss of total pressure recovery just above the surface forming an upside down triangle created from the low momentum fluid. With the growing of the vortices, they also protrude out further out into the flow. Following this, the vortices seem to decrease in strength and size. The vortex shedding identified in Figure 4.15 accounts for the varying in strength of the vortices, which are shown rolling off of the separated flow on the upper surface. Additionally, the vortices on the upper surface displays the same pinching in effect noted throughout this chapter. The 2nd through the 4th frame most clearly show the high total pressure flow being swept into the base of the counter-rotating vortices following the low momentum fluid from the boundary layer being swept into the vortices. This pinching in effect oscillates over time.

While the counter-rotating vortices on the lower surface were also clearly defined, they are observed farther apart from each other than the pair on the upper surface in Figure 4.22. Due to the increased distance and second turn these vortices on the lower surface pass through as opposed to the pair on the upper surface, they

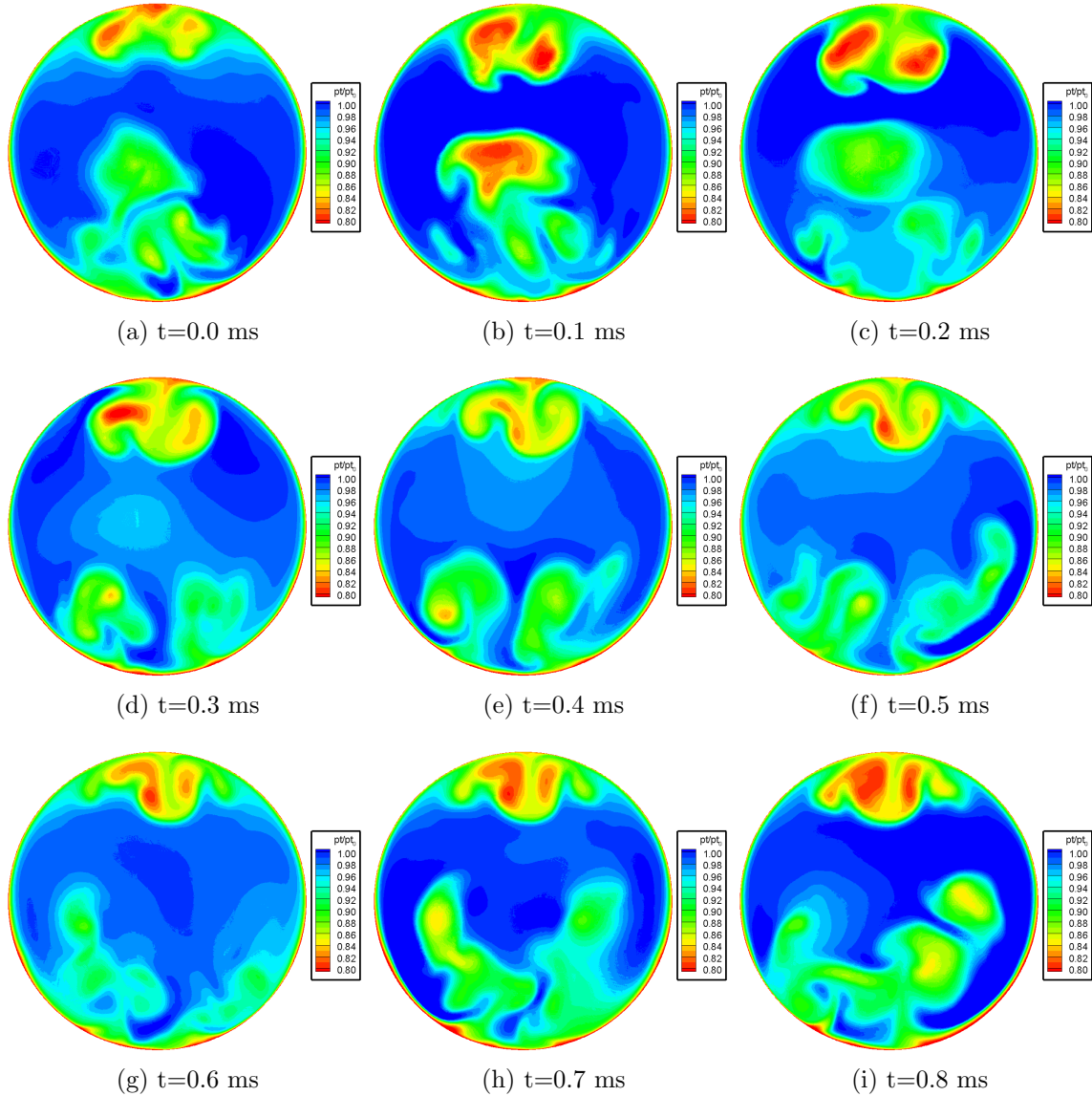


Figure 4.22: DDES video frames of the total pressure recovery at the AIP taken 0.1 milliseconds apart.

have more time to spread out and dissipate through the core flow. The dissipation and mixing with high momentum core flow also explain why the lower region has higher total pressure recovery than the upper surface. Like with the upper surface, vortex shedding is observed with the counter-rotating vortices combining and release a pocket with lower total pressure recovery into the core of the flow that quickly passes over the AIP.

Within almost every frame of Figure 4.22 there is at least one location in the flow that has less than a 80.0% total pressure recovery, whereas the average was 96.9%. The boundary layer is exempt from this observation as it is expected to have greater loss. While the value for the peak loss in total pressure recovery is used within inlet and engine design, these peak losses rarely occur in locations where AIP probes would have been located in the flow, further justifying the use of more probe locations in assessing the flow.

While the overall features compare between the DDES and WM-LES solutions of Figures 4.22 and 4.23, the WM-LES solution resolves much more eddy content than the DDES solution. The detail provided by resolving the energy content within eddies above the filter width better represents the flow past the AIP. This allows for the WM-LES to resolve the energy content as if forms within the boundary layer and convects it through the flow. Conversely, the DDES solution smears the total pressure recovery mapping more by not resolving the energy content within the RANS region near the wall. The comparison of the boundary layers on the sides of the duct between the DDES and WM-LES solutions best highlights this difference.

The WM-LES solution in Figure 4.23 shows the vorticies on the upper surface expanding and contracting as noticed for the DDES solution in Figure 4.22. Further, a decrease in total pressure recovery is noticed when the region has expanded and protrudes further into the flow, much like the DDES solution. The two counter-rotating vorticies that comprise the upper region of decreased total pressure recovery are also observed.

The lower counter-rotating vorticies in the WM-LES solution of Figure 4.23 are harder to distinguish due to the addition of the small scale eddies present within the flow. The counter-rotating vorticies are still shown convecting the low momentum fluid from the boundary layer into the flow creating reductions in the total pressure recovery. As noted in the DDES solution, the region of total pressure loss on the lower surface is wider than on the upper surface due to the increased distance and

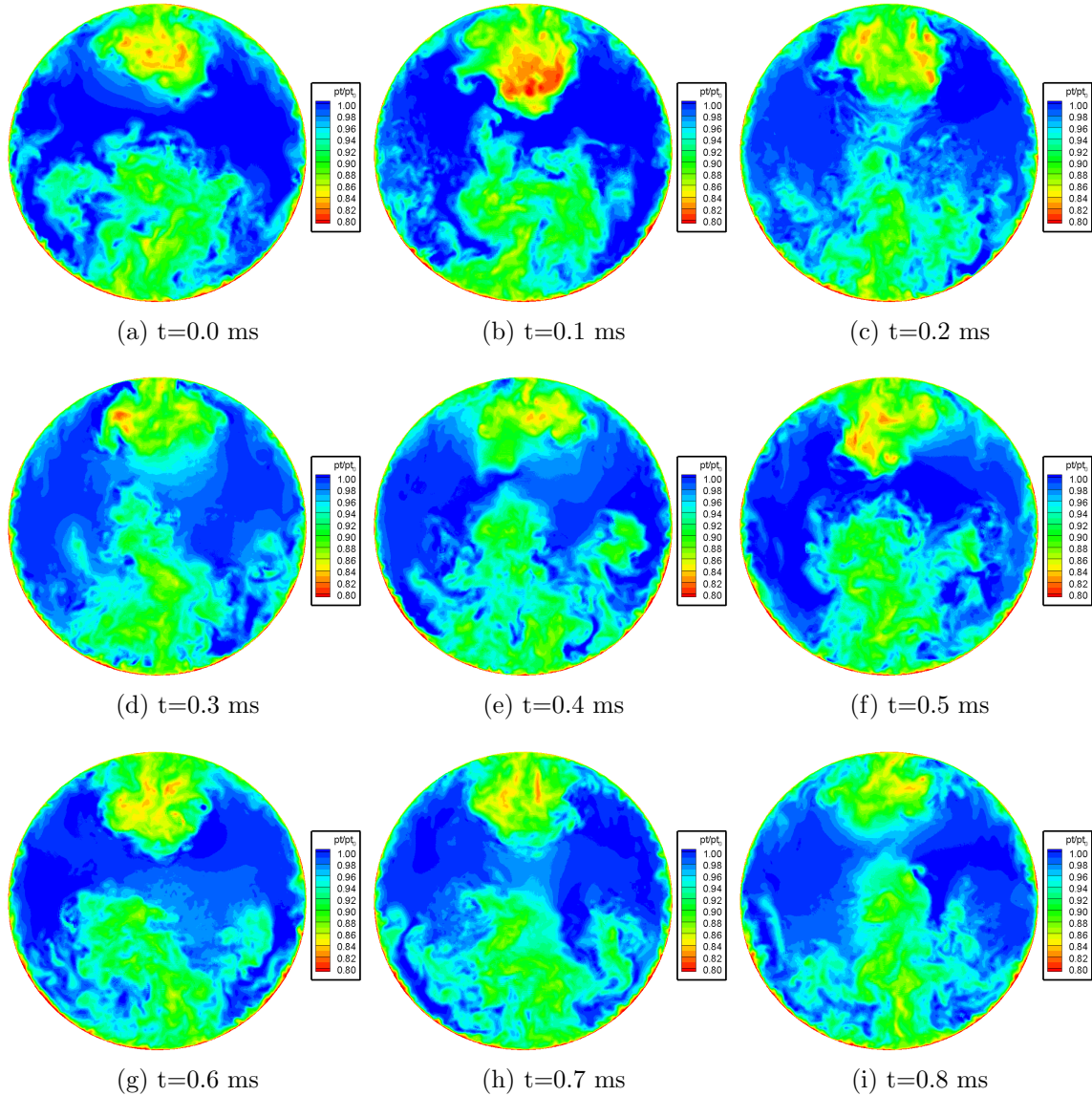


Figure 4.23: WM-LES video frames of the total pressure recovery at the AIP taken 0.1 milliseconds apart.

time the vorticies travel and mix with the core flow. Once again, the lower surface has higher values of total pressure recovery due to this phenomena. The WM-LES solution shows eddies from the separated flow traveling much higher into the flow. Based upon the location of the 40 probes on the AIP, this flow feature would not be captured. Since AIPs are commonly used to characterize flow for a turbine engine, the core flow is less important as that coincides with the location of the axle assembly.

While this exercise was conducted to better understand the greater complexity of the flow using the solution across the entire plane, a similar effort could be completed using the data from the 40 probes at a single instance in time. Although the flow features observed in this study were expected based on previous work, mapping the full slice builds upon the importance of using more than 40 probes at the AIP from Section 4.4. The flow features in the total pressure recovery from instantaneous solutions present much differently in shape, size, and magnitude than the averaged values would indicate. In both the DDES and WM-LES animations, the lowest total pressure recovery occurred at locations that do not align with the AIP probes. Therefore, the probes would not be able to detect peak instantaneous distortion within the flow.

4.6 Summary of Results

This chapter completed the methods defined in Chapter III to make comparisons in support of the primary objective of using a WM-LES turbulence model with higher order numerical methods on a structured grid to better predict flow within a serpentine inlet duct. Section 4.2 completed a grid independence study that identified the fine grid to use for the rest of the chapter. Further, the two different temporal schemes used indicated the 2nd order temporal scheme to better predict the flow features.

Following the independence study, Section 4.3 completed the test matrix in order to draw conclusions based on the completion of the primary objective. The DDES and WM-LES solutions obtained are compared to test data and previous modeling efforts using DDES. Through the use of total pressure recovery mappings at the AIP, oil flow visualizations, instantaneous centerplane slices, and flow distortion, the use of the structured grid and higher order methods improved the accuracy of the flow prediction. The use of higher order numerical methods with DDES enabled by a fully structured grid produced more accurate results than the previous mixed grid results. While the WM-LES simulation was obtained, marking a major milestone for the model within US3D, the results from this study did not indicate an increase in overall accuracy. Although the WM-LES solution appropriately simulated the high

eddy content within the flow and the total pressure recovery mapping of the upper surface closely matched test data, the flow was under resolved and needed more cells. It further proved its value by using 1/3 as many cells as the fine clustered grid allowing for a significant reduction the computational cost. The oil flow visualizations indicated a fundamental flaw in the wall model with regards to the equilibrium and zero pressure gradient assumptions preventing the wall from displaying reversed wall shear stress despite reversed flow existing within the cells above the wall, which would not have been corrected with only a higher grid density. With modifications, accurate modeling predictions could be obtained with WM-LES at a reduced computational cost.

The DDES solution performed better than the WM-LES simulation obtained. With a more refined grid for the WM-LES model to run, it is hypothesized that the solution would improve, but assumption

Two additional studies were conducted to further the understanding of the flow and drawbacks of using a 40 probe AIP. In Section 4.4, the 40 probe AIP was directly compared to the plane averaged solution using 72,000 points. The discretization of the 40 probes clearly prevents some flow features from presenting themselves, but both methods provided the same total pressure recovery for the plane as a whole. Section 4.5 analyzed frames from a video of the DDES and WM-LES solutions at the AIP. These frames are instantaneous and show more detail of the flow that is smoothed throughout the time average of the plane. Lastly, the locations that experienced the greatest loss in total pressure did not occur at locations where AIP probes were located adding justification for using more probe locations in testing.

V. Dyanmic Vreman

5.1 *Introduction*

The inclusion of a dynamic Vreman model in US3D was not part of the primary objective of modeling the serpentine inlet duct, but it was completed to expand the capability of US3D. This objective was outlined as the third objective of the secondary objectives listed in Chapter I. As noted in Section 3.2.2.1, the current incorporation of the WM-LES within US3D uses a Vreman SGS model. While Vreman showed that the model provides predictions comparable to the dynamic Smagorinsky model, without the incurred dynamic computational cost, he identified applying a dynamic procedure to the Vreman model could provide a further increase in accuracy of predictions [5]. While there are many publications detailing the dynamic Smagorinsky as an improved method, to the knowledge of the author, no established publications exist detailing the derivation and implementation of a dynamic Vreman model, serving as the motivation for this study. This chapter expands upon Vreman's statement by presenting the derivation of the application of the dynamic procedure developed by Germano *et al.* [25] to the Vreman SGS model. Following the derivation and incorporation into US3D, the dynamic Vreman model was verified and validated using a flat plate model in which a known solution exists.

5.2 *Methodology*

The first step of adding a dynamic Vreman model to US3D was the derivation of the numerical model in Section 5.2.1. While the concept of applying the larger test filter is relatively simple, the application of the test matrix and implementation of the model into US3D is detailed in Section 5.2.2. The model is exercised against a flat plate model defined in Section 5.2.3, with Section 5.2.4 identifying the data collection and analysis techniques applied to get the results presented in Section 5.3.

5.2.1 *Numerical Model.* The dynamic procedure defined by Germano *et al.* is applied to the Vreman model presented in Section 2.5.2 and reoutlined as:

$$\nu_T = c \sqrt{\frac{B_\beta}{\alpha_{ij}\alpha_{ij}}} \quad (5.1)$$

where c is the Vreman constant defined as $c = 2.5C_s^2$ in which C_s is the Smagorinsky constant [5]. The remaining components of the Vreman model are defined as:

$$\alpha_{ij} = \partial_i \overline{u_j} = \frac{\partial \overline{u_j}}{\partial x_i} \quad (5.2)$$

$$B_\beta = \beta_{11}\beta_{22} - \beta_{12}^2 + \beta_{11}\beta_{33} - \beta_{13}^2 + \beta_{22}\beta_{33} - \beta_{23}^2 \quad (5.3)$$

$$\beta_{ij} = \Delta_m^2 \alpha_{mi} \alpha_{mj} \quad (5.4)$$

in which the $\frac{\partial \overline{u_j}}{\partial x_i}$ are the velocity gradients [5].

The procedure begins with the application of the Germano relationship, T_{ij} , that by employing a second filter arrives at:

$$T_{ij} = \mathcal{L}_{ij} + \widehat{\tau}_{ij} = \widehat{\overline{\rho u_i u_j}} - \frac{1}{\widehat{\rho}} \widehat{\overline{\rho u_i}} \widehat{\overline{\rho u_j}} \quad (5.5)$$

in which the terms with a hat denote the second filter where terms with the bar and tilde represent Reynolds and Favre averaged variables [25]. The second filter, also known as the test filter, is larger with $\hat{\Delta} = 2\Delta$ being shown as the most optimal size for the second filter based upon compressible homogeneous turbulence [23]. The formalism of:

$$\mathcal{L}_{ij} = \widehat{\overline{\rho \widetilde{u}_i \widetilde{u}_j}} - \frac{1}{\widehat{\rho}} \widehat{\overline{\rho \widetilde{u}_i}} \widehat{\overline{\rho \widetilde{u}_j}} \quad (5.6)$$

is then necessary for the Germano relationship to be fully constructed. Following the assumption that the two subgrid tensors can be modeled with the same constant, the

following definitions are formed:

$$\tau_{ij} - \frac{1}{3}\tau_{kk}\delta_{ij} = c_d J_{ij} \quad (5.7)$$

$$T_{ij} - \frac{1}{3}T_{kk}\delta_{ij} = c_d K_{ij} \quad (5.8)$$

in which the subgrid model kernals, J_{ij} and K_{ij} , based upon the constant Vreman model are:

$$J_{ij} = -2\bar{\rho}\nu_T(\widetilde{S}_{ij} - \frac{1}{3}\delta_{ij}\widetilde{S}_{kk}) = -2\bar{\rho}\sqrt{\frac{B_\beta}{\alpha_{ij}\alpha_{ij}}}(\widetilde{S}_{ij} - \frac{1}{3}\delta_{ij}\widetilde{S}_{kk}) \quad (5.9)$$

$$K_{ij} = -2\widehat{\rho}\widehat{\nu}_T(\widehat{S}_{ij} - \frac{1}{3}\delta_{ij}\widehat{S}_{kk}) = -2\widehat{\rho}\sqrt{\frac{\widehat{B}_\beta}{\widehat{\alpha}_{ij}\widehat{\alpha}_{ij}}}(\widehat{S}_{ij} - \frac{1}{3}\delta_{ij}\widehat{S}_{kk}) \quad (5.10)$$

with the second filter being applied to the variables within the Vreman model. The assumption was made that commutation of the larger test filter to the variables from the original Vreman model occurs as:

$$\widehat{\alpha}_{ij} = \partial_i \widehat{u}_j = \frac{\partial \widehat{u}_j}{\partial x_i} \quad (5.11)$$

$$\widehat{B}_\beta = \widehat{\beta}_{11}\widehat{\beta}_{22} - \widehat{\beta}_{12}^2 + \widehat{\beta}_{11}\widehat{\beta}_{33} - \widehat{\beta}_{13}^2 + \widehat{\beta}_{22}\widehat{\beta}_{33} - \widehat{\beta}_{23}^2 \quad (5.12)$$

$$\widehat{\beta}_{ij} = \widehat{\Delta}^2 \widehat{\alpha}_{mi} \widehat{\alpha}_{mj} \quad (5.13)$$

where the test filter can be calculated for a face by taking a simple average of the values at opposite faces of the cells adjacent to the face being assessed. By combining Equations 5.7 and 5.8 into Equation 5.5, the following is generated:

$$\mathcal{L}_{ij}^d = \mathcal{L}_{ij} - \frac{1}{3}\mathcal{L}_{kk}\delta_{ij} = c_d K_{ij} \widehat{c}_d \widehat{J}_{ij} \quad (5.14)$$

with consideration that $\widehat{c}_d \widehat{J}_{ij} = c_d \widehat{J}_{ij}$ by assuming that the coefficient c_d is constant across the second filter width. The calculation of c_d is then formed in a manor

to minimize the error, E_{ij} , committed by the numerical method by solving for the residual as:

$$E_{ij} = \mathcal{L}_{ij}^d - c_d K_{ij} + c_d \widehat{J}_{ij} \quad (5.15)$$

in Germano *et al.* proposed:

$$\frac{\partial E_{ij} \widetilde{S}_{ij}}{\partial c_d} = 0 \quad (5.16)$$

with the tensor \widetilde{S}_{ij} remains undetermined to collapse Equation 5.15 in order to solve for a single solution, because Equation 5.15 contains six independent relationships that would result in up to six different constants being calculated. A method by Lilly [23] recasts Equation 5.16 as:

$$\frac{\partial E_{ij} E_{ij}}{\partial c_d} = 0 \quad (5.17)$$

followed by the application of a method of least-squares to solve for the dynamic constant. Explicitly, this can be written as:

$$c_d = \frac{M_{ij} \mathcal{L}_{ij}^d}{M_{kl} M_{kl}} \quad (5.18)$$

where

$$M_{ij} = K_{ij} - \widehat{J}_{ij} \quad (5.19)$$

in which Garnier *et al.* specify a few properties applying to c_d [23]. First, c_d can be negative, implying a local anti-dissipative nature, interpreted as the backwards energy-cascade [23]. Second, the range of c_d is not bounded in which the denominator can cancel out without the strict cancellation of numerator [23]. These properties affect the numerical stability of the model, and an *ad hoc* procedure is needed to ensure good numerical attributes of the model. One method consists of applying separate averages of the numerator and denominator as:

$$c_d = \frac{\langle M_{ij} \mathcal{L}_{ij}^d \rangle}{\langle M_{kl} M_{kl} \rangle} \quad (5.20)$$

whereby another method consists of time averaging the entire fraction as:

$$c_d = \left\langle \frac{M_{ij} \mathcal{L}_{ij}^d}{M_{kl} M_{kl}} \right\rangle \quad (5.21)$$

and for the purpose of the current study, the second method of applying an average of the entire fraction was used for a rolling average of the last 10 iterations. Additionally, clipping needed to be applied to ensure stability in which the the dynamic constant obtained by the dynamic procedure prior to time averaging for stability was constrained to $0 \leq c_d \leq 2c$ based upon the Vreman constant. While allowing negative values of c_d as an implicit energy backscatter method was considered as $-2c \leq c_d \leq 2c$, implementation proved to be unstable.

5.2.2 US3D Implementation. The dynamic Vreman model was implimented in US3D, a parallel implicit unstructured hypersonics reasearch CFD code developed by the University of Minnesota [40]. Inviscid fluxes are calculated using 2nd and 6th order kinetic-energy consistant schemes by Subbareddy and Candler [33] with a flux limiter by Ducros [34]. US3D already contains a constant Smagorinsky and constant Vreman models within the viscous flux routine, in which the dynamic Vreman model was added to the routine as a new model. The fluxes in US3D are calculated at the cell faces but variables are stored at the cell center. As US3D is a parallel code, the full grid is split into small domains for each core being utilized. Each smaller domain knows only the cells within it and passes information regarding shared cells to the other cores.

In the implementation of a larger test filter associated with the dynamic procedure, three different methods of averaging were applied based on the location of the face within the domain as shown in Figure 5.1, where the red face denotes the face currently being calculated and the dots representing the cell centers. The interior face is the easiest case in which the opposing faces are averaged across to achieve the test filter values. For boundary conditions, the assumption was made to use just a constant Vreman calculation without applying the dynamic procedure. Lastly, the shared

faces have two neighboring cell center values when using a 6th order flux scheme, so those two shared cells could be averaged onto the dashed imaginary face in Figure 5.1 that can then be subjected to the test filter. To facilitate the calculations of the test filter of opposing faces, a mapping was created to map each face to its opposing faces.

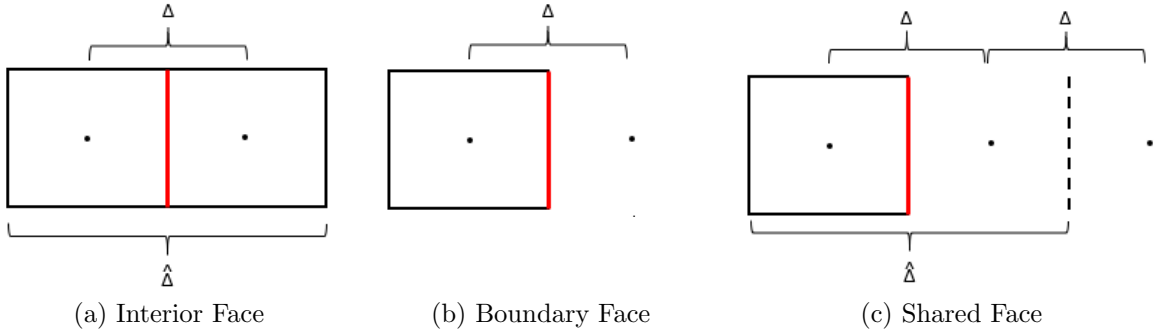


Figure 5.1: Test filter averaging for interior faces, boundary faces, and shared faces

To reduce redundant calculations, prior to calculating the dynamic procedure, the Vreman model is applied to all faces and stored for used in the dynamic procedure. These values used with the face to face mapping allows for the completion of Equations 5.9 and 5.10 needed in Equation 5.19. The numerator and denominator from Equation 5.18 are calculated to then obtain the iteration c_d from Equation 5.20, which is stored. To improve stability of the model, the c_d calculated from the last ten iterations are then averaged. The averaged c_d is then used within the constant Vreman equation to compute the turbulent viscosity for the face which is provided back to the rest of US3D.

Minor changes were made to other routines within US3D in order to allow the storage of the face to face mapping of opposing faces and the ten most recent iteration values of c_d for each face within the domain of the core. The last addition was allowing the selection of the dynamic Vreman model as a valid turbulence model in the input deck.

5.2.3 *Test Model.* A simple flat plate model is used with a grid designed for WR-LES for validation and verification of the dynamic Vreman model. The flat plate model is the same model used by Komives during the inclusion of the WM-LES within US3D [8], which is a model tested by Souverein *et al.* [41]. The dimensions of the box are based upon the thickness of the developed boundary layer prescribed in the inflow as $4\delta \times 10\delta \times 50\delta$ corresponding to the width, height, and length respectively, where $\delta = 11$ mm based upon the low Reynolds number test case ($Re_\theta = 5000$) by Souverein *et al.* [41]. The box generated contains $1191 \times 266 \times 151$ nodes in the x, y, and z directions respectively, for a total of 47.3 million cells. The x-z plane at $y=0$ served as the flat plate on the boundary of the domain. The first cell off the wall was set to a $y^+ = 0.5$ which is sufficient to support a WR-LES method.

The three dimensional model consists of a no-slip isothermal wall boundary condition on the lower face with periodic boundary conditions on either side running with the flow that are connected with each other. The surface above the plate uses a symmetric boundary condition as it is far enough from the plate to not impact the solution, and the 5δ prior to the upper surface applies a growth rate 20% to damp out the solution and reduce effects from the symmetric boundary. A supersonic outflow boundary is applied to the outflow surface. Lastly, a synthetic turbulent inflow is prescribed based on digital filtering as outlined by Komives [8]. The turbulent boundary layer used in the synthetic turbulence is scaled down to allow the flow to develop growing to the boundary layer thickness of $\delta = 11$ millimeters within the test section [8]. The scaling took a boundary layer profile from a RANS solution of the grid, that was then scaled to a point upstream of the desired boundary layer thickness [8].

Prior to collecting the turbulent statistics, the geometry is run for a sufficient length to allow for the turbulent inflow to fully propagate downstream. A fixed timestep of 1.2×10^{-7} seconds was used when collecting turbulent statistics to align with the results presented by Komives.

5.2.4 *Data Collection and Comparison.* The known flat plate solution will be compared to the solution obtained by the dynamic Vreman model. The primary figures of merit will be the ability to predict the coefficient of friction on the plate and the ability to recover the turbulent log law.

The coefficient of friction on the wall is obtained through statistics embedded in US3D that computes a running time average on the surface of the plate. The surface statistics include averaged shear stress in each direction as well as the averaged temperature on the wall. The three directional shear components are then combined to obtain the shear of the wall as:

$$\overline{\tau_w} = \sqrt{\overline{\tau_x^2} + \overline{\tau_y^2} + \overline{\tau_z^2}} \quad (5.22)$$

which is then used in:

$$C_f = \frac{\overline{\tau_w}}{0.5\rho U^2} \quad (5.23)$$

to calculate the coefficient of friction using free stream values for the density, ρ , and velocity magnitude, U , in the denominator. The coefficient of friction can then be compared to the test data value of 2.1×10^{-3} presented in the low Reynolds number by Souverein *et al.* [41].

A user routine was generated and implemented containing the inflow synthetic turbulent code as well as turbulent statistic methods. The method being used in the study collapses the grid along the z-axis to get a spatial average across the flow field that is then time averaged from iteration to iteration. This is the same method used with the S-duct detailed in Section 3.5.3. With the time averaged data, the average flow profile and boundary layer thickness can be assessed. Further, the velocity of the flow profile can be used to generate the log law plot comparing u^+ to y^+ .

5.3 Results

The dynamic Vreman model solution was first assessed to ensure the calculated c_d was independent to each face unlike a constant model. To visualize c_d , which is a face quantity, the value for c_d was averaged from the six faces of a cell to obtain a cell centered value that could be output in accordance to US3D's data structure. Figure 5.2 was nondimensionalized by the Vreman constant, $c = 0.064$, and shows that for the majority of the flow the calculated c_d falls at or below that of the Vreman constant. This indicates that the dynamic procedure is calculating a dynamic constant to prevent the buildup of energy at the subgrid filter width. While c_d may be greater than zero in the upper regions of Figure 5.2, the turbulent viscosity calculated may still be zero as no turbulent eddies exist in the flow, which is shown in Figure 5.3. Further, Figure 5.3 shows the development of the boundary layer from the scaled synthetic turbulence to a larger boundary layer approaching and growing larger than the test boundary layer thickness of 11 mm.

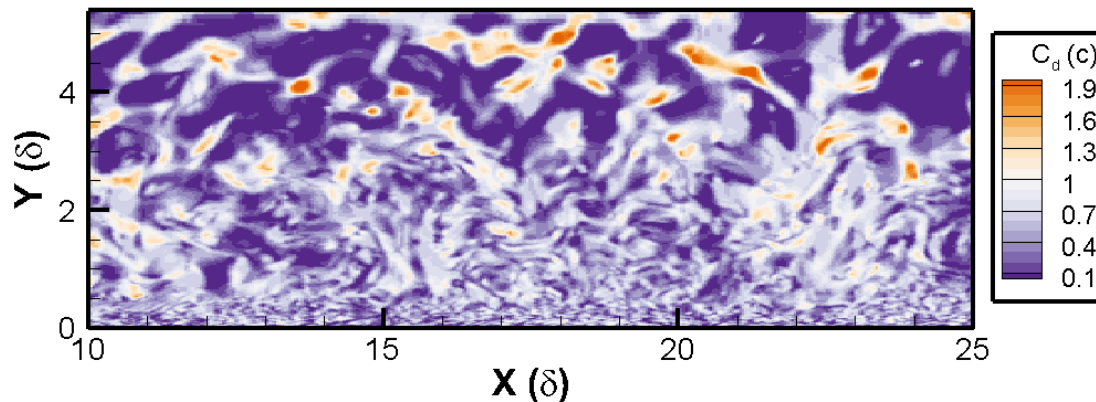


Figure 5.2: Instantaneous calculated c_d of a slice through the domain

Averaging the shear stress over time and combining to calculate the wall shear yields Figure 5.4. In Figure 5.4, the developing flow noted in Figure 5.3 is further emphasized through the increasing shear from from the leading edge of the domain to around 25δ where the maximum spanwise average occur. At which point, the wall shear decreased across the rest of the plate. Although the larger portion of the plate

is presented, the location at which the boundary layer thickness matches the value provided in the test data by Souverein *et al.* [41] is of importance.

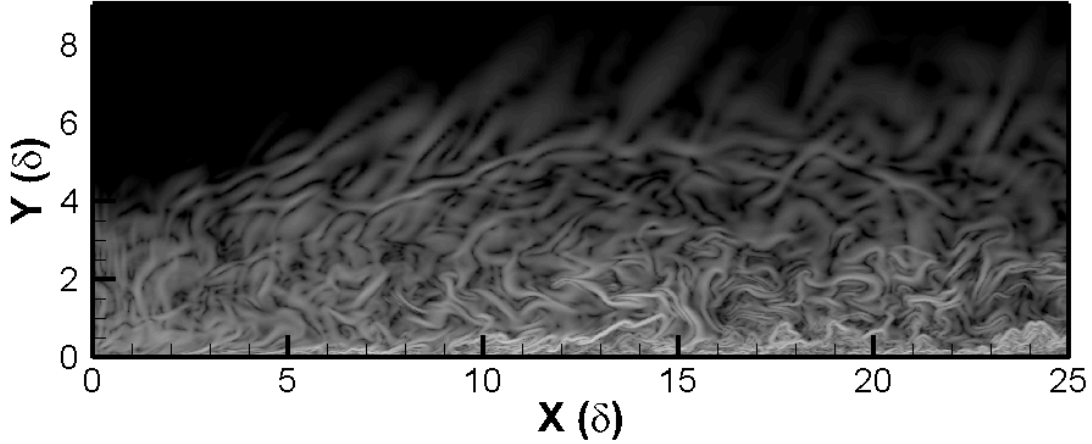


Figure 5.3: Instantaneous density gradient magnitude of a slice through the developing flow

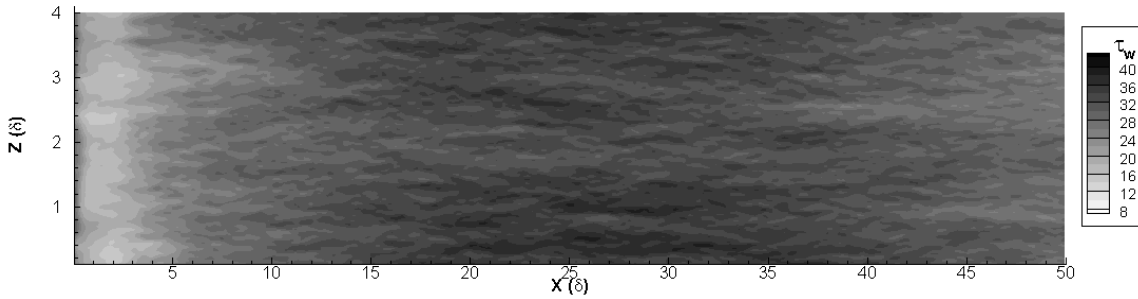


Figure 5.4: Time averaged wall shear on the surface of the flat plate

The time and spatial averaged flow data was assessed in vertical slices every δ along the x-axis. The post-processing routine used was generated by Komives in support of the WM-LES development [8], which at each location started at the wall and iterated along the slice until it reached the point at which the velocity had reached 99% of the freestream velocity of 550 m/s. This resulting value corresponded to the boundary layer thickness at that x location. Following this procedure, the location of 14δ provided a boundary layer thickness of $\delta = 11.06$ mm that matched the thickness reported by Souverein *et al.* that had developed from the synthetic inflow turbulence. This location was then used as the focus for all subsequent calculations.

A line at $x = 14\delta$ was extracted from Figure 5.4 to produce Figure 5.5. The time averaged wall shear was then averaged to obtain a mean wall shear of $\tau_w = 31.43$ Pa. To calculate Equation 5.23, the freestream density and velocity were obtained at $x = 14\delta$ and $y = 9\delta$. With values of $u = 547.9$ m/s and $\rho = 0.0959$ kg/m³ from this location, the coefficient of friction was determined to be $c_f = 2.18 \times 10^{-3}$. This value for the coefficient of friction is in close agreement with $c_f = 2.1 \times 10^{-3}$ from the data presented by Souverein *et al.*, with an error of 4.0%. Komives included 5% error bars in his presentation of the coefficient of friction, which contains the fine grid used here, showing agreement between the constant Vreman and dynamic Vreman models. Further, the location at which the test boundary layer thickness of 11 mm was obtained fell before the location where the Reynolds stresses were equalized accounting for some of the error calculated.

While attempts were made to present the recovery of the loglaw by the dynamic Vreman model, errors within the spatial averaging collection routine prevented usable data from being obtained. These errors further inhibited the calculation of the momentum boundary layer thickness, θ , and subsequent calculation of Re_θ that would provide additional comparisons to the test data presented by Souverein *et al.*. Additionally, it prevented the visualization and comparison of the Reynolds stress to test data that would further prove the accuracy of the model.

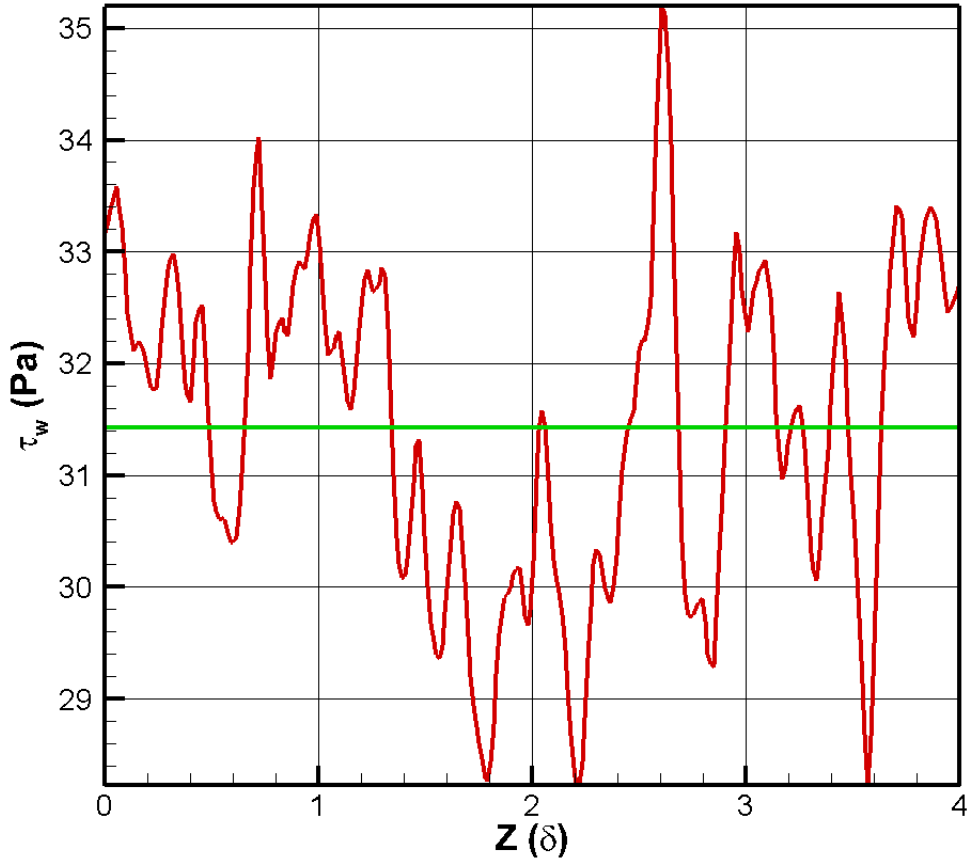


Figure 5.5: Time averaged wall shear and its mean at $x = 14\delta$ on the surface of the flat plate

5.4 Conclusion

The dynamic Vreman model that has been derived and implemented within US3D, shows promising results. Using the dynamic procedure developed by Germano *et al.* with a base single equation model of constant Vreman, a dynamic Vreman model was derived. The parallel unstructured architecture of US3D was leveraged to best implement a test filter optimized at two times the subgrid filter. Once implemented, the testing of the dynamic Vreman model was conducted on a turbulent flat plate, where a known solution exists. A synthetic inflow turbulence model was used to produce an inflow turbulence boundary layer thinner than the desired 11 mm

boundary layer allowed the boundary later to develop. This provided turbulent flow from the beginning, thus avoiding increased computational cost to model the additional turbulent transition and the need to trip the flow. The flat plate case selected was based off of work by Souverein *et al.* in which a low Reynolds case was presented.

To assess the model, plotting the dynamic constants calculated showed that most values were at or below that of the constant Vreman value, which was anticipated as it was the base model. A slice of the solution was presented showing the density gradient magnitude in which the growth of the boundary layer from the synthetic turbulent inflow can be assessed. The wall shear was obtained through a time averaging method within US3D that aided the visualization of the density gradient magnitude in showing flow development and decay. By assessing the boundary layer thickness based upon recovery of the freestream velocity, the location of $x = 14\delta$ was determined to correspond to a boundary layer thickness of 11.05 mm. By averaging the shear stress at this location on the flat plate, the coefficient of friction was determined to be 2.18×10^{-3} . The error in coefficient of friction prediction of 4.0% is small, but it aligns with results presented by Komives.

As the dynamic procedure incorporates many additional calculations, it increases the computational cost of the model. While this was considered the current study and efforts were made to limit the increase in computational cost, further optimization of the routines is recommended to obtain the ideal performance of the model. It would also be beneficial to conduct a study in order to fully quantify the increased cost experienced by the use of the dynamic procedure.

The current model was built in US3D using the 6th order spatial scheme allowing for the sharing of the necessary information for the test filter, which prevented its use with the S-duct that could only achieve stability at a 4th order scheme. For this reason it is recommended to restructure the dynamic Vreman model in US3D to run on 4th or 2nd order spatial schemes to allow for wider application of the model. Although this may increase the memory cost of the model and thus increase the computational

cost, the availability of the model on any grid, especially on complex geometry, would be worth the cost.

While further testing and analysis is needed, it was shown that the derivation and implementation of the dynamic Vreman model within US3D was successful. The model was able to obtain a coefficient of friction within a reasonable margin of 4.0% error compared to test data. Upon completion of the planned analysis, the inclusion of the dynamic Vreman model as a more advance subgrid scale model will expand the capabilities of US3D, successfully achieving the third secondary objective outlined in Chapter I.

VI. Conclusions and Recommendations

6.1 *Summary and Conclusions*

The flow separation and subsequent distortion within a diffusing serpentine inlet is a complex flow solution that has not been modeled with sufficient accuracy throughout previous studies. The need for accurate solutions is driven by industries desire to accelerate development with modeling in efforts to reduce costly testing. The primary objective defined in Section 1.3 consisted two primary parts to improve the accuracy of modeling predictions of S-duct flow. First, characterize the improvement through the use of higher order numerical models enabled by the use of a generated fully structured grid for DDES. Second, assess the viability of the WM-LES model in US3D for the S-duct to achieve increased accuracy with decreased computational cost. The primary objective was successfully completed through the development of a fully structured grid, the use of higher order numerical methods, and the use of both DDES and WM-LES on the S-duct. Comparisons between the solutions was achieved through the use of the figures of merit outlined in Section 1.3.3 including surface averaged wall shear stress and static pressure along with AIP time averaged total pressure recovery and flow distortion. While all the figures of merit were considered, the flow distortion and total pressure recovery were the most important in describing the flow at the AIP.

Chapter II provided a background on flow features observed through previous testing on S-ducts and the methods used to describe the flow. Turbulence modeling approaches from RANS to different types of LES such as wall resolved, wall modeled, and hybrid were all described to set the basis for why WM-LES was selected for this study. Previous modeling studies were presented that used RANS, DDES, and IDDES turbulence models, but no grid and model combination successfully predicted all the flow metrics from test data, further prompting the investigation of the structured grid with a WM-LES as an alternative approach to the problem.

The diffusing serpentine inlet duct was modeled using higher order numerical methods with DDES and WM-LES enabled by the generation of a fully structured

grid following the methods in Chapter III. The details on how a fully structured grid with different grid densities was generated was also included in Chapter III and satisfied the first task for the primary objective.

The grid independence study assessed three different grid densities and the effect of different temporal numerical schemes on the solution to start Chapter IV. The grid independence study based on 4th order spatial DDES solutions of 1st and 2nd order temporal schemes. The fine grid solution was determined to be grid independent with a difference of less than 1% for mass flow rate, total pressure recovery, and circumferential flow distortion when used with a 2nd order temporal scheme. Therefore, the fine grid was used in all further assessments and comparisons using DDES. While the fine grid was intended for use on the WM-LES, limitations in computational resources prevented its use.

The DDES and WM-LES solutions using 4th order spatial fluxes were then compared to test data and DDES solutions from Lakebrink and Mani [4] in Chapter IV following the methods presented in Chapter III to assess the accuracy and validity of the models. When comparing the solutions to previous test data, it was noted that the mass flow rates achieved were lower than the mass flow rates in the test data and previous modeling efforts. Since the mass flow rate was lower the total pressure recovery on the AIP mapping was higher as expected from a previous study by Lakebrink and Mani [4]. The DDES solutions obtained in this study better captured the total pressure recovery than the mixed grid DDES solution when compared to the test data, indicating that the increase to a 4th order flux scheme that was permitted by a fully structured grid improved the accuracy of the model. But the circumferential flow distortion values for structured grids were farther from test data than the mixed grid DDES solution. The WM-LES solution was the opposite of the DDES solutions obtained in this study, where the circumferential flow distortion was closer to matching the test data than the total pressure recovery. Further, the magnitudes of the higher order DDES solutions were closer to the expected total pressure mapping than the mixed grid DDES solutions. While the WM-LES total pressure mapping closely

matched the test data on the upper surface, the magnitude of the lower surface was higher than the test data. The use of a fine grid for the WM-LES solution may further resolve the core flow AIP measurements.

The DDES solution and WM-LES solutions obtained using 2nd order temporal accuracy and 4th order spatial fluxes were compared to the 2nd order flux scheme mixed grid DDES solution and test data using oil flow visualizations. The DDES solution obtained in this study had spiral nodes that were not fully developed or were nonsymmetrically positioned. The root cause of the poor oil flow visualization results were the surface statistics being initiated too early corrupting the overall average. The WM-LES solutions failed to develop separated flow on both the upper and lower surface separation regions. While the poor grid resolution could have been a factor, the more likely cause is the assumption of no pressure gradients at the wall. Since this flow clearly has large pressure gradients at the wall, the equilibrium wall model used may not be the most appropriate for this flow. Overcoming this assumption would not have been accomplished with a finer grid. Therefore, the solutions obtained in this study poorly predicted the flow separation locations, but recommendations to improve the results are included in Section 6.2.

Overall, the primary objective was successfully accomplished. The use of higher order methods enabled by a fully structured grid improved the accuracy of the DDES solutions. Further, the decreased dissipation from the use of higher order methods allowed for fewer cells to be used than the mixed grid solutions. Although, the DDES solutions were more accurate when looking at the AIP total pressure recovery mapping and AIP averaged value, the instantaneous slices showed fewer resolved eddies in the flow. The WM-LES simulation was the first ever conducted on this S-duct geometry, allowing for the assessment of its applicability for this complex flow problem. While the total pressure recovery mapping was not as accurate in the lower region of the duct, the upper region was very close to test data. Most importantly, the WM-LES solution only used 53 million cells as opposed to 148 million cells for the fine structured grid with wall clustering or the 186 million cells for the mixed grid, drastically reducing the

computational cost of the simulation. Additionally, it performed well at predicting the circumferential flow distortion, but it failed to predict the separation locations on the surface of the S-duct. While it validated the use of WM-LES for this type of problem meeting the primary objective, it identified several shortcomings of the currently implemented wall model within US3D. The shortcomings of the zero pressure gradient assumption and the use of an equilibrium wall model are further addressed with recommendations in Section 6.2.

Chapter IV also contained several other assessments to further expand the testing and modeling techniques used for characterizing S-ducts. First, the total pressure mappings were generated using both the 40 AIP probes and the overall averaged slice at the AIP. The difference in methods clearly showed that although 72,000 points cannot be captured with testing, 40 points are not enough to obtain the relevant features in the flow and produce different mappings. Interestingly, this comparison showed that the overall average across both methods yielded almost identical total pressure recovery values, which may only be a coincidence. Second, frames from videos generated at the AIP of the DDES and WM-LES solution were presented to understand differences in the instantaneous flow from the averaged flow. The comparison further supported the stance that 40 AIP probes are not sufficient. In all frames assessed, the largest loss in total pressure occurred in locations where AIP probes would not have been, resulting in test data that does not accurately capture key features of the flow.

A dynamic procedure was applied to the Vreman SGS model in Chapter V as a secondary objective to improve the overall turbulence modeling capabilities. The derivation and implementation of a dynamic Vreman model was the first of its kind. While intended to be used in the S-duct simulations, the implementation of the dynamic procedure used a 6th order spatial flux scheme that was unstable for the structured S-duct grid, so a known flat plate solution by Souverein *et al.* [41] was used to exercise the dynamic Vreman model. The coefficient of friction was determined to be 4.0% different from test data which falls within the error bounds previously presented by Komives [8] for US3D using the standard Vreman model on the same

test case. Further, the location at which the test boundary layer thickness of 11 mm was obtained fell before the location where the Reynolds stresses were equalized accounting for some of the error calculated. The addition of the dynamic Vreman model expanded the capability of US3D, and can be used in any LES turbulence model to improve its accuracy.

6.2 Recommendations and Future Research Areas

Through accomplishing the study, many areas of further study or changes in approach were identified. While some were discussed previously in this study, they are combined in this section to include them alongside the recommendations not previously presented.

While poor grid resolution was part of the cause for the poor oil flow visualizations, the assumption of no pressure gradient was another factor. Therefore, the wall model applied in the WM-LES solution should be modified to incorporate the pressure gradients at the wall. In addition to being better suited for this problem, this modification would allow for a wider application of the WM-LES method contained within US3D. Following this modification, the WM-LES simulation should be repeated using the fine unclustered grid. The independence study pointed to needing the fine grid, but due to computational resources available, the simulation was conducted on the medium density grid. As a result, it was noticeable in the WM-LES solution that too coarse of a grid was used as it failed to fully resolve the flow features in the core flow. Additionally, the assessment of y^+ on the wall of the S-duct for the WM-LES simulation was on average twice as large as it should be to appropriately resolve the boundary layer and subsequently the flow.

Since the cases conducted were unsteady, best CFD practices suggest to complete a timestep independence study similar to the grid independence study. While this was planned, it was not completed for a few reasons. First, to reduce the overall run duration with number of iterations needed to obtain multiple flowtimes, the largest

stable timestep for 1st order temporal 4th order spatial DDES with a structured grid was used. Second, the same time step was then run for all unsteady calculations for standardization among the the simulations. Lastly, the amount of computational resources needed to complete the study were not available.

Conducting the WM-LES probe sensitivity study as outlined in Section 3.4 should be completed. There was not enough time or resources to complete the probe sensitivity in this study. With the current knowledge of wall models, the placement of the wall model probe is not exactly known, and this additional study could significantly improve the WM-LES solution along with a more refined grid.

Several modifications to US3D are recommended to improve its functionality. First, the interpolate function provided in US3D needs to be reworked to better handle ghost cells. The interpolate function would have allowed for the solution from one grid to be interpolated onto a different grid. Following a period of time to wash out transients from the new grid or model being run statistics could be collected, reducing the computational time needed for the project. When the interpolate function was used, the solution crashed on the inflow and outflow boundaries. While several methods to fix the error were attempted like freezing the cells to reestablish the boundary conditions, none worked and the new grids were initialized from quiescent flow. As a result the computational cost of the study increased to allow for the mass balance of new grids to damp out to a converged state before statistics were initiated. The second modification to US3D is correcting the functionality of the surface statistics routine. The poor oil flow visualizations obtained resulted from not being able to turn off or restart the surface statistics once they were initiated. Once it was identified that the solution was contaminated with nonconverged iterations, the statistics could have been restarted to capture valid statistics if this function worked properly. The functionality is coded into US3D but as of now once statistics are turned on they stay on indefinitely for the solution.

The effect of the acoustic waves reflecting through the duct needed to be accounted for in the solution, but they could have been prevented with modifications made to the geometry provided. By applying a nozzle on the end of the extension tube, the outflow boundary condition could have been set to supersonic. This would have absorbed the acoustic waves and prevented their further propagation in the duct without affecting the solution within the S-duct. While applying a preconditioner to the flow would have also corrected the acoustic waves, the modification to the geometry would have been quicker and prevented the modification of the source code of US3D.

In Chapter V, there were several recommendations made regarding the implementation of the dynamic Vreman SGS model. First, it is recommended to restructure the model to run with a 2nd or 4th order spatial flux scheme. Requiring a 6th order spatial flux scheme limits the use of the model to highly Cartesian grids with very little grid stretching or skew. This would have prevented the use of this model within the S-duct structured grids used in this study. Changing the flux scheme the model is build off of enables wider use of this model. Second, the dynamic Vreman model could be improved in its implementation by streamlining the calculations to minimize the computational cost increase of the dynamic procedure. The current implementation was built with reducing redundant calculations in mind, it could be further consolidated. Third, further testing is needed to fully complete the verification and validation testing of the model. Exercising the model in more complicated flows to fully define when the increased cost for the dynamic procedure is needed to correct the shortcomings of single equation models. Lastly, the same simulation should be run in US3D for both the Vreman model and dynamic Vreman model to time the difference encountered with the use of the dynamic procedure.

Appendix A. AIP Grid Probe Locations

Table A.1: Probe locations of the AIP probes and the cell centers of the cells which the probe locations occur for the clustered coarse grid for DDDES.

Probe Number	Rake Leg	Ring	Requested Locations (m)			Achieved Locations (m)		
			x	y	z	x	y	z
1	1	1	3.18E-03	0.00E+00	2.01E-02	2.79E-03	2.96E-04	1.99E-02
2	1	2	3.18E-03	0.00E+00	3.48E-02	3.64E-03	-3.42E-04	3.44E-02
3	1	3	3.18E-03	0.00E+00	4.49E-02	2.93E-03	-3.09E-04	4.43E-02
4	1	4	3.18E-03	0.00E+00	5.31E-02	3.99E-03	3.18E-04	5.32E-02
5	1	5	3.18E-03	0.00E+00	6.02E-02	3.49E-03	-3.55E-04	6.06E-02
6	2	1	3.18E-03	1.42E-02	1.42E-02	3.17E-03	1.43E-02	1.46E-02
7	2	2	3.18E-03	2.46E-02	2.46E-02	2.60E-03	2.44E-02	2.44E-02
8	2	3	3.18E-03	3.18E-02	3.17E-02	3.65E-03	3.21E-02	3.18E-02
9	2	4	3.18E-03	3.76E-02	3.76E-02	3.15E-03	3.78E-02	3.80E-02
10	2	5	3.18E-03	4.26E-02	4.26E-02	2.79E-03	4.31E-02	4.26E-02
11	3	1	3.18E-03	2.01E-02	-1.27E-06	3.82E-03	2.00E-02	-1.20E-05
12	3	2	3.18E-03	3.48E-02	-1.27E-06	3.78E-03	3.45E-02	3.54E-04
13	3	3	3.18E-03	4.49E-02	-1.27E-06	3.41E-03	4.50E-02	2.43E-04
14	3	4	3.18E-03	5.31E-02	-1.27E-06	3.16E-03	5.33E-02	1.02E-04
15	3	5	3.18E-03	6.02E-02	-1.27E-06	2.97E-03	5.99E-02	7.30E-05
16	4	1	3.18E-03	1.42E-02	-1.42E-02	2.41E-03	1.41E-02	-1.46E-02
17	4	2	3.18E-03	2.46E-02	-2.46E-02	2.59E-03	2.43E-02	-2.46E-02
18	4	3	3.18E-03	3.18E-02	-3.18E-02	2.50E-03	3.12E-02	-3.16E-02
19	4	4	3.18E-03	3.76E-02	-3.76E-02	2.42E-03	3.74E-02	-3.77E-02
20	4	5	3.18E-03	4.26E-02	-4.26E-02	3.86E-03	4.24E-02	-4.22E-02
21	5	1	3.18E-03	0.00E+00	-2.01E-02	3.98E-03	-2.76E-04	-1.99E-02
22	5	2	3.18E-03	0.00E+00	-3.48E-02	2.56E-03	-3.57E-04	-3.46E-02
23	5	3	3.18E-03	0.00E+00	-4.49E-02	2.54E-03	3.13E-04	-4.45E-02
24	5	4	3.18E-03	0.00E+00	-5.31E-02	2.49E-03	-3.16E-04	-5.28E-02
25	5	5	3.18E-03	0.00E+00	-6.02E-02	3.90E-03	3.44E-04	-6.06E-02
26	6	1	3.18E-03	-1.42E-02	-1.42E-02	2.41E-03	-1.41E-02	-1.46E-02
27	6	2	3.18E-03	-2.46E-02	-2.46E-02	2.59E-03	-2.43E-02	-2.46E-02
28	6	3	3.18E-03	-3.18E-02	-3.18E-02	2.50E-03	-3.12E-02	-3.16E-02
29	6	4	3.18E-03	-3.76E-02	-3.76E-02	2.42E-03	-3.74E-02	-3.77E-02
30	6	5	3.18E-03	-4.26E-02	-4.26E-02	3.86E-03	-4.24E-02	-4.22E-02
31	7	1	3.18E-03	-2.01E-02	-1.27E-06	3.82E-03	-2.00E-02	-1.20E-05
32	7	2	3.18E-03	-3.48E-02	-1.27E-06	3.78E-03	-3.45E-02	3.54E-04
33	7	3	3.18E-03	-4.49E-02	-1.27E-06	3.41E-03	-4.50E-02	2.43E-04
34	7	4	3.18E-03	-5.31E-02	-1.27E-06	3.16E-03	-5.33E-02	1.02E-04
35	7	5	3.18E-03	-6.02E-02	-1.27E-06	2.97E-03	-5.99E-02	7.30E-05
36	8	1	3.18E-03	-1.42E-02	1.42E-02	3.17E-03	-1.43E-02	1.46E-02
37	8	2	3.18E-03	-2.46E-02	2.46E-02	2.60E-03	-2.44E-02	2.44E-02
38	8	3	3.18E-03	-3.18E-02	3.17E-02	3.65E-03	-3.21E-02	3.18E-02
39	8	4	3.18E-03	-3.76E-02	3.76E-02	3.15E-03	-3.78E-02	3.80E-02
40	8	5	3.18E-03	-4.26E-02	4.26E-02	2.79E-03	-4.31E-02	4.26E-02

Table A.2: Probe locations of the AIP probes and the cell centers of the cells which the probe locations occur for the clustered fine grid for DDES.

Probe Number	Rake Leg	Ring	Requested Locations (m)			Achieved Locations (m)		
			x	y	z	x	y	z
1	1	1	3.18E-03	0.00E+00	2.01E-02	2.80E-03	-1.97E-04	1.99E-02
2	1	2	3.18E-03	0.00E+00	3.48E-02	3.65E-03	2.20E-04	3.50E-02
3	1	3	3.18E-03	0.00E+00	4.49E-02	2.71E-03	-2.06E-04	4.50E-02
4	1	4	3.18E-03	0.00E+00	5.31E-02	3.23E-03	2.15E-04	5.30E-02
5	1	5	3.18E-03	0.00E+00	6.02E-02	2.68E-03	2.38E-04	6.01E-02
6	2	1	3.18E-03	1.42E-02	1.42E-02	3.28E-03	1.43E-02	1.41E-02
7	2	2	3.18E-03	2.46E-02	2.46E-02	3.29E-03	2.43E-02	2.46E-02
8	2	3	3.18E-03	3.18E-02	3.17E-02	3.52E-03	3.21E-02	3.19E-02
9	2	4	3.18E-03	3.76E-02	3.76E-02	2.96E-03	3.79E-02	3.77E-02
10	2	5	3.18E-03	4.26E-02	4.26E-02	3.68E-03	4.24E-02	4.27E-02
11	3	1	3.18E-03	2.01E-02	-1.27E-06	2.83E-03	2.02E-02	3.58E-06
12	3	2	3.18E-03	3.48E-02	-1.27E-06	3.59E-03	3.46E-02	-3.69E-05
13	3	3	3.18E-03	4.49E-02	-1.27E-06	2.86E-03	4.50E-02	-9.81E-05
14	3	4	3.18E-03	5.31E-02	-1.27E-06	3.57E-03	5.30E-02	-1.20E-04
15	3	5	3.18E-03	6.02E-02	-1.27E-06	3.30E-03	6.03E-02	-1.42E-04
16	4	1	3.18E-03	1.42E-02	-1.42E-02	3.13E-03	1.42E-02	-1.41E-02
17	4	2	3.18E-03	2.46E-02	-2.46E-02	2.85E-03	2.46E-02	-2.48E-02
18	4	3	3.18E-03	3.18E-02	-3.18E-02	3.52E-03	3.18E-02	-3.20E-02
19	4	4	3.18E-03	3.76E-02	-3.76E-02	3.34E-03	3.77E-02	-3.76E-02
20	4	5	3.18E-03	4.26E-02	-4.26E-02	3.19E-03	4.27E-02	-4.25E-02
21	5	1	3.18E-03	0.00E+00	-2.01E-02	3.07E-03	-1.85E-04	-2.01E-02
22	5	2	3.18E-03	0.00E+00	-3.48E-02	2.77E-03	-2.29E-04	-3.46E-02
23	5	3	3.18E-03	0.00E+00	-4.49E-02	3.56E-03	-2.03E-04	-4.48E-02
24	5	4	3.18E-03	0.00E+00	-5.31E-02	3.44E-03	-2.09E-04	-5.28E-02
25	5	5	3.18E-03	0.00E+00	-6.02E-02	3.29E-03	2.29E-04	-6.02E-02
26	6	1	3.18E-03	-1.42E-02	-1.42E-02	3.13E-03	-1.42E-02	-1.41E-02
27	6	2	3.18E-03	-2.46E-02	-2.46E-02	2.85E-03	-2.46E-02	-2.48E-02
28	6	3	3.18E-03	-3.18E-02	-3.18E-02	3.52E-03	-3.18E-02	-3.20E-02
29	6	4	3.18E-03	-3.76E-02	-3.76E-02	3.34E-03	-3.77E-02	-3.76E-02
30	6	5	3.18E-03	-4.26E-02	-4.26E-02	3.19E-03	-4.27E-02	-4.25E-02
31	7	1	3.18E-03	-2.01E-02	-1.27E-06	2.83E-03	-2.02E-02	3.58E-06
32	7	2	3.18E-03	-3.48E-02	-1.27E-06	3.59E-03	-3.46E-02	-3.69E-05
33	7	3	3.18E-03	-4.49E-02	-1.27E-06	2.86E-03	-4.50E-02	-9.81E-05
34	7	4	3.18E-03	-5.31E-02	-1.27E-06	3.57E-03	-5.30E-02	-1.20E-04
35	7	5	3.18E-03	-6.02E-02	-1.27E-06	3.30E-03	-6.03E-02	-1.42E-04
36	8	1	3.18E-03	-1.42E-02	1.42E-02	3.28E-03	-1.43E-02	1.41E-02
37	8	2	3.18E-03	-2.46E-02	2.46E-02	3.29E-03	-2.43E-02	2.46E-02
38	8	3	3.18E-03	-3.18E-02	3.17E-02	3.52E-03	-3.21E-02	3.19E-02
39	8	4	3.18E-03	-3.76E-02	3.76E-02	2.96E-03	-3.79E-02	3.77E-02
40	8	5	3.18E-03	-4.26E-02	4.26E-02	3.68E-03	-4.24E-02	4.27E-02

Table A.3: Probe locations of the AIP probes and the cell centers of the cells which the probe locations occur for the unclustered medium grid for WM-LES.

Probe Number	Rake Leg	Ring	Requested Locations (m)			Achieved Locations (m)		
			x	y	z	x	y	z
1	1	1	3.18E-03	0.00E+00	2.01E-02	3.73E-03	2.16E-04	2.00E-02
2	1	2	3.18E-03	0.00E+00	3.48E-02	3.66E-03	2.44E-04	3.50E-02
3	1	3	3.18E-03	0.00E+00	4.49E-02	2.76E-03	-2.27E-04	4.47E-02
4	1	4	3.18E-03	0.00E+00	5.31E-02	3.39E-03	-2.38E-04	5.28E-02
5	1	5	3.18E-03	0.00E+00	6.02E-02	2.82E-03	2.64E-04	6.02E-02
6	2	1	3.18E-03	1.42E-02	1.42E-02	2.87E-03	1.43E-02	1.39E-02
7	2	2	3.18E-03	2.46E-02	2.46E-02	3.09E-03	2.46E-02	2.48E-02
8	2	3	3.18E-03	3.18E-02	3.17E-02	3.55E-03	3.16E-02	3.17E-02
9	2	4	3.18E-03	3.76E-02	3.76E-02	2.94E-03	3.76E-02	3.77E-02
10	2	5	3.18E-03	4.26E-02	4.26E-02	3.82E-03	4.26E-02	4.26E-02
11	3	1	3.18E-03	2.01E-02	-1.27E-06	3.55E-03	2.00E-02	-9.93E-05
12	3	2	3.18E-03	3.48E-02	-1.27E-06	3.20E-03	3.48E-02	1.87E-04
13	3	3	3.18E-03	4.49E-02	-1.27E-06	2.53E-03	4.49E-02	1.07E-04
14	3	4	3.18E-03	5.31E-02	-1.27E-06	3.36E-03	5.34E-02	8.29E-05
15	3	5	3.18E-03	6.02E-02	-1.27E-06	3.10E-03	6.04E-02	7.56E-05
16	4	1	3.18E-03	1.42E-02	-1.42E-02	2.54E-03	1.44E-02	-1.42E-02
17	4	2	3.18E-03	2.46E-02	-2.46E-02	3.58E-03	2.46E-02	-2.44E-02
18	4	3	3.18E-03	3.18E-02	-3.18E-02	3.19E-03	3.18E-02	-3.21E-02
19	4	4	3.18E-03	3.76E-02	-3.76E-02	3.00E-03	3.76E-02	-3.74E-02
20	4	5	3.18E-03	4.26E-02	-4.26E-02	2.85E-03	4.25E-02	-4.28E-02
21	5	1	3.18E-03	0.00E+00	-2.01E-02	3.77E-03	2.05E-04	-2.03E-02
22	5	2	3.18E-03	0.00E+00	-3.48E-02	3.50E-03	2.52E-04	-3.47E-02
23	5	3	3.18E-03	0.00E+00	-4.49E-02	3.23E-03	2.25E-04	-4.51E-02
24	5	4	3.18E-03	0.00E+00	-5.31E-02	3.09E-03	2.34E-04	-5.34E-02
25	5	5	3.18E-03	0.00E+00	-6.02E-02	2.94E-03	2.56E-04	-6.03E-02
26	6	1	3.18E-03	-1.42E-02	-1.42E-02	2.54E-03	-1.44E-02	-1.42E-02
27	6	2	3.18E-03	-2.46E-02	-2.46E-02	3.58E-03	-2.46E-02	-2.44E-02
28	6	3	3.18E-03	-3.18E-02	-3.18E-02	3.19E-03	-3.18E-02	-3.21E-02
29	6	4	3.18E-03	-3.76E-02	-3.76E-02	3.00E-03	-3.76E-02	-3.74E-02
30	6	5	3.18E-03	-4.26E-02	-4.26E-02	2.85E-03	-4.25E-02	-4.28E-02
31	7	1	3.18E-03	-2.01E-02	-1.27E-06	3.55E-03	-2.00E-02	-9.93E-05
32	7	2	3.18E-03	-3.48E-02	-1.27E-06	3.20E-03	-3.48E-02	1.87E-04
33	7	3	3.18E-03	-4.49E-02	-1.27E-06	2.53E-03	-4.49E-02	1.07E-04
34	7	4	3.18E-03	-5.31E-02	-1.27E-06	3.36E-03	-5.34E-02	8.29E-05
35	7	5	3.18E-03	-6.02E-02	-1.27E-06	3.10E-03	-6.04E-02	7.56E-05
36	8	1	3.18E-03	-1.42E-02	1.42E-02	2.87E-03	-1.43E-02	1.39E-02
37	8	2	3.18E-03	-2.46E-02	2.46E-02	3.09E-03	-2.46E-02	2.48E-02
38	8	3	3.18E-03	-3.18E-02	3.17E-02	3.55E-03	-3.16E-02	3.17E-02
39	8	4	3.18E-03	-3.76E-02	3.76E-02	2.94E-03	-3.76E-02	3.77E-02
40	8	5	3.18E-03	-4.26E-02	4.26E-02	3.82E-03	-4.26E-02	4.26E-02

Bibliography

1. Wellborn, S. R., Reichert, B. A., and Okiishi, T. H., “An Experimental Investigation of the Flow in a Diffusing S-Duct,” *28th Joint Propulsion Conference and Exhibit*, , No. AIAA 1992-3622, 1992.
2. Delot, A.-L. and Scharnhorst, R. K., “A Comparison of Several CFD Codes with Experimental Data in a Diffusing S-Duct,” *49th AIAA/ASME/SAE/ASEE Joint Propulsion Conference*, , No. AIAA 2013-3796, 2013.
3. Winkler, C. M. and Davis, Z. S., “Summary of the 3rd Propulsion Aerodynamics Workshop: S-duct Results,” , No. AIAA 2017-4912, July 2017.
4. Lakebrink, M. T. and Mani, M., “Numerical Investigation of Dynamic Distortion and Flow Control in a Serpentine Diffuser,” *2018 AIAA Aerospace Sciences Meeting*, , No. AIAA 2018-1283, January 2018.
5. Vreman, A. W., “An Eddy-Viscosity Subgrid-Scale Model for Turbulent Shear Flow: Algebraic Theory and Applications,” Vol. 16, No. 10, 2004, pp. 3670–3681.
6. Cantwell, B., “AA200 Chapter 9 - Viscous Flow Along a Wall,” https://web.stanford.edu/cantwell/AA200_Course_Material/AA200_Course_Notes/, 24 September 2018.
7. White, F. M., *Fluid Mechanics*, McGraw-Hill, 5th ed., 2003.
8. Komives, J. R., *Development and Validation of a LES Turbulence Wall Model for Compressible Flows with Heat Transfer*, Ph.D. thesis, The University of Minnesota, 2016.
9. Spalding, D. B., “A Single Formula for the Law of the Wall,” *Journal of Applied Mechanics*, , No. 28(3), 1961, pp. 455–458.
10. Pope, S. B., *Turbulent Flows*, Cambridge University Press, New York, NY, 2000.
11. Wellborn, S. R., Okiishi, T. H., and Reichert, B. A., “A Study of the Compressible Flow Through a Diffusing S-Duct,” , No. NASA/TM - 106411, 1993.
12. Squire, L. C., “The Motion of a Thin Oil Sheet Under the Steady Boundary Layer on a Body.” *Journal of Fluid Mechanics*, Vol. 11, No. 2, January 1961, pp. 161–179.
13. Tobak, M. and Peake, D., “Topology of Two-Dimensional and Three-Dimensional Separated Flows,” , No. NASA/TM - 81294, 1979.
14. Hornung, H. and Perry, A. E., “Some Aspects of Three-Dimensional Separation. I. Streamsurface Bifurcations,” *Zeitschrift für Flugwissenschaften und Weltraumforschung*, Vol. 8, No. 2, March 1984, pp. 77–87.
15. Perry, A. E. and Hornung, H., “Some Aspects of Three-Dimensional Separation. II. Vortex Skeletons,” *Zeitschrift für Flugwissenschaften und Weltraumforschung*, Vol. 8, No. 3, May 1984, pp. 155–160.

16. Mattingly, J. D., Heiser, W. H., and Pratt, D. T., *Aircraft Engine Design.*, AIAA education series, American Institute of Aeronautics and Astronautics, Reston VA, 2nd ed., 2002.
17. Younghans, J., “Engine Inlet Systems and Integration with Airframe,” *University of Tennessee Space Institute*, 1980.
18. Mattingly, J. D., *Elements of Propulsion : Gas Turbines and Rockets.*, AIAA education series, American Institute of Aeronautics and Astronautics, 2006.
19. SAE, “Gas Turbine Engine Inlet Flow Distortion Guidelines,” Tech. rep., 2002.
20. Blazek, J., *Computational Fluid Dynamics: Principles and Applications.*, Butterworth-Heinemann, Amsterdam, 3rd ed., 2015.
21. Georgiadis, N. J., Rizzetta, D. P., and Fureby, C., “Large-Eddy Simulation: Current Capabilities, Recommended Practices, and Future Research,” *AIAA Journal*, Vol. 48, No. 8, 2010, pp. 1772–1784.
22. Kawai, S. and Larsson, J., “Wall-Modeling in Large Eddy Simulation: Length Scales, Grid Resolution, and Accuracy,” *Physics of Fluids*, Vol. 24, No. 1, 2012.
23. Garnier, E., Adams, N. A., and Sagaut, P., *Large Eddy Simulation for Compressible Flows.*, Springer, Berlin, 2009.
24. Smagorinsky, J., “General Circulation Experiments with the Primitive Equations,” *Monthly Weather Review*, , No. 91, 1963, pp. 99–165.
25. Germano, M., Piomelli, U., Moin, P., and Cabot, W. H., “A Dynamic Subgrid-Scale Eddy Viscosity Model.” *Physics of Fluids A: Fluid Dynamics*, Vol. 3, No. 7, July 1991, pp. 1760–1765.
26. Larsson, J., Kawai, S., Bodart, J., and Bermejo-Moreno, I., “Large Eddy Simulation with Modeled Wall-Stress: Recent Progress and Future Directions,” *Mechanical Engineering Reviews*, Vol. 3, No. 1, 2016.
27. Choi, H. and Moin, P., “Grid-Point Requirements for Large Eddy Simulation: Chapman’s Estimates Revisited.” *Physics of Fluids*, Vol. 24, No. 1, 2012.
28. Marco, N. and Komives, J. R., “Wall-Modeled Large Eddy Simulation of a Three-Dimensional Shock-Boundary Layer Interaction,” *2018 AIAA Aerospace Sciences Meeting*, January 2018.
29. Spalart, P. R., Deck, S., Shur, M. L., Squires, K. D., Strelets, M. K., and Travin, A., “A New Version of Detached-Eddy Simulation, Resistant to Ambiguous Grid Densities.” *Theoretical and Computational Fluid Dynamics*, Vol. 20, No. 3, 2006, pp. 181 – 195.
30. Shur, M. L., Spalart, P. R., Strelets, M. K., and Travin, A. K., “A Hybrid RANS-LES Approach with Delayed-DES and Wall-Modelled LES capabilities.” *International Journal of Heat and Fluid Flow*, Vol. 29, 2008, pp. 1638 – 1649.

31. Reichert, B. A., “A Study of High Speed Flows in an Aircraft Transition Duct,” , No. NASA/TM - 104449, 1991.
32. Scharnhorst, R. K. and Delot, A.-L., “Computational and Experimental Results for Flows in a Diffusing S-Duct without and with Flow Control Devices,” *AIAA Propulsion and Energy Forum*, , No. 2015-3964, 2015.
33. Subbareddy, P. K. and Candler, G. V., “A Fully Discrete, Kinetic Energy Consistent Finite-Volume Scheme for Compressible Flows,” *Journal of Computational Physics*, Vol. 228, No. 5, 2009, pp. 1347–1364.
34. Ducros, F., Ferrand, V., Nicoud, F., Weber, C., Darracq, D., Gacherieu, C., and Poinso, T., “Large-Eddy Simulation of the Shock/Turbulent Interaction,” *Journal of Computational Physics*, Vol. 152, No. 2, 1999, pp. 517–549.
35. Bond, R. B. and Blottner, F. G., “Derivation, Implementation, and Initial Testing of a Compressible Wall-Layer Model.” *International Journal for Numerical Methods in Fluids*, Vol. 66, No. 9, 2011, pp. 1183 – 1206.
36. *LINK3D Version 1.1x Software User Manual.*, 2017.
37. Johnson, H., Drayna, T., Nompelis, I., and Candler, G., *US3D User Manual v1.1*.
38. Chaudhry, R. S. and Candler, G. V., “Computing Measured Spectra from Hypersonic Pitot Probes with Flow-Parallel Freestream Disturbances.” *AIAA Journal*, Vol. 55, No. 12, 2017, pp. 4155–4166.
39. Frigo, M. and Johnson, S. G., “The Design and Implementation of FFTW3,” *Proceedings of the IEEE*, Vol. 93, No. 2, 2005, pp. 216–231, Special issue on “Program Generation, Optimization, and Platform Adaptation”.
40. Nompelis, I., Drayna, T., and Candler, G., “A Parallel Unstructured Implicit Solver for Hypersonic Reacting Flow Simulation,” *17th AIAA Computational Fluid Dynamics Conference*, 2005.
41. Souverein, L. J., Dupont, P., Debiève, J.-F., Van Oudheusden, B. W., and Scarano, F., “Effect of Interaction Strength on Unsteadiness in Shock-Wave-Induced Separations,” *AIAA Journal*, Vol. 48, No. 7, 2010, pp. 1480–1493.

Vita

Captain Ryan Thompson was born and raised in Trenton, MI. He graduated from Trenton High School in 2009 and subsequently attended the United States Air Force Academy where he earned a Bachelor of Science degree in Aeronautical Engineering in 2013. Following Captain Thompson's commission, he worked at the Air Force Nuclear Weapons Center. He began his AFIT master's degree program in the fall of 2017; this thesis completes his degree requirements to earn a Masters of Science degree in Aeronautical Engineering.

Permanent address: 2950 Hobson Way
Air Force Institute of Technology
Wright-Patterson AFB, OH 45433

REPORT DOCUMENTATION PAGE				Form Approved OMB No. 0704-0188	
The public reporting burden for this collection of information is estimated to average 1 hour per response, including the time for reviewing instructions, searching existing data sources, gathering and maintaining the data needed, and completing and reviewing the collection of information. Send comments regarding this burden estimate or any other aspect of this collection of information, including suggestions for reducing the burden, to Department of Defense, Washington Headquarters Services, Directorate for Information Operations and Reports (0704-0188), 1215 Jefferson Davis Highway, Suite 1204, Arlington, VA 22202-4302. Respondents should be aware that notwithstanding any other provision of law, no person shall be subject to any penalty for failing to comply with a collection of information if it does not display a currently valid OMB control number. PLEASE DO NOT RETURN YOUR FORM TO THE ABOVE ADDRESS.					
1. REPORT DATE (DD-MM-YYYY) 03/01/2019		2. REPORT TYPE Master's Thesis		3. DATES COVERED (From - To) September 2017 - March 2019	
4. TITLE AND SUBTITLE Wall Model Large Eddy Simulation of a Diffusing Serpentine Inlet Duct				5a. CONTRACT NUMBER	
				5b. GRANT NUMBER	
				5c. PROGRAM ELEMENT NUMBER	
6. AUTHOR(S) Thompson, Ryan J. Capt				5d. PROJECT NUMBER	
				5e. TASK NUMBER	
				5f. WORK UNIT NUMBER	
7. PERFORMING ORGANIZATION NAME(S) AND ADDRESS(ES) Air Force Institute of Technology Graduate School of Engineering and Management (AFIT/EN) 2950 Hobson Way Wright-Patterson AFB OH 45433-7765				8. PERFORMING ORGANIZATION REPORT NUMBER	
9. SPONSORING/MONITORING AGENCY NAME(S) AND ADDRESS(ES) The Boeing Company Senor Research Fellow, Mori Mani 6200 James S McDonnell Blvd Saint Louis, MO 63134 mori.mani@boeing.com				10. SPONSOR/MONITOR'S ACRONYM(S)	
				11. SPONSOR/MONITOR'S REPORT NUMBER(S) AFIT-ENY-MS-19-M-248	
12. DISTRIBUTION/AVAILABILITY STATEMENT Distribution Statement A. Approved for Public Release;Distribution Unlimited					
13. SUPPLEMENTARY NOTES This work is declared a work of the U.S. Government and is not subject to copyright protection in the United States.					
14. ABSTRACT Accurate modeling predictions of an S-duct are needed to reduce costly testing and accelerate development time while characterizing the flow following the inlet. While DNS is too cost prohibitive due to grid scaling with Reynolds number, WM-LES remains a tractable alternative. The use of higher order numerical models on a fully structured grid in US3D were assessed using DDES and WM-LES turbulence models to obtain increased prediction accuracy of the S-duct flow when compared to previous studies and test data. Further, a first of its kind dynamic Vreman model was derived, implemented, and validated in US3D using a flat plate model.					
15. SUBJECT TERMS Large Eddy Simulation, Inlet Distortion, Serpentine Inlet, Dynamic Vreman					
16. SECURITY CLASSIFICATION OF:			17. LIMITATION OF ABSTRACT	18. NUMBER OF PAGES	19a. NAME OF RESPONSIBLE PERSON
a. REPORT	b. ABSTRACT	c. THIS PAGE			Jeffrey R. Komives
U	U	U	UU	184	19b. TELEPHONE NUMBER (Include area code) (937) 255-6565 x4744

Standard Form 298 (Rev. 8/98)
Prescribed by ANSI Std. Z39.18